Growth, Characterisation and Surface Structures of MnSb and NiSb Thin Films

by

James Douglas Aldous

Thesis

Submitted to the University of Warwick

for the degree of

Doctor of Philosophy

Department of Physics

July 2011

THE UNIVERSITY OF
WARWICK

Contents

Contents

List of Tables

List of Figures

Acknowledgments

No one would have believed, in the first years of the twenty teens, that this thesis would have been produced and published. No one could have dreamed that it would be scrutinised as someone with a microscope studies creatures that swarm and multiply in a drop of water. Few even considered the possibility of this thesis becoming a reality and yet, across the gulf of Britain, minds immeasurably superior to my own regarded this thesis with dubious eyes.

Anyone for pig?

Declarations

I declare that this thesis reports my work between July 2007 and May 2011 under the supervision of Dr Gavin Bell. The research reported here has not been submitted either wholly or in part in this or any other academic institution for the admission to a higher degree.

All data presented in this thesis has been acquired from MnSb thin films grown by the author using the Warwick MBE system. X-ray diffraction data presented in Chap. 3 and Chap. 4 was taken with the assistance of Dr Thomas Hase, Dr Stuart Wilkins and Dr David Walker. The TEM data in Chap. 4 was taken and analysed by Dr Richard Beanland and Dr Ana Sanchez. The atomic force micrograph in figure Fig. 4.4 was taken by Mr Christopher Burrows. The in-house magnetometry data in Chap. 5 was collected with the assistance of Dr Martin Lees. The XMCD data also presented in Chap. 5 was collected by the author with the assistance of Dr Thomas Hase and in collaboration with Dr Cecilia Sánchez-Hanke at the National Synchrotron Light Source, USA. The SPRKKR calculations discussed in Sec. 5.2 and shown in Fig. 5.4 were performed by Mr Ian Maskery. The SPLEEM data in Fig. 5.6 was acquired and analysed by Dr Wolfgang Theis and Mr Thibault Decoster of Birmingham University. The CAICISS data in Chap. 6 was acquired and analysed with the assistance of Dr Marc Walker. The LEED I-V data, also presented in Chap. 6, was acquired by the author at Liverpool University in collaboration with Dr Vinod Dhanak. The DFT calculations on the cubic phase of NiSb was performed by undergraduate project students, Mr David Pickup and Todd Humphries. All other data and interpretation has been carried out by the author.

The work in this thesis has either been published in or awaiting submission to a refereed journal:

- *Stoichiometry, contamination and microstructure of MnSb(0001) surfaces*, S. A. Hatfield, J. D. Aldous and G. R. Bell *Applied Surface Science* **255** (2009) pp. 3567-3575

- *Surface Magnetism in epitaxial MnSb films*, J. D. Aldous, C. W. Burrows, T. P. A. Hase, J. A. Duffy, C. Sánchez-Hanke, A. Quesada, A. K. Schmid, T. Decoster, W. Theis and G. R. Bell, *to be submitted to J. Appl. Phys.*

- *Spin polarisation in epitaxial MnSb polymorphs*, A. M. Sánchez, R. Beanland, J. D. Aldous, C. W. Burrows, I. Maskery, M. d-S. Dias, M. Bradley, J. B. Staunton and G.R. Bell, *to be submitted to Phys. Rev. B*

- *Growth and structural characterisation of NiSb(0001) thin films*, J. D. Aldous, M. Brewer, S. Wilkins, C. W. Burrows, G. R. Bell and T. P. A. Hase, *in preparation*

Work in this thesis has also been presented at the following conferences (presenting author in bold):

- *Micro- and Nano- structure of MnSb(0001) thin films on III-V Substrates*, **J. D. Aldous**, S. A. Hatfield and G. R. Bell, poster presentation at the 8th Scanning Probe Microscopy conference, 2008

- *Growth, Repreparation and Surface Magnetic Properties of MnSb(0001)*, **J. D. Aldous**, C. W. Burrows and G. R. Bell, poster presentation at the 10th European Conference on Surface Crystallography and Dynamics, 2010

- *Magnetic properties of epitaxial MnSb(0001) thin films*, **J. D. Aldous**, C. W. Burrows, T. P. A. Hase, J. A. Duffy, C. Sánchez-Hanke, A. Quesada, A. K. Schmid, T. Decoster, W. Theis and G. R. Bell, poster presentation at the IoP Condensed Matter and Materials Physics conference, 2010

Abstract

Epitaxial growth of NiSb on GaAs(111)B substrates has been achieved for the first time. X-ray diffraction confirms the films are of high quality and oriented (0001) with respect to the (111) substrate. Surface reconstructions have been observed on NiSb thin films through electron diffraction performed *in situ* during and after growth. Three different surface reconstructions have so far been observed. Two of these, the (4×4) and (4×6) reconstructions, are entirely new to the binary pnictides. The latter, however, is only metastable. The third reconstruction is a td(1×3) and is believed to be related to similar reconstructions seen on MnSb and MnAs.

The epitaxial growth of MnSb on GaAs(111)B substrates has been the subject of a J dependent growth study. It is seen that the final surface morphology is highly sensitive to the local beam flux ratio, J, with changes of a few percent leading to sharp and abrupt changes in the morphology. An XRD investigation of these films reveal varied and complex behaviour, with the appearance of a large number of reflections which do not originate from either GaAs(111) or MnSb(0001). Cubic MnSb(111) crystallites have been seen in some thin films in a variety of strain states with evidence of tetragonal distortions.

Surface preparation methods of air-exposed MnSb has been investigated using a combination of x-ray photoelectron spectroscopy (XPS), scanning electron microscopy (SEM) and x-ray mangetic circular dichroism (XMCD). A thick Mn-oxide layer, which is resistant to conventional *in situ* ion-bombarding and annealing (IBA) methods, is formed after exposure to air. Such surfaces are found to be non-magnetic. A simple combination of HCl acid etching followed by *in situ* IBA treatments is found to result in a well ordered (2×2) surface, with the recovery of a magnetic surface. A new antimony capping procedure has been investigated and found to be effective in preventing oxidation of the surface even after prolonged exposure to air. Such samples are found to retain a magnetic surface. It will also be shown that detailed analysis of the XMCD is not possible due to jj coupling which precludes the use of the sum rules, whilst theoretical calculations within the SPR-KKR DFT framework fail to adequately describe some aspects of the bulk magnetic behaviour.

Quantitative surface structure determination using co-axial impact collision scattering spectroscopy (CAICISS) and low energy electron diffraction (LEED I-V) has been performed on the MnSb(0001)-(2×2) reconstruction. In total, 68 unique surface structures have been trialled, with none of them fitting the experimental data to any degree of satisfaction. A number of key observations have however still been made. Firstly, the LEED I-V suggests the MnSb is bulk-terminated with antimony and consists of a manganese-rich surface layer. This agrees with RHEED observations made during and after growth. However, both the CAICISS and LEED I-V data show the surface region to be six-fold symmetric, in direct contradiction with the bulk symmetry. In addition, the CAICISS data indicates the bulk structure is not preserved all the way to the surface,

with the Sb–Sb and Mn–Mn layer separations being approximately equal. This suggests the structure of the outermost MnSb layers deviate significantly from the bulk structure and has profound implications for the surface magnetic and electronic properties, as well as for epitaxial growth with MnSb acting as the substrate.

Abbreviations and common symbols

2D	...	Two dimensional
3D	...	Three dimensional
AFM	...	Atomic force microscopy
α	...	Linear expansion co-efficient
a_{GaAs}	...	GaAs lattice parameter, 5.6533 Å
BEP	...	Beam equivalent pressure
BFG	...	Beam flux gauge
BP	...	Binary pnictides
CAICISS	...	Co-axial impact collision scattering spectroscopy
c-MnSb	...	MnSb in the zinc-blende cubic structure
c-NiSb	...	NiSb in the zinc-blende cubic structure
DFT	...	Density functional theory
DOS	...	Density of states
E_F	...	Fermi energy, or Fermi level
FR	...	Flipping ratio
FWHM	...	Full width at half maximum
J	...	Beam flux ratio, defined as BEP(transition metal)/BEP(Sb)
GMR	...	Giant magnetoresistance
$\hbar$	...	Reduced Planck's constant, 1.055×10^{34} Js
H_c	...	Coercive field
HMF	...	Half-metallic ferromagnet
IB	...	Ion bombard
IBA	...	Ion bombard and anneal
IMFP	...	Inelastic mean-free path
k_B	...	Boltzmann's constant, 1.381×10^{-23} m^2 kg s^{-2} K^{-1}
KKR	...	Korringa, Kohn and Rostoker Green's function DFT methodology
SPRKKR	...	The Munich implementation of KKR
LEED	...	Low energy electron diffraction
μ_B	...	Bohr magneton, 5.788×10^5 eV T^{-1}
MBE	...	Molecular beam epitaxy
m_e	...	Mass of the electron, 9.109×10^{-31} kg
n-MnSb	...	MnSb in the niccolite structure
n-NiSb	...	NiSb in the niccolite structure
NIST	...	National Institute of Standards and Technology
NSLS	...	National Synchrotron Light Source, USA
$\mathbf{Q}$	...	Momentum transfer of a scattered electron or photon
Q_x, Q_y, Q_z	...	x, y and z components of momentum transfer vector, $\mathbf{Q}$
RHEED	...	Reflection high energy electron diffraction
R_P	...	Pendry r-factor
RSM	...	Reciprocal space map

SADP	...	Selected area diffraction pattern
SEM	...	Scanning electron microscopy
SP	...	Spin-polarisation
SPLEEM	...	Spin-polarised low energy electron microscopy
SQUID	...	Superconducting quantum interference device
T_C	...	Curie temperature
TEM	...	Transmission electron microscopy
TEY	...	Total electron yield
TOA	...	Take off angle
T_{sub}	...	Substrate temperature
V_0	...	Real component of the muffin-tin potential
V_{0i}	...	Imaginary component of the muffin-tin potential
VB	...	Vacancy buckling
VSM	...	Vibrating sample magnetometry
w-MnSb	...	MnSb in the wurtzite structure
w-NiSb	...	NiSb in the wurtzite structure
XAS	...	X-ray absorption spectroscopy
XMCD	...	X-ray magnetic circular dichroism
XPS	...	X-ray photoelectron spectroscopy
XRD	...	X-ray diffraction
XRMS	...	X-ray resonant magnetic scattering

Chapter 1

Introduction

1.1 Motivation

A large part of solid state theory assumes a crystal which is periodic in three spatial dimensions. The introduction of defects within a material system can lead to quite dramatic changes in physical and electronic properties. The surface is essentially a special kind of defect which breaks the three-dimensional (3D) periodicity and, amongst other things, leads to surface structures which can be quite different from an idealised bulk-terminated substrate, to the appearance of band gap states. Understanding these changes in physical and electronic properties at the surface is of paramount importance in device physics; as electrical components shrink, the surface region plays an ever increasing role in the behaviour of an electronic device.

Other issues also arise as devices become ever smaller. For example, quantum mechanical tunnel currents between different parts of a device will exponentially increase as characteristic length scales decrease. Therefore, there is a limit below which miniaturisation becomes impractical. New devices are sought after which negate this leakage current problem as well as operate at higher frequencies and consume less power than today's electronic devices. One way to achieve these goals is to manipulate electrons not only by using their charge but by taking advantage of their quantum mechanical spin, leading to so called spin electronic, or spintronic, devices. These were first conceived after the discovery of the giant magnetoresistence effect (GMR) [1, 2], which is where the electrical resistance of a ferromagnetic multilayer changes depending upon the relative orientations of the layer magnetisations. However, a wide range of new and

novel devices have now been conceived, ranging from spin field effect transistors [3], spin valves [4], combined storage-logic components [5], "spin batteries" [6] and even single-electron entrapment allowing quantum computation.

Some passive spintronic-based commercial products made from metallic multilayers have already found large scale success. In 2000, the first computer hard disks making use of GMR were released, while magnetoresistive random access memory (MRAM) is a well developed, non-volatile data storage medium which is faster than "flash" memory but does not suffer from rewrite fatigue [7]. However, active semiconductor spintronic devices which are compatible with current industrial techniques are highly sought after. This imposes some fundamental requirements which need to be met. Firstly, the semiconductor spintronic device needs a source of spin polarised electrons. Secondly, this spin polarised current needs to remain coherent over operational length and time scales encountered in a commercial device. Thirdly, the spin state needs to be manipulated and detected.

The second issue relating to coherence is thought to have been largely solved. Experiments on GaAs have shown spin polarised currents to be coherent over length scales of up to 4 μm, which is orders of magnitude larger than necessary [8].

The detection and manipulation of spin polarised current is the most well developed aspect of the three requirements. Individual electron spins can be made to precess by the application of a static electric field perpendicular to the spin polarised current, an effect known as the Rashba effect and described by Datta and Das [3]. Andreev reflection and photo- and electro- luminescence in light emitting diode structures can all be used to detect the state of the spin polarised current. However, a more compact solid state method of detection is strongly preferable, such as one making use of GMR and ferromagnetic contacts.

The first of these requirements is in principle relatively straightforward. Ferromagnets necessarily have a degree of spin polarisation at the Fermi energy. Application of an electric field will lead to a spin polarised current, but efficient injection of this cur-

rent into a semiconductor remains the key problem. Spin dependent scattering processes at semiconductor/metal interfaces can lead to significant reductions in the spin polarisation. The most promising method of spin injection is to use a tunnel junction such as an ultra thin metal-oxide layer between the metal and semiconductor [5, 9, 10] but this requires the oxide to be epitaxially compatible with both the ferromagnetic metal and the semiconductor into which the spin current is to be injected. However, and most importantly, whilst a material may be ferromagnetic in the bulk, the interface between a ferromagnet and semiconductor may not be, or if it is, the spin polarisation may be reduced. This change is driven by the reduction from three to two dimensional periodicity in the vicinity of the interface and affects all spin injector materials in all spintronic devices. Understanding how interface structure affects the magnetic properties and thus the spin polarisation at the Fermi energy at the interface is of vital importance.

Any successful spin injector material needs to satisfy a number of conditions. Firstly, a spin injector must be capable of delivering a current with significant spin polarisation. The degree of spin polarisation in the injected current will depend upon the injection regime (tunnelling, ballistic or diffusive transport across the interface) but generally the larger the spin polarisation at the Fermi level, E_F, the larger the degree of spin polarisation in the injected current. Secondly, any spin injector material needs to be compatible with existing industrial and commercial techniques and materials. In practice, this means the material needs to form stable and abrupt interfaces with a range of tetrahedrally coordinated semiconductors, for example GaAs and Si, can be grown using molecular beam epitaxy or sputtering and patterned using UV and electron beam lithographic techniques.

A fairly straightforward approach would be to use elemental ferromagnets such as iron and nickel, however chemical intermixing at the interface prohibits the formation of stable and abrupt interfaces which are required for efficient spin injection [11]. A second approach would be to dope a tetrahedrally coordinated semiconductor with magnetic ions. At a critical magnetic ion density, a spontaneous magnetisation will arise enabling

the injection of a spin polarised current. The level of doping required to achieve this is of the order of a few atomic percent, ensuring epitaxial compatibility with zinc-blende semiconductors. However, the Curie temperatures of these materials is often well below room temperature, making them unsuitable for the majority of commercial applications.

A third and much more promising approach, is to make use of compound ferromagnets. A vast array of such materials exist, from the binary pnictides, e.g. MnAs and MnSb, to so-called half-metallic ferromagnets such as NiMnSb. They have good epitaxial compatibility with III-V semiconductors, forming stable and abrupt interfaces. However, the degree of spin polarisation in injected currents has yet to be unambiguously determined experimentally for most of these hybrid multilayer structures. Moreover, the fine structural details at their interfaces with III-V semiconductors is unknown.

1.2   Organisation of the thesis

This work concerns the growth, structural and magnetic characterisation of MnSb and NiSb thin films. The remainder of this chapter is dedicated to introducing the magnetic, electronic and structural properties which makes MnSb and NiSb interesting prospects for spintronics applications, as well as the basic notation and concepts used within surface physics.

The nature of this work has necessitated the use of a wide range of *in situ* and *ex situ* techniques. Chap. 2 contains an introduction to these techniques, including background theory and experimental schematics and, where relevant, an introduction to the theoretical methods and simulation packages which have been used to analyse the experimental data.

Chap. 3 is the first of the experimental results chapters and details the work undertaken in growing epitaxial NiSb(0001) thin films on GaAs(111)B substrates. This chapter combines SEM, XPS and XRD data in order to elucidate on the surface morphology, surface stoichiometry and crystal structure respectively. On the basis of these

results, an optimised set of growth conditions are proposed.

Chap. 4 is concerned with the epitaxial growth of MnSb(0001) on GaAs(111) substrates. The first section of Chap. 4 details the growth conditions which have been employed during this work and highlights the changes and additions to the original conditions proposed by Hatfield which have been made during this project. Sec. 4.2 contains a detailed x-ray photoelectron spectroscopy (XPS) study of MnSb(0001) samples which have been exposed to atmospheric conditions and subjected to a variety of preparation methods. On the basis of the XPS results, a surface preparation method is proposed with XPS and low energy electron diffraction (LEED) data shown to demonstrate its efficacy. In Sec. 4.3, a study of the effects of different beam flux ratios, J, on the final film structure and morphology of MnSb(0001) is presented.

The bulk and surface magnetic properties of the epitaxial MnSb thin films are the subject of Chap. 5. The chapter is split into two distinct sections. The first relates wholly to the the bulk magnetic properties which were probed using a combination of vibrating sample magnetometry (VSM) and the superconducting quantum interference device (SQUID). Sec. 5.2 contains the polarised soft x-ray work which was undertaken to: (a) determine if a magnetic surface could be obtained from an air contaminated thin film; (b) determine any qualitative differences between the bulk and the surface of the film; and (c) demonstrate that an Sb-capping procedure is capable of preventing oxidation of the surface.

The final experimental results chapter, Chap. 6, focusses on the two quantitative surface structure techniques which have been used during this project, namely LEED I-V and CAICISS. The different surface structures which have been trialled during this work are given in Sec. 6.1 with the experimental and simulated data given in Sect. 6.3 and Sec. 6.2 for LEED I-V and co-axial impact collision ion scattering spectroscopy (CAICISS) respectively.

Finally, Chap. 7 contains a final conclusion of the work undertaken before underlining some of the questions which have arisen during this work. This includes proposals

for further investigation of the NiSb(0001)/GaAs(111) growth system, the use of additional quantitative surface structure techniques to further narrow down the MnSb(0001)-(2×2) structural model as well as some basic modifications which could be made to the growth chamber.

1.3   Spintronics applications for MnSb and NiSb

Most basically, MnSb natively adopts the "niccolite" structure and is described as being a p-type semimetal with a carrier concentration of $\sim 10^{22}$ cm^{-3} and orders ferromagnetically below a Curie temperature of 587 K [12, 13]. The semimetallic behaviour of MnSb arises due to a complex Fermi surface, where the hole-pockets are larger than the electron pockets. A crude schematic of how this might arise is shown in Fig. 1.1(b), with a direct gap semiconductor shown in (a) for comparison. The spin-polarisation (SP) for MnSb at E_F is only $\sim$20% which does not make it particularly attractive for spintronics. However, it demonstrates a particularly large Kerr effect [14], which is enhanced after oxidation of the surface [15], giving it possible application in magneto-optical devices and in waveguides [16]. Moreover, MnAs nanoparticles used in semiconductor heterostructures show a huge magnetoresistive effect as well as the induction of an electromotive force with the application of a static magnetic field [6]. Such "spin-batteries" could be devised and constructed from MnSb.

It is worth stating some potentially very important and hugely attractive features of MnSb and related compounds. Firstly, NiSb is paramagnetic [17] and CrSb is an antiferromagnet [18]. Given these different magnetic responses spin valves and other spintronic devices constructed from these three materials are simple in both concept and design. However, of perhaps greater importance is the magnetic and electronic properties of the binary pnictides in the cubic and wurtzite structures, as theoretical calculations show that a range of BPs, including CrSb and MnSb, are half-metallic ferromagnets (HMFs) [19, 20, 21]. In such a material, the majority spin channel has a non-zero density of states at E_F, whereas the minority spin channel has a band gap
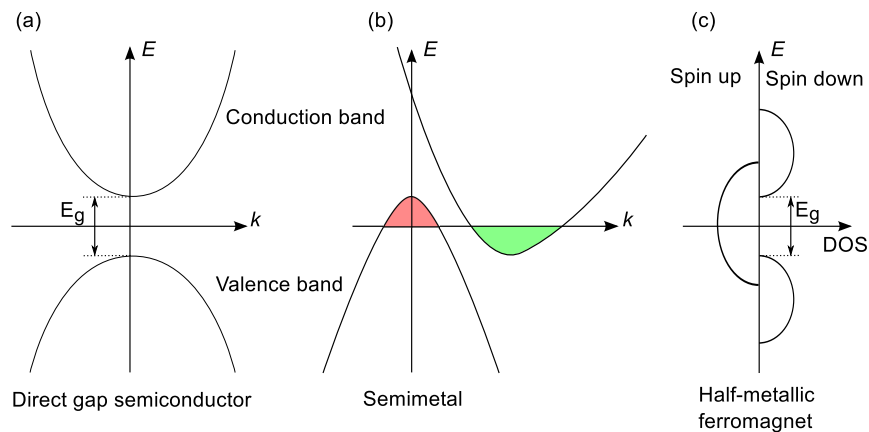
Figure 1.1: *A schematic of the band structure of: (a) a direct band gap semiconductor; (b) a semimetal with empty states in the valence band (red) and filled states in the conduction band (green); (c) a half-metallic ferromagnet.*

which straddles E_F [22], leading to 100% spin-polarisation of the conduction electrons. A crude illustration of this type of bandstructure is shown in Fig. 1.1(c). In addition, recent DFT calculations show the SP of cubic MnSb (c-MnSb) is more robust against variations in temperature, doping and strain than the prototypical HMF, NiMnSb [23]. These cubic BP phases are clearly highly attractive for spintronics applications but little experimental evidence of their existence can be found in the literature, with the most convincing evidence being the growth of ultra-thin films of CrSb on rock salt substrates [24, 25]. The reason so few examples of these highly promising materials exist in the literature is because the equilibrium energy of these cubic and wurtzite (w-MnSb) phases is larger than the equilibrium energy of the niccolite phase, meaning c-MnSb is unlikely to be seen in bulk form. However, MBE growth is a non-equilibrium dynamical process, so these additional structural phases could possibly be encouraged through such means as strain engineering.

1.4   Crystal structure of binary pnictides

The class of material to which MnSb and NiSb belong is known as the binary pnictides, with NiAs (niccolite) being the prototypical example. These compounds consist of
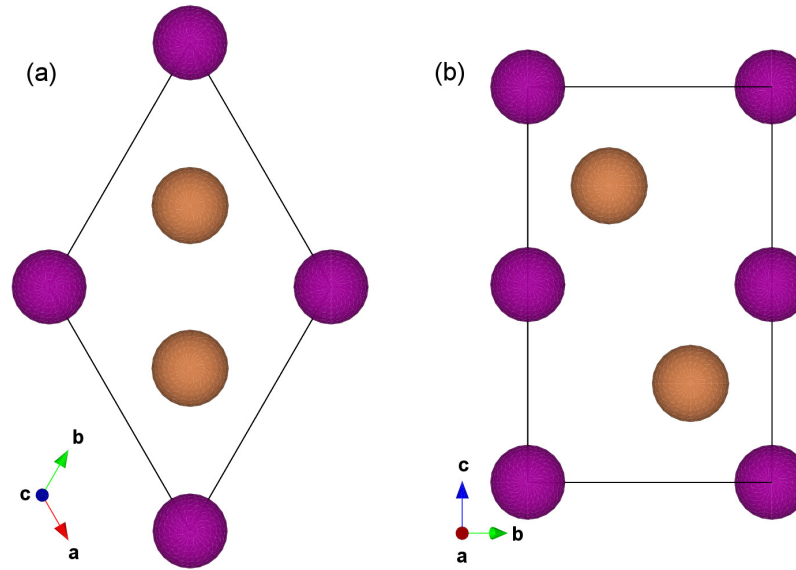
Figure 1.2: *(a) Top-down view of the NiAs structure along the [0001] direction. (b) Side-on view of the unit cell along the [1̄100] direction.*

a transition metal atom bonded to a pnictogen, such as arsenic or antimony, with the atomic arrangement consisting of a double hexagonal structure of space group P6$_3$/mmc. The layer stacking is described as 'ABAC' with the transition metal occupying 'A' sites and the pnictogen occupying the alternating 'B' and 'C' sites. The atomic basis set which describes this structure is

$$\mathbf{B}_1 = 0 \qquad\qquad\qquad\qquad\qquad \text{(Ni)}$$

$$\mathbf{B}_2 = \frac{1}{2}\mathbf{A}_3 \qquad\qquad\qquad\qquad \text{(Ni)}$$

$$\mathbf{B}_3 = \frac{1}{3}\mathbf{A}_1 + \frac{2}{3}\mathbf{A}_2 + \frac{1}{4}\mathbf{A}_3 \quad \text{(As)}$$

$$\mathbf{B}_4 = \frac{2}{3}\mathbf{A}_1 + \frac{1}{3}\mathbf{A}_2 + \frac{3}{4}\mathbf{A}_3 \quad \text{(As)}$$

where $\mathbf{A}_{1,2,3}$ label the primitive unit vectors in Cartesian coordinates. The magnitude of vectors $\mathbf{A}_1$ and $\mathbf{A}_2$ is the lattice parameter a, while the magnitude of $\mathbf{A}_3$ is the lattice parameter c. By convention, the primitive lattice vectors satisfy a right-handed basis set, the internal angle between $\mathbf{A}_1$ and $\mathbf{A}_2$ is 120° and both of these are perpendicular to $\mathbf{A}_3$. Fig. 1.2, which was made using the VESTA software package [26], shows this
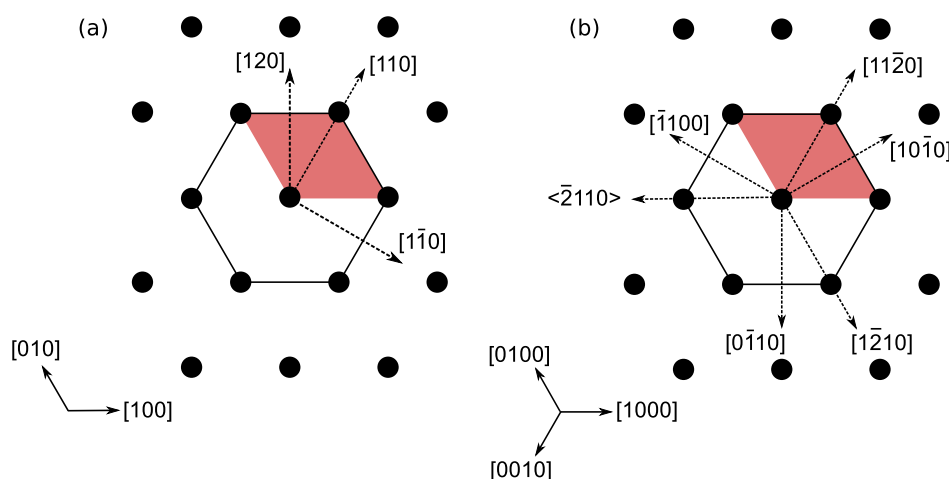
Figure 1.3: *Directions in hexagonal structures using (a) three index notation (b) four index notation. When resolved in the (0001) plane, pnictogen bonds are found to lie parallel to directions of the from [1$\bar{1}$00] only. Families of equivalent directions can be determined by simple permutation of the hki indices. The shaded area denotes the bulk-truncated (1×1) surface mesh.*

structure.

Convention for labelling crystallographic directions

The labelling of crystallographic directions in hexagonal lattices can lead to confusion. Using the conventional three index notation, Fig. 1.3 shows the confusion which can arise: the [1$\bar{1}$0] direction is symmetrically equivalent to [120] but inequivalent to [110]. Instead, four indices [$hkil$] are commonly used. In this system [h000], [0k00] and [00i0] all denote primitive lattice directions separated by 120° in the basal plane. Crystallographic directions are then constructed from a combination of these directions, as shown in Fig. 1.3, and in such a way that $i = -(h+k)$. This means that i is technically a dummy index, but it does help highlight the crystal symmetry and remove confusion, as in this notation the directions [2$\bar{1}\bar{1}$0], [$\bar{1}$2$\bar{1}$0] and [$\bar{1}\bar{1}$20] are all equivalent. Directions which lie along the long diagonal of the primitive unit cell take the form of [1$\bar{1}$00]. This notation is convenient not least because equivalent directions in the basal plane can be found by permuting the order of hki, but also because Mn-Sb bonds when resolved

in the (0001) plane never lie parallel to $[2\bar{1}\bar{1}0]$-type directions and only lie parallel to $[1\bar{1}00]$-type directions. This notation is used in this thesis.

Crystals adopting the NiAs structure are strictly only three-fold symmetric. The transition metal atom adopts a simple hexagonal structure which is itself 6-fold symmetric, but the pnictogen occupies alternating 'B' and 'C' sites which describes an hexagonal closed packed (hcp) lattice leading to three-fold symmetry. For a bulk-truncated (0001) crystal, this symmetry is preserved all the way to the surface but steps of $c/2$ add a complication, as the bond direction between terraces separated by $c/2$ steps is rotated by $60°$. A surface which consists of many such terraces is essentially two domain and may therefore appear to have six-fold symmetry in diffraction techniques such as LEED and RHEED.

1.5 Surface reconstruction and Wood notation

In the case of the zincblende III-V semiconductors, surface reconstruction is an inevitable consequence of the loss of 3D periodicity. In the bulk, each atom forms four covalent bonds, each bond filled with two electrons of opposite spin. In creating a surface, some bonds are broken and are left partially filled. In the simplest case of {001} surfaces, two bonds are broken, leaving two partially filled dangling bonds. These dangling bonds are energetically unfavourable [27] and so the surface atoms will attempt to change their co-ordination in order to fill (or empty) these dangling bonds and reduce the total energy [28, 29]. As a result, the chemical composition and structure of the outermost layers may be different from an idealised bulk terminated crystal [30].

The situation is marginally more complex for {111} surfaces of III-V materials. With specific references to GaAs, a (111) surface is wholly gallium terminated with three back-facing bulk bonds to arsenic atoms and one dangling bond perpendicular to the surface. This is shown in Fig. 1.4. In this case, removing the outermost layer of gallium atoms leaves an arsenic-terminated surface, with three dangling bonds and a
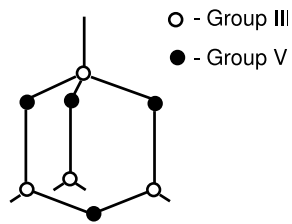
Figure 1.4: *Ball-and-stick model of GaAs(111).*

single back-facing bulk bond per atom. This is sufficiently unenergetically favourable that these arsenic atoms desorb from the surface, resulting in a gallium terminated surface. This surface is denote as (111)A. On the opposite side of a (111)A surface are arsenic atoms with one dangling bond and three back-facing bulk bonds. This surface is thus always terminated with arsenic and is designated (111)B.

Metal surfaces are also subject to surface reconstructions for ultimately the same reason, i.e. to reduce the total surface energy. However, the bonding in metals is much less directional than that of covalently bonded semiconductors, so there are far fewer examples of clean metal surfaces undergoing reconstruction, other than simple inward or outward relaxation. Adsorbate induced reconstruction is more common and has been investigated extensively due to the connection with catalytic and industrial processes [31, 32, 33, 34].

As a brief aside, it is also worth nothing that the interface between substrate and epilayer is itself only 2D periodic. In this region, the local atomic structure of both the epilayer and substrate may differ from that of an idealised truncated bulk in order to minimise the total energy, in the same way that a free surface reconstructs. Only surface reconstructions are considered in what follows, but interface structure can play a significant role in heteroepitaxy.

There exist two methods of relating the symmetry and lattice vectors of the surface to that of the bulk, the most general of which is the matrix notation proposed by Park and Madden [35]. The method uses a simple relationship between the two sets of translation vectors. If the primitive lattice vectors of the bulk net are denoted **a** and

$\mathbf{b}$ and those of the surface are $\mathbf{a}'$ and $\mathbf{b}'$, then

$$\begin{pmatrix} \mathbf{a}' \\ \mathbf{b}' \end{pmatrix} = G \begin{pmatrix} \mathbf{a} \\ \mathbf{b} \end{pmatrix}$$

where the the matrix G is defined

$$G = \begin{pmatrix} G_{11} & G_{12} \\ G_{21} & G_{22} \end{pmatrix}$$

yielding

$$\begin{aligned} \mathbf{a}' &= G_{11}\mathbf{a} + G_{12}\mathbf{b} \\ \mathbf{b}' &= G_{21}\mathbf{a} + G_{22}\mathbf{b} \;. \end{aligned}$$

Whilst this is entirely general and can accommodate situations when an overlayer or adsorbate is incommensurate with the substrate, for most situations a much more convenient notation devised by Wood is used [36]. For the $\{hkl\}$ surface of material X, if $|\mathbf{a}'| = p|\mathbf{a}|$ and $|\mathbf{b}'| = q|\mathbf{b}|$, and if the surface mesh is rotated by an angle ϕ relative to the bulk mesh, then

$$X(hkl)-(p \times q)\,R\phi^{\circ} \tag{1.1}$$

For the case when there is no rotation between the surface and substrate nets, the $R\phi^{\circ}$ term is dropped. If an adsorbate, A, deposited onto a surface leads to a reconstruction, "$-A$" is added as a suffix. Finally, several minor modifications exist, such as using $\mathsf{p}(2 \times 2)$ and $\mathsf{c}(2 \times 2)$ to denote respectively a primitive or centred (2×2) reconstruction. Less commonly used in the literature, but used extensively in this thesis, is the use of "td" to denote a triple domain surface, for example $\mathsf{td}(1 \times 3)$.

Chapter 2

Experimental techniques

2.1 Molecular beam epitaxy

Molecular beam epitaxy (MBE) was first achieved with III-V semiconductors by Arthur [37] and Cho [38] at Bell Laboratories in the latter part of the 1960s. The method allows for the controlled growth of thin film crystalline materials on substrates composed of either the same (homoepitaxy) or different (heteroepitaxy) material. The principal advantages of this technique over other growth methods are its relative simplicity, the ability to control the layer thickness to the sub-monolayer level, the ability to "fine tune" electronic properties such as the band gap through epitaxial strain and the growth of multilayer structures. The technological applications for this technique are thus enormous, allowing the manufacture of such devices as light emitting diodes, solid state laser structures and microprocessors.

The method of MBE is a very straightforward one, where shuttered cells containing the source material are heated to form molecular beams which are directed towards the substrate. This process does however necessitate the use of ultra high vacuum (UHV) chambers. The background pressure inside the growth chamber needs to be sufficiently small such that the inelastic mean free path of the atoms or molecules in the molecular beams is larger than the geometrical size of the chamber. This is easily fulfilled provided the pressure is less than 10^{-5} mbar. However, it is important that the density of contaminants incorporated into the growth layer remains as low as practicable. This is particularly important where either or both of the electronic properties and crystallographic structure are adversely affected by the incorporation of contaminants
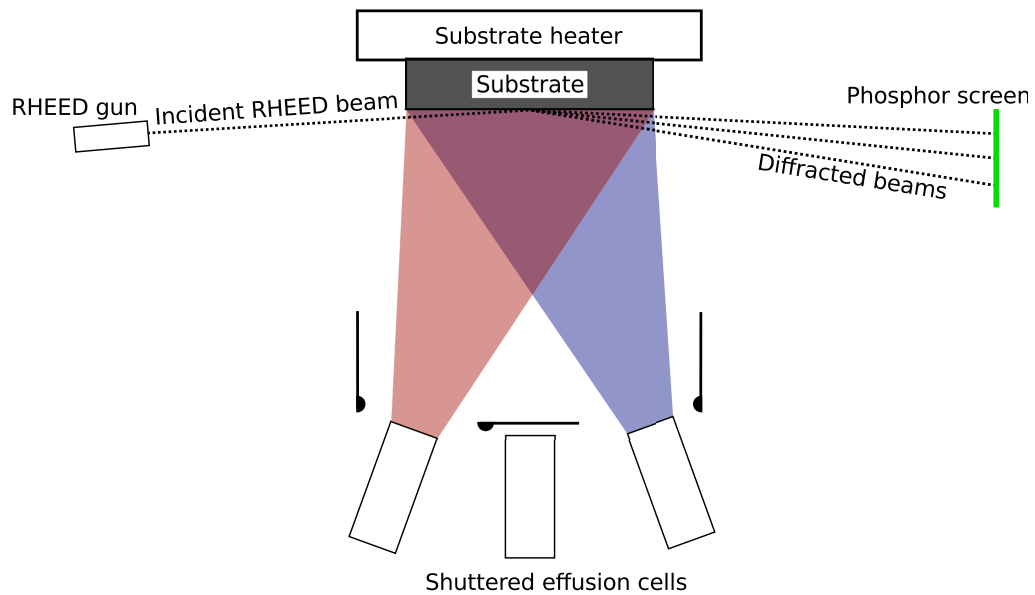
Figure 2.1: *A schematic of a typical MBE chamber. Shuttered effusion cells with the source material are directed towards a sample substrate heated to the required temperature for high quality growth of the overlayer. Grazing incidence electron diffraction using RHEED allows in situ monitoring of the surface.*

typically found in properly baked vacuum chambers, i.e. H_2, H and CO. This requirement imposes a much stricter condition on the base pressure and necessitates the use of UHV, where background pressures should be below $\sim 10^{-9}$ mbar [39].

A schematic of the main components of a typical growth chamber is shown in Fig. 2.1. A target substrate is usually affixed to a removable sample plate or holder which is inserted into a manipulator, with the substrate facing shuttered effusion cells. This geometry allows the use of reflection high energy electron diffraction to qualitatively assess the surface crystallinity and surface roughness, and quantitatively determine the symmetry, growth orientation and surface reconstruction. More detailed discussions of the RHEED technique are reserved for Sec. 2.2.3. The shuttered effusion cells depicted in Fig. 2.1 typically consist of a pyrolytic boron nitride (PBN) crucible and are heated using either a hot filament in direct thermal contact with the crucible or by electron beam (e-beam) heating. The method of heating used depends on the growth material. Source materials exhibit a vapour pressure-temperature behaviour following the Clausius-

Clapeyron equation

$$P = A \; exp\left(\frac{-\Delta H}{RT}\right). \tag{2.1}$$

where P is the beam equivalent pressure as measured by a pressure gauge in the path of the beam (beam flux gauge, BFG), ΔH is the enthalpy of evaporation or sublimation, whichever is appropriate for the source material at a temperature T and R is the molar gas constant. For materials such as antimony, beam pressures of 10^{-5} mbar are readily achieved using PBN crucibles directly heated by a metal filament due to its low enthalpy of sublimation. Other materials, such as nickel, have considerably larger enthalpies of sublimation than that of antimony [40] making this method of sublimation technically difficult. For these materials, heating through electron bombardment (e-beam) is the preferred method, often with rods of high purity ($\geq$99.99% pure) source material exposed in the vacuum. In both cases however there is a need to ensure the beam pressures are stable over the growth time. For materials such as antimony, the source temperature is typically stabilised using thermocouples and a PID control regulating the power output from the cell's power supply. For e-beam heated cells, the HV drain current is stabilised using a PID feedback loop controlling the filament current. In this work the antimony and manganese cells are of the first type, with heater filaments in direct contact with PBN crucibles. Nickel is sublimated into the Warwick growth chamber using the latter method, with a nickel rod of 99.99% purity exposed to a 30 mA, $\sim$2.2 keV electron beam.

Atoms and molecules arriving at the substrate surface can undergo a number of atomistic processes as depicted in Fig. 2.2. Each of these processes have an associated barrier height, E_b, and the rate at which each process occurs, R_b, is simply related to the absolute temperature, T, of the surface

$$R_b = \nu_0 \; exp\left(\frac{-E_b}{k_B T}\right) \tag{2.2}$$

where ν_0 is the attempt frequency and is related to the lateral vibrations of the atom.
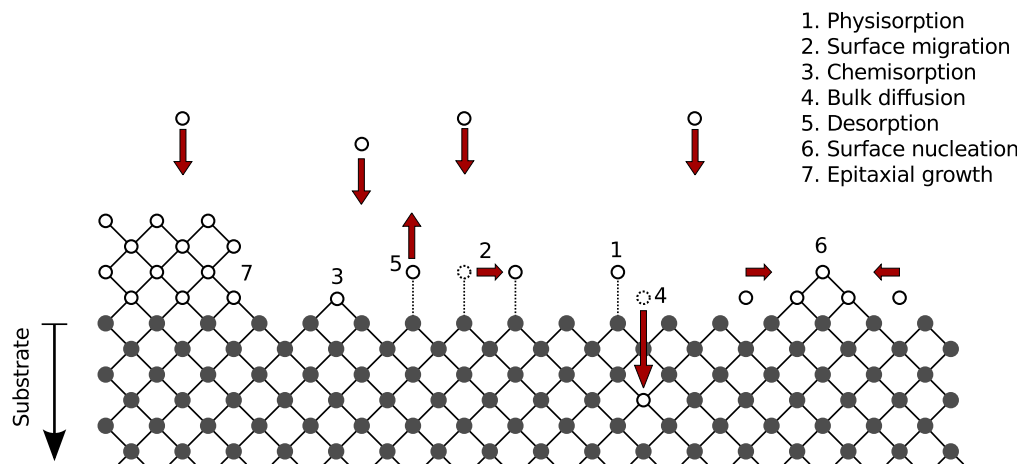
Figure 2.2: *An illustration of the processes which can occur at surfaces during growth.*

Upon arrival at the surface, the atoms can become weakly bound (physisorbed) through the van der Waals interaction or chemically bond (chemisorbed) to the substrate. In order for the film to grow, atoms must migrate and become incorporated at an epitaxial site and adopt the bulk-like bonding configuration of the growth layer. The speed with which this happens and the quality and morphology of the resultant thin film is dependent upon a number of factors. Firstly the substrate temperature plays a key role in affecting the desorption rate of atoms from the substrate surface as well as the ability for atoms to migrate on the surface. Secondly the beam flux ratio (BFR) determines the relative abundance of the growth elements which in turn is closely related to the chemical potential at the surface. The chemical potential is particularly important as it determines the relative desorption rates, also known as the sticking co-efficient [37]. Finally, the lattice mismatch between the substrate and growth layer plays a vital role. This mismatch can correspond to a structural difference, such as a hexagonal crystal on a cubic substrate, or more commonly to the difference between the in-plane lattice parameters of the growth layer and substrate. For systems where the symmetry of the substrate and growth layer are the same, films of a few monolayers will be strained to match the substrate and form a perfect registry between the two. As the layer grows thicker the homogeneous strain energy increases until it becomes energetically preferable

(a)   (b)   (c)

Frank-van der Merwe   Volmer-Weber   Stranski-Krastanov
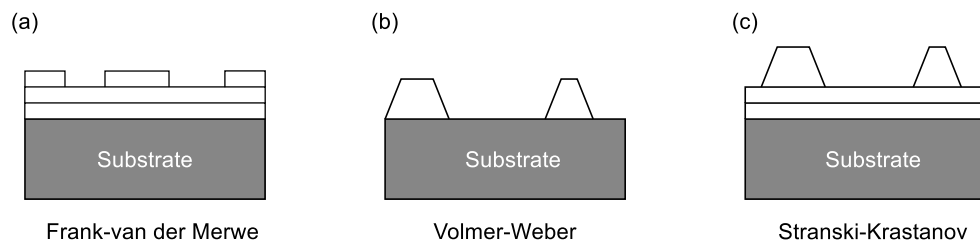
Figure 2.3: *The three idealised growth modes. a) Layer-by-layer growth b) Three dimensional island growth c) Three dimensional island formation with a wetting layer.*

for the strain to relax through the formation of defects and misfit dislocations.

The mode through which the growth proceeds is affected not only by the strain energy and strain relaxation mechanisms but also by the interactions between the growth atoms and their interactions with the substrate. For most applications layer-by-layer growth, known as the Frank-van der Merwe growth mode, is preferred. This mode is where one atomic layer completes before another starts and is shown schematically in Fig. 2.3(a). However, there are cases where the interactions between growth atoms is much larger than the interactions between growth atoms and substrate. In this case the 3D island or Volmer-Webber growth mode depicted in Fig. 2.3(b) is preferred. There is a hybrid mode between the two, where an initial wetting layer gives way to 3D island formation as shown in Fig. 2.3(c). This is known as the Stranski-Krastanov mode and is, for instance, observed in the growth of semiconductor quantum dots [41, 42].

These three modes are of course idealised and a variety of other modes exist. For instance crystallographically oriented nanorods can spontaneously grow in-plane or be made to grow out-of-plane from the substrate surface [43, 44, 45]. Another growth mode which cannot be described using any of modes discussed is known as endotaxy and is where oriented crystallites grow into the substrate as a result of high chemical reactivity at the interface. This type of growth mode is seen with MnSb on InP(111) [46] and MnSb on GaSb(001) [47].

2.2 Electron diffraction

X-ray diffraction has found many uses in materials characterisation but its key strength is also its limitation, that being the inelastic mean free path of x-rays in matter is up to a few μm making the technique surface insensitive. Several methodologies exist which increases the surface specificity of XRD but these techniques generally require the use of synchrotron radiation. The field of electron diffraction has developed as a surface specific technique to give quantitative information on the surface symmetry and structure. This section outlines the important details of two electron diffraction techniques: low energy electron diffraction (LEED) and reflection high energy electron diffraction (RHEED). Sec. 2.2.2 details the methods employed to perform quantitative surface structure determination using LEED I-V.

2.2.1 Low energy electron diffraction

Much of the mathematical description of bulk XRD is applicable to electron diffraction. That is, coherent elastic scattering is needed for the formation of diffraction beams. This simply means that energy and momentum must be conserved

$$E = \frac{\hbar^2 |\mathbf{k}|^2}{2m_e} \tag{2.3a}$$

$$E_f = E_i \tag{2.3b}$$

$$|\mathbf{k}_f| = |\mathbf{k}_i| \tag{2.3c}$$

where E_i and $\mathbf{k}_i$ ($\mathbf{k}_i$, E_f) are the energy and wavevector of the incident (scattered) electron respectively and other symbols have their usual meanings [48]. For diffraction in 3D, $\mathbf{k}_i$ can change only by discrete amounts according to the 3D reciprocal lattice, $\mathbf{G}_{ijk}$, of the scattering crystal,

$$\mathbf{k}_f = \mathbf{k}_i + \mathbf{G}_{ijk}. \tag{2.4}$$
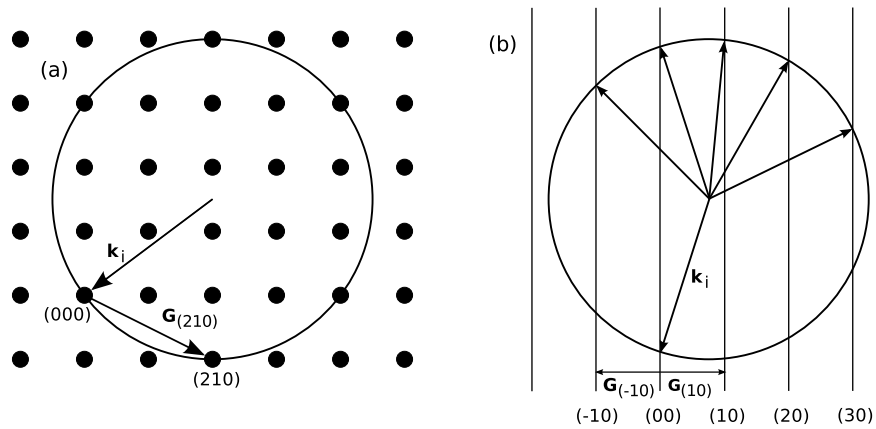
Figure 2.4: *The Ewald sphere construction for a) 3D periodic structure and b) a 2D periodic structure.*

Eqs. 2.3c and 2.4 lead to the von Laue diffraction condition

$$|\mathbf{G}_{ijk}|^2 + 2\mathbf{k}_i \cdot \mathbf{G}_{ijk} = 0. \tag{2.5}$$

These conditions can be depicted graphically using the Ewald sphere construction and is shown in Fig. 2.4(a) [48]. In this construction, a circle of radius $|\mathbf{k}_i|$ is drawn on a 2D projection of the reciprocal lattice with an arrow of length $|\mathbf{k}_i|$ terminating at the (000) spot. All reciprocal lattice points which are intersected by the circle satisfy Eqns. 2.3–2.5 and hence generate diffraction spots.

For the case of scattering from a 2D surface, the reciprocal lattice vector defined above becomes $\mathbf{G}_{ij}$ due to the loss of periodicity perpendicular to the surface. This means that momentum parallel to the surface plane must be conserved, but the condition is relaxed perpendicular. Eq. 2.4 thus becomes

$$\mathbf{k}_i^{\parallel} = \mathbf{k}_i^{\parallel} + \mathbf{G}_{ij} \tag{2.6}$$

where the superscripts denote a direction parallel to the surface plane. Furthermore, with the relaxation of momentum conservation perpendicular to the surface, reciprocal lattice points become reciprocal lattice "rods" which extend perpendicular to the surface
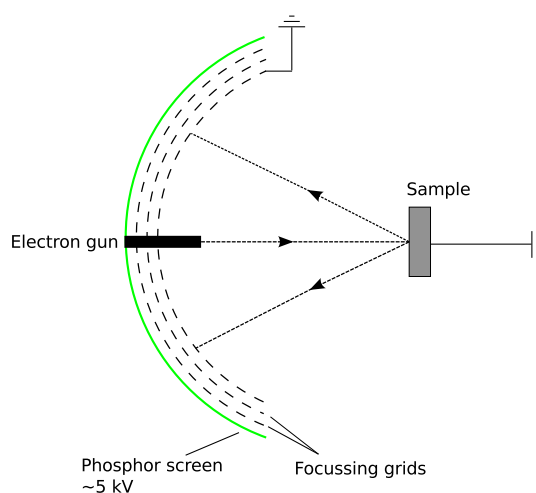
Figure 2.5: *A typical LEED experimental geometry. Electrons from an electron gun are directed towards an earthed sample at normal incidence. Inelastically backscattered electrons are filtered and elastically backscattered electrons are focussed using a series of grids. The elastically scattered electrons are finally accelerated through a potential to a phosphor screen on which the diffraction pattern is observed.*

plane. This subtly changes the Ewald sphere construction, as shown in Fig. 2.4(b).

A typical LEED experiment is depicted in Fig. 2.5. Here an electron gun generating a beam of electrons with an energy between 30–500 eV ($\lambda \sim$ 2–0.5 Å) are directed towards the sample. A series of grids reject electrons which are inelastically back scattered and focuses those which have been elastically scattered onto a phosphor-coated screen at potential of $\sim$4–6 kV. Due to the experimental geometry, the pattern of diffraction spots on the phosphor screen is simply a projection of the Ewald sphere and the reciprocal lattice. Careful measurement of the separation between diffracted beams enables the determination of the surface lattice parameter and the geometrical arrangement of the spots indicates the surface symmetry. That is, a square real space lattice will result in a square reciprocal lattice. However it is not possible to use the Fourier Transform (FT) methods common to XRD in order to obtain the real space structure from an electron diffraction pattern. This is because electrons in the diffracted beam have undergone multiple scattering events before emerging from the sample surface. The single scattering, "kinematic" theory discussed so far does not by its very defi-

nition deal with multiple scattering events. Instead, a "dynamical" diffraction theory which explicitly deals with multiple scattering is required. This is the basis for LEED intensity-energy or LEED I-V experiments and is the subject of the following section.

2.2.2 LEED I-V

The first electron diffraction experiments were performed by Davison and Germer in the 1920s [49], but it was not until the early 1970s that a complete theory of electron diffraction emerged. Part of the problem with LEED scattering theory is the interaction cross section for low energy electrons with matter is many orders of magnitude larger than that of x-rays. Indeed, it is this increased cross section which gives LEED its surface specificity, but it also means multiple scattering events play a central role. Moreover, there was some debate during the initial formulation of LEED theory as to what exactly dominates the scattering process: ion core-electron scattering or electron-electron scattering by electrons near the Fermi energy [50, 51]. This was eventually solved by Pendry who demonstrated that scattering from ion cores dominates [52, 53]. This is a hugely important point, especially if LEED is to be used to geometrically optimise a surface structure. Any rearrangement of the atoms in the near surface region results in changes in the bonding configuration and a rearrangement of the electron density. If the scattering was dominated by valence electrons this rearrangement would require the scattering potential to be recalculated at every step. However, the core nuclear potential once calculated for a particular atom is fixed and is largely insensitive to the proximity of nearby atoms.

Strictly, the scattering potential relevant to LEED is non-local. It should include electrostatic contributions from all the atomic nuclei and electrons, exchange-correlation effects and be treated in a self-consistent manner. Generating and using such a potential requires an unfeasible amount of computational effort. Indeed, this problem runs parallel to similar ones encountered within density functional theory (DFT). Just as in some implementations of DFT, the potential used in LEED calculations is a vastly simplified
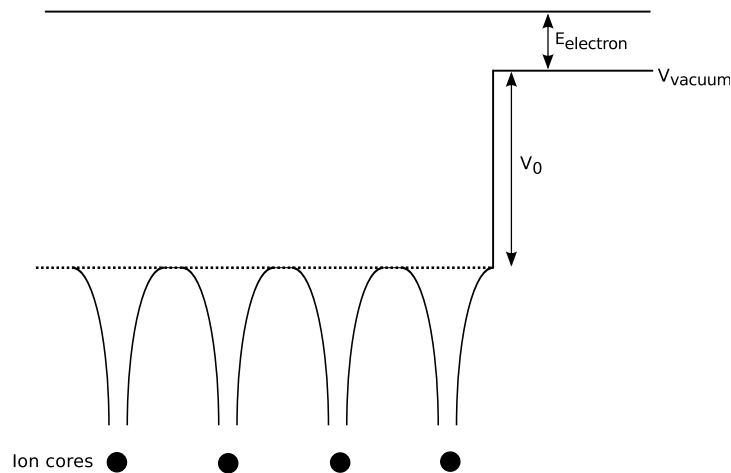
Figure 2.6: *A schematic of the muffin-tin potential for a crystal extending from right to left, with a vacuum/surface interface. Ion cores are surrounded by a spherically symmetric potential with adjacent cores just touching but not overlapping. The potential is set as a constant determined by the average value at the points where spheres touch. An electron of energy $E_{electron}$ relative to the vacuum level will gain an extra amount of energy equal to V_0 as it crosses the surface/vacuum interface.*

one, utilising the one-electron (local) approximation within the "muffin-tin" model [54]. In this model, shown schematically in Fig. 2.6, the potential is split into two distinct regions: within non-overlapping spheres centred on atomic sites ("ion cores") a spherically symmetric potential of radius r_{mt} is assumed, whilst a constant value is taken for the remaining "interstitial" regions. Calculating a muffin-tin potential is a much more tractable problem and is used extensively in LEED, as in DFT.

Before proceeding, a brief comment is needed on the conventions used in the literature. The name given to the value of the constant potential in the muffin-tin model is variously given as the muffin-tin zero, the muffin-tin constant and the real component of the inner potential. The inner potential is a spatial average of the potential the incident LEED electrons experience upon entering the crystal, which includes the space within the ion cores. This value can be measured experimentally: incident electrons gain on average a small amount of energy as they cross the vacuum-surface interface which leads to a rigid shift of the energy scale. In contrast, the muffin-tin constant is purely a construct of the muffin-tin model and by definition does not take into account

the potential within the ion cores. Moreover the inner potential is taken relative to the "vacuum level" whereas the muffin-tin constant is not. However the names are used interchangeably within the literature. In this thesis, the constant potential in the interstitial region will be referred to as the muffin-tin zero, V_0.

In XRD, the atomic scattering factor, f, can be approximated as a real quantity provided the incident photon energy is far enough away from a resonant absorption edge. In LEED, this scattering factor is complex for all incident energies and leads to the scattered wave being phase shifted relative to the incident wave. Each incident electron undergoes numerous scattering events, with each event introducing a phase shift. To account for this, the scattering factor in LEED is typically written as a partial wave of the form [55, 56]

$$f(\theta) = \frac{1}{2ik} \sum_{l=0} (2l+1) \left[\exp(2i\delta_l) - 1\right] P_l(\cos(\theta)) \qquad (2.7)$$

where k is the magnitude of the electron wave vector, l is angular momentum, δ_l is the scattering phase shift and P_l are Legendre polynomials. The scattering phase shifts are dependent upon the atomic species and the wave vector k and play a crucial role in LEED theory. Phase shifts for a given structure and atomic species are calculated using the radial solutions of the Schrödinger equation inside and outside of the ion core and equating the logarithmic derivative on either side of the muffin-tin sphere boundary, r_{mt} [56, 57]. If the solution inside the muffin-tin is denoted $R_l(r_m)$ and $L_l = \frac{R'_l(r_m)}{R_l(r_m)}$, the phase shifts satisfy

$$\exp(2i\delta_l) = \frac{L_l h_l^{(2)}(kr_{mt}) - h_l^{(2)\prime}(kr_{mt})}{h_l^{(1)\prime}(kr_{mt}) - L_l h_l^{(1)}(kr_{mt})} \qquad (2.8)$$

where $h_l^{(1)}$ and $h_l^{(2)}$ are spherical Hankel functions of the first and second kind.

So far, inelastic scattering, electron absorption and finite temperature effects have been neglected. The effect of inelastic scattering and electron absorption can be

accounted for by introducing an imaginary component to the muffin-tin potential, V_{0i}, without changing Eqs. 2.7 and 2.8, except that k is now complex [56, 57]. The outgoing wave will now not only be phase shifted but will also be damped by an amount $\exp(-2\mathrm{Im}\delta_l)$. While this damping could be incorporated into the phase shift calculations, it is typically included as a term in the interatomic wave propagation. Atomic vibrations have a very similar effect, in that the overall diffracted beam intensity is reduced. This reduction is quantified through the Debye-Waller factor, $\exp(-2M)$, multiplying the intensities as $I = I_0 \exp(-2M)$, where

$$\exp(-2M) = \exp(-|\mathbf{Q}|^2 \langle (\Delta \mathbf{r})^2 \rangle). \tag{2.9}$$

In this equation $\langle (\Delta \mathbf{r})^2 \rangle$ is the average mean-square atomic deviation which may be anisotropic and $|\mathbf{Q}|^2$ is the 3D momentum transfer of the diffraction beam under consideration. Where the vibrations are assumed to be isotropic $\langle (\Delta \mathbf{r})^2 \rangle$ the Debye model of thermal vibrations can be used to give [56]

$$\langle (\Delta \mathbf{r})^2 \rangle = \frac{3\hbar^2 T}{m_a k_B \theta_D^2} \tag{2.10}$$

where m_a is the mass of the atomic species, T is the temperature in Kelvin at which the experiment was performed, θ_D is the Debye temperature of the crystal and other symbols have their usual meanings.

Codes used in this work

As previously discussed, there exist no direct method of transforming the diffraction data into a real space structure. Instead, solving the surface structure using LEED requires an iterative trial-and-error approach. In such an approach, theoretical LEED I-V curves for a trial structure are compared to the experimental LEED I-V curves and a reliability factor, or r-factor, calculated. This r-factor quantifies the agreement between the simulated and experimental data. On the basis of this r-factor, and any previous

trial structure r-factors, a new structure can be defined and simulated. This process continues until the agreement between the trial structure simulations and experimental data is deemed to be satisfactory.

This work has required the use of two different software packages in order to perform LEED I-V simulations. The first package, by Barbieri and van Hove [58], performed a relativistic calculation to obtain the scattering phase shifts. This package calculates for any structure the phase shifts for an electron of energy 0–300 eV for $l = 0$ to a user specified maximum. The following is a brief outline of the steps involved in the phase shift calculation.

The first stage is to generate a radial charge density for each of the N atoms in the structure for which phase shifts are required. This is a free-atom calculation done using the self-consistent, relativistic Dirac-Fock equation. The second stage is to compute the muffin-tin potential for the 3D bulk structure which is done using the method of Mattheiss [59]. In this step the atomic charge densities of the different elements comprising the structure which were calculated in stage one are superimposed and the muffin-tin zero, V_0, determined. The user specifies the size of the muffin-tin radii to use for the N elements in the 3D bulk. Small variations in the muffin-tin radii can lead to dramatic changes in the calculated phase shifts, which requires this stage to be an iterative one. In stage three, the phase shifts are determined from the muffin-tin potential calculated in stage two using the fully relativistic Dirac equation.

A number of previously calculated phase shift files are readily available [60]. To check for consistency, phase shifts for nickel were calculated using the Barbieri-Van Hove package and compared to those available. The results of this calculation are given in Fig. 2.7(a), where the solid lines are the phase shifts available from Van Hove and the dashed lines correspond to those calculated. Given the excellent agreement between the two, calculations for MnSb were performed in the same way as for nickel. The results for this calculation are also shown in Fig. 2.7, with panels (b) and (c) being the manganese and antimony phase shifts respectively. The phase shifts for manganese are very similar
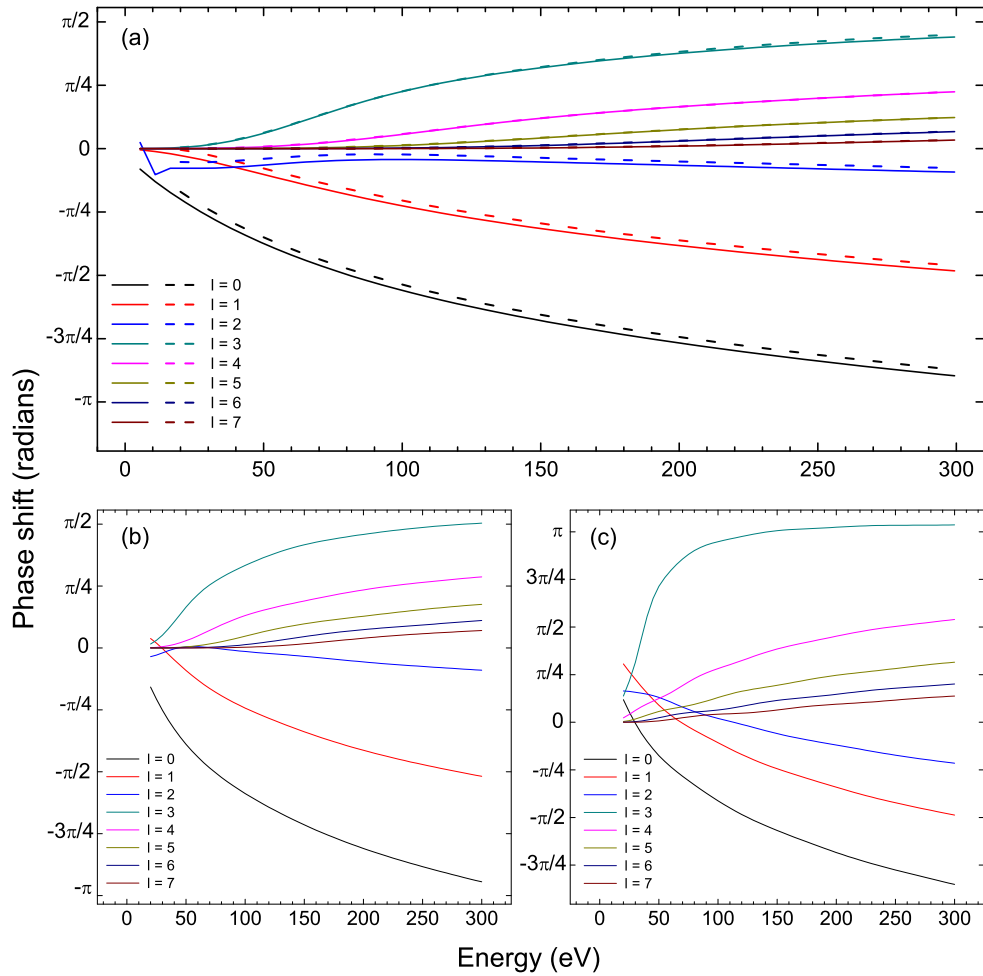
Figure 2.7: *(a) Calculated (dashed line) and reference (solid line) phase shifts for bulk-like nickel. (b) and (c) are calculated phase shifts for manganese and antimony in MnSb respectively.*

to those of nickel which is to be expected; nickel and manganese have similar atomic numbers so the atomic ion-core potentials should be similar. These phase shifts have been used throughout this work.

The LEED I-V software package used during this work is the Cambridge LEED, or CLEED package [61]. This package consists of three individual programs which are based in large part on the routines published by Van Hove and Tong [57]. The first of these is a LEED I-V calculation program, *cleed_nsym*, which takes as its input a trial structure and returns simulated I-V curves. A second program, *crfac*, calculates

the Pendry r-factor [62] between the simulated and experimental I-V curves. This r-factor takes a value between 0 and 1, where a value of 0 signifies perfect correlation between theoretical and experimental data and 1 signifies no correlation. Furthermore this r-factor is predominantly sensitive to the locations of peaks and troughs in the experimental and theoretical data and not on the absolute intensities of the peaks, except where peaks overlap when relative peak intensities are taken into consideration. When *crfac* calculates the r-factor, it rigidly shifts the calculated I-V curves within a ± 10 eV range. The reason for this is the real component of the muffin-tin potential increases the energy of the incident electrons by an amount equal to this quantity as it crosses the vacuum-surface interface but is rarely known *a priori*. To account for this value being chosen incorrectly, the *crfac* program rigidly shifts the calculated I-V curves within this narrow range in order to reach a minimum for that iteration. A third programme, *csearch* takes this r-factor, compares it to previous iterations and moves atoms in the trial structure to minimise the global r-factor.

To perform a full structure optimisation, CLEED requires three input files: a file specifying the bulk structure; an input file specifying the "overlayer" structure along with some computational variables for the *cleed_nsym* program and a control file which defines the relationship between the experimental and theoretical LEED I-V curves. Specifying the bulk and overlayer structures involves providing the co-ordinates of the atomic sites, the chemical species occupying each atomic site which is done through the phase shift files and vibrational coefficients which are calculated using Eq. 2.10. The atoms specified in the bulk file are never adjusted and remain as-supplied. The atomic positions in the overlayer file are assumed to be free parameters to be adjusted by *csearch* unless physical constraints are supplied. That is, unless stated otherwise *csearch* will assign one parameter for each x, y and z co-ordinate of every atom. However it is possible to specify which atoms are allowed to move, how they may move and if their motion is coupled to any other atom through symmetry.

In this work the geometrical optimisation performed by *csearch* was done using

a downhill gradient search. The Debye temperature of the bulk was assumed to be 300 K and the surface to be 250 K. The values for the real and imaginary parts of the muffin-tin potential have been set to -7 eV and 4 eV respectively. All of these values are approximations as the true values are not known but none are of particular importance in the LEED I-V calculations. As previously discussed V_{0i} is an effective damping term on the LEED spot intensity and lattice vibrations act to damp the diffracted beam intensity, but the Pendry r-factor is largely concerned with peak positions rather than absolute peak intensities. Moreover, in the simulations the energy scale of the simulated data for each iteration is rigidly shifted to minimise the r-factor. This accounts for a discrepancy in V_0.

2.2.3   Reflection high energy electron diffraction

Reflection high energy electron diffraction (RHEED) is essentially the same as LEED: electrons emitted from an electron gun are incident upon a sample and emerge as a series of diffracted beams which are observed on a phosphor-coated screen. In RHEED however, the electrons typically have an energy of between 10 and 20 keV and are incident upon the surface at a grazing angle of ∼1–3° as shown schematically in Fig. 2.8(a). The primary benefit of this experimental geometry is that electron diffraction can be performed at the same time as MBE growth as neither the phosphor screen or electron gun are in the path of the molecular beams (Fig. 2.1).

The diffraction pattern obtained in RHEED is slightly different from that in LEED. In a LEED experiment, the diffraction pattern obtained is simply a top-down projection onto the LEED optic of the intersection between the Ewald sphere and reciprocal lattice rods. In RHEED, the diffraction pattern is effectively the side-on projection of this intersection, as shown in Fig. 2.8. This means diffraction spots become diffraction streaks in RHEED and the observed pattern is a 1D projection of the 2D reciprocal lattice. In order to determine the full 2D reciprocal lattice, the sample must be rotated and the incident electron beam directed down various high symmetry directions.
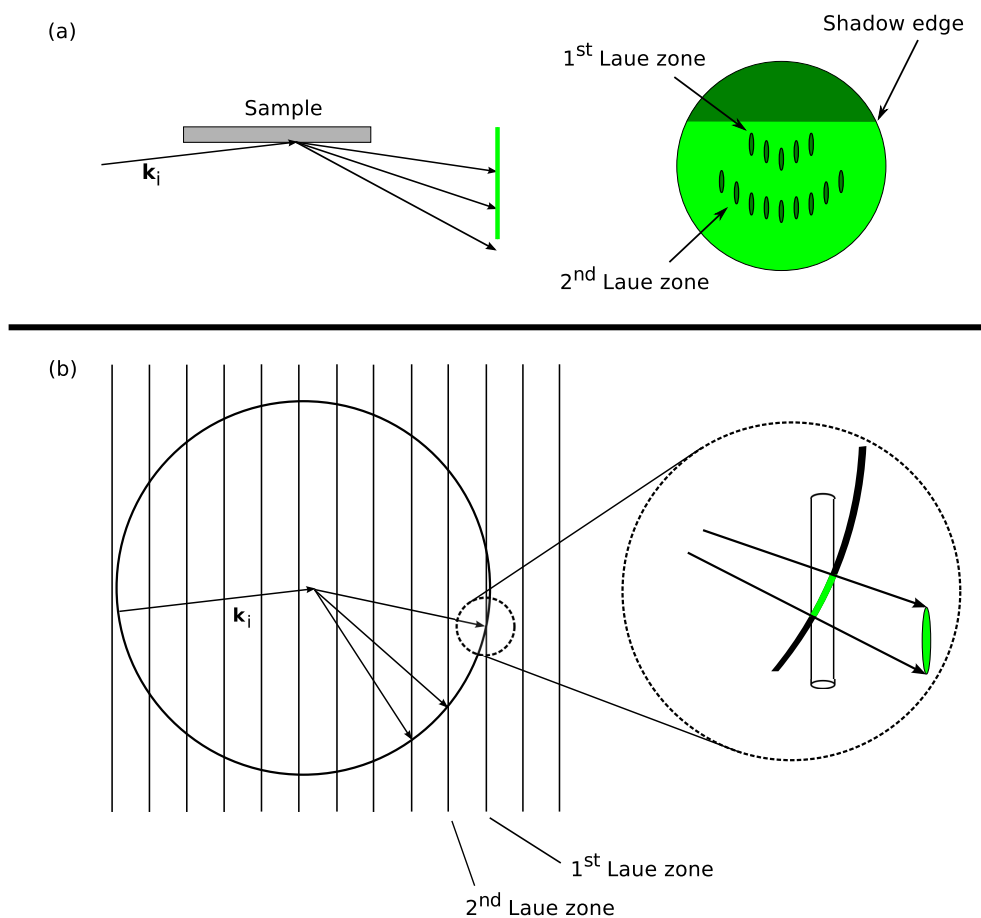
Figure 2.8: *A typical RHEED experiment showing (a) the incident geometry and what is observed on the phosphor screen and (b) how the characteristic RHEED streaks are formed by the intersection of the Ewald sphere with the reciprocal lattice rods.*

The length and width of the RHEED streaks depends upon the crystallinity of the surface, the energy distribution of the incident electrons and to a lesser extent the temperature at which the RHEED experiment is conducted. For a perfectly 2D crystalline surface at 0 K with a perfectly monochromatic electron beam, the reciprocal lattice rods become infinitely narrow and would lead to sharp, well defined diffraction spots on the RHEED screen [55]. Surface disorder, surface lattice vibrations and contamination all act to increase the width of the reciprocal lattice rods and hence the diffraction features elongate to give the streaks which characterise a RHEED pattern.

2.3 X-ray photoelectron spectroscopy

X-ray photoelectron spectroscopy allows the chemical composition of a material or thin film to be determined non-destructively. In this technique, a sample is illuminated with x-rays to excite electrons from bound states and eject them into the vacuum. Analysis of the energy spectrum of the emitted electrons enables the chemical identification of the surface. A more detailed and rigorous analysis of XPS spectra allows different bonding environments to be determined.

Core electrons in atoms and solids are localised into discrete energy levels subject to the quantum numbers n (principle quantum number), l (azimuthal orbital angular momentum) and m_l which defines the projection of l along a particular direction. In a given orbital, m_l can take any value between -l and +l and each m_l sublevel is capable of holding up to two electrons. These two m_l electrons are differentiated by their spin angular momentum, m_s and takes a value of $\pm\frac{1}{2}$. The total angular momentum, j, of an electron is thus defined as

$$j = l \pm \frac{1}{2}.$$

(2.11)

From this, the degeneracy (number of allowed states) is defined as $2j + 1$. For example, a d orbital contains 10 electrons: 6 in the 3d$_{5/2}$ and 4 in the 3d$_{3/2}$ sub-orbitals, where the subscript is the total angular momentum, j. An XPS spectrum from a d orbital will consist of two separate peaks with a peak area ratio of 3:2, separated by an amount equal to the spin-orbit interaction energy.

The energies of these discrete atomic levels can be calculated by solving the Schrödinger equation in the presence of the atomic potential. Since each atom has a unique atomic potential this leads to a unique set of discrete energy levels giving rise to a "spectral fingerprint". It is this which enables the unambiguous identification of atomic species in a given sample and the determination of its composition.

To generate an XPS spectrum, a monochromatic x-ray beam with a photon

energy of $h\nu$ incident upon a sample surface causes the photoemission of electrons from energy levels with a binding energy $E_b < h\nu$. A simple model suggests that the kinetic energy, E_k, of the photoelectron is simply the difference between the photon energy and electron binding energy

$$E_k = h\nu - E_b. \tag{2.12}$$

This is a statement of Koopman's theorem, but this is never observed. The photoexcited atom contains a core-hole and a net positive charge. This positive charge is "felt" by the other electrons in the excited atom which relax inwards to minimise their potential energy. Moreover, the conduction band electrons also experience an additional Coulombic potential which causes them to relax inwards in order to screen the potential. These two effects, known as intra- and inter-atomic relaxation processes respectively, whilst not being separable experimentally, provide the photoelectron with additional energy, leading to "chemical shifts". In principle, this allows the identification of different chemical environments of the same atomic species in the same sample.

Also of interest, is the observed lineshapes of a spectral feature. These are often described as being psudeo-Voigt functions, which are a convolution of Gaussian and Lorentzian lineshapes. The finite lifetime of the excited state contributes the Lorentzian component to the peak shape. This broadening is approximately constant for a given excited final state, that is, the lifetime broadening for Sb 3p spectral features is approximately constant for all chemically shifted components as the final excited state is the same, but is different for the Sb 4p spectral feature. Experimental factors such as a non-monochromatic x-ray beam and the intrinsic resolution of the detector contribute a Gaussian component to the spectral lineshape. This component is constant for a given x-ray source and spectrometer.

The peak area, A^p, for a given core level is given by

$$A^p \propto \int_0^\infty c^p(z) \exp\left(\frac{-z}{\lambda^p(E_k)\sin(\theta)}\right) dz \tag{2.13}$$

where $c^p(z)$ is the elemental concentration profile as a function of depth, z, $\lambda^p(E_k)$ is the inelastic mean free path (IMFP) of a photoelectron with an energy E_k and θ is the take-off angle (TOA) relative to the surface plane. In principle, it is possible to numerically model XPS data using this equation to determine the concentration profile $c^p(z)$ but this is inevitably time consuming and solutions are rarely unique. In some situations, however, it is possible to obtain trends by making the assumption $c^p(z)$ is constant so $A^p \propto \lambda^p(E_k)$ and the normalised intensity, I^p, can then be defined as

$$I^p = \frac{A^p}{a\lambda^p(E_k)D} \tag{2.14}$$

where a is the atomic sensitivity factor for the core level in question and D is the total dwell time per point in the scan region. The value of A^p is determined using peak fitting software after subtraction of an appropriate Shirely background [63]. This allows peak area ratios to be taken and the determination to a first approximation of the surface chemical composition.

Making the assumption that $c^p(z)$ is constant is not always applicable. In such situations, angle-dependent XPS experiments can yield information on the concentration profile. Moreover, two different core levels from the same element can be used to gain additional information on the concentration profile; the kinetic energies of the electrons in the two spectral features are different and so have different IMFPs and different effective probing depths.

All XPS data presented in this thesis were obtained at the National Centre for Electron Spectroscopy and Surface Analysis (NCESS), Daresbury Laboratory. The system comprises of a fast entry chamber, an XPS analysis chamber and a sample preparation chamber with an ion gun for Ar^+ sputtering and a heating stage. This XPS system uses a rotating aluminium anode source and a monochromater to select the Al K_α excitation ($h\nu = 1486.6eV$) with a maximum power rating of 8 kW and source FWHM of 0.26 eV. Photoelectrons are detected using a 300 mm hemispherical analyser

with a resolution of 0.3 eV. The overall energy resolution is thus 0.4 eV.

2.4 X-ray diffraction

X-ray diffraction is the coherent scattering of photons from the core electrons around atoms in a structure. The physical model proposed by Bragg says a diffraction peak occurs when the photon path length between any two scattering centres in a unit cell is an integer multiple of the photon wavelength. This amounts to the following mathematical relationship

$$2d_{hkl}\sin(\theta_B) = n\lambda \tag{2.15}$$

where d_{hkl} is the separation of atomic planes defined by the hkl Miller indices, θ_B is the angle between the crystal lattice planes and incident x-ray beam and λ is the x-ray wavelength. By analogy to diffraction from a grating, n is known as the "order" of diffraction, but the convention has developed where n is dropped from the equation in this context. A diffraction peak which would then correspond to the "second order" (111) reflection of a cubic lattice is in fact labelled as the (222) lattice plane with a plane spacing half that of the (111) spacing [64]. This convention is used throughout this thesis.

Whilst Eq. 2.15 is entirely correct, it is worth noting the dependency on λ which is not desirable, as two diffraction datasets obtained from the same material using separate photon energies will have Bragg peaks at different angles. However, it is possible to reformulate Bragg's law removing this dependency by considering the scattering vector, $\mathbf{Q}$, of the scattered photons graphically depicted in Fig. 2.9. Through geometry it can be shown that

$$\mathbf{Q} = \begin{pmatrix} Q_x \\ Q_y \\ Q_z \end{pmatrix} = \begin{pmatrix} \frac{4\pi}{\lambda}\sin\left(\frac{\omega}{2}\right)\sin\left(\theta - \frac{\omega}{2}\right) \\ 0 \\ \frac{4\pi}{\lambda}\sin\left(\frac{\omega}{2}\right)\cos\left(\theta - \frac{\omega}{2}\right) \end{pmatrix} \tag{2.16a}$$

where the magnitude of the photon wave vector, $|\mathbf{k}|$, has been replaced by $\frac{2\pi}{\lambda}$. For the
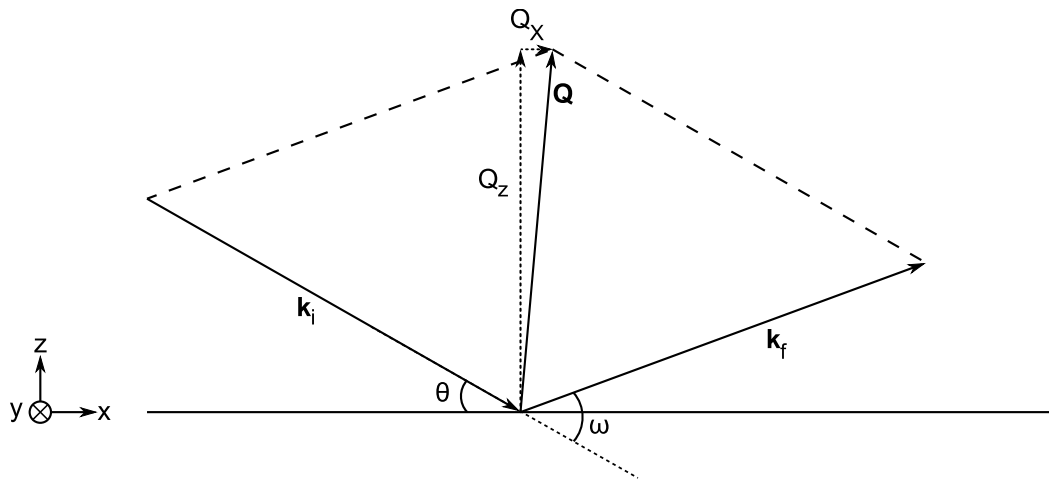
Figure 2.9: *Graphical representation of the scattering vector.*

case of symmetric diffraction, where $\omega = 2\theta$, the above simplifies to give

$$|\mathbf{Q}| = Q_z = \frac{4\pi}{\lambda} \sin\left(\frac{\omega}{2}\right). \tag{2.16b}$$

This can be substituted into Eq. 2.15 to yield

$$d = \frac{2\pi}{|Q_z|}. \tag{2.17}$$

This is a convenient form of Bragg's law as: a) all related lattice planes will be equally spaced in Q-space; and b) diffraction peak positions are independent of experimental conditions.

In this thesis, data from two different scattering experiments are presented. The first are symmetric Q_z scans and the second are "reciprocal space maps," which are 2D maps of scattered intensity obtained by "rocking" θ about a series of fixed detector positions. All of these data will be presented as scattered intensity against Q_x and Q_z.

Systematic Extinctions

A brief comment is needed on the observed systematic extinctions in x-ray diffraction patterns. The "structure factor" F_{hkl} expresses the total amplitude and phase of the scattered x-rays from the unit cell

$$F_{hkl} = \sum_1^n f_n e^{2\pi i(hu_n + kv_n + lw_n)} \tag{2.18}$$

where f_n is the atomic scattering factor and is proportional to atomic number, hkl are the Miller indices and (u_n, v_n, w_n) are the fractional co-ordinates of each atom in the n atom basis set. For example, the face centred cubic (fcc) lattice has an atomic basis of $(0, 0, 0)$, $(\frac{1}{2}, \frac{1}{2}, 0)$, $(\frac{1}{2}, 0, \frac{1}{2})$ and $(0, \frac{1}{2}, \frac{1}{2})$ and leads to the simple conclusion that if hkl is a mixed combination of odd and even numbers there is no reflection. Reflections only occur when hkl is an unmixed set of either odd or even numbers. As a second example, the hexagonal close packed structure has an atomic basis of $(0, 0, 0)$ and $(\frac{1}{3}, \frac{2}{3}, \frac{1}{2})$. This leads to a straightforward relationship: if l is odd and $h + 2k = 3m$ where m is an integer there is no reflection. A reflection will occur for all other combinations of hkl.

Graphical solution of Bragg's law

Indexing a diffraction pattern from an entirely unknown structure can be challenging, but, if the structure is cubic, a simple graphical solution to Bragg's law can be used to rapidly determine the lattice parameter. To do this it is necessary to calculate the lattice spacing d_{hkl} for arbitrary hkl. Vector analysis shows $1/d_{hkl}$ for a cubic structure to be [65]

$$\frac{1}{d^2} = \frac{h^2 + k^2 + l^2}{a^2} \ . \tag{2.19}$$

Substitution of this into Eq. 2.17 leads to

$$|Q_z|^2 = \frac{4\pi^2}{a^2}(h^2 + k^2 + l^2) \ . \tag{2.20}$$

If any or all of the unknown reflections in a diffraction pattern originate from a cubic structure then a straight line with gradient $\frac{4\pi^2}{a^2}$ can be plotted on a graph of Q_z^2 against $(h^2 + k^2 + l^2)$. Moreover, by applying this methodology in conjunction with Eq. 2.18 the type of cubic lattice, i.e. simple, fcc or bcc can also be determined.

This method can be extended to other structures but the process is invariably more complex. The lattice plane spacing in hexagonal lattices can be calculated for arbitrary (hkl), but there is the added complication of a non-orthogonal basis set and two different lattice parameters, a and c. For a hexagonal crystal

$$\frac{1}{d^2} = \frac{4}{3} \frac{(h^2 + hk + k^2)}{a^2} + \frac{l^2}{c^2} . \tag{2.21}$$

It is easily shown that when this is combined with Eq. 2.17, Q_z^2 is to be plotted against $\left(\frac{4}{3}(h^2 + hk + k^2) + \frac{l^2}{(c/a)^2} \right)$. For an unknown lattice the $\frac{c}{a}$ ratio is an unknown quantity but could be used as a free parameter in a fitting algorithm, if reflections corresponding to (00l) planes cannot be unambiguously determined. However, if the basal planes of the hexagonal lattice are expected to lie parallel to the surface then lattice planes with non-zero hk values will not be observed which greatly simplifies the analysis.

Scherrer Equation

An interesting but complicated topic is the effect of finite particle size on the FWHM of a diffraction peak. The Bragg equation states that a sample with a single value of d_{hkl} will result in a series of sharp peaks. However, this is only true of a perfect crystal of infinite size. As this can never be the case, all diffraction peaks are broadened by an amount inversely proportional to the thickness of the crystal.

Under the assumption of a parallel, monochromatic x-ray beam with diffraction peaks much broader than the resolution of the detector, the peak broadening in two-

theta, $\beta(2\theta)$, due to finite crystal size as derived by Scherrer is

$$\beta(2\theta) = \frac{K\lambda}{\tau\cos(\theta)} \ .$$ (2.22)

In this equation τ is the particle size, λ the x-ray wavelength, θ is the Bragg angle, K is a constant and $\beta(2\theta)$ is the full width at half maximum (FWHM) of the diffraction peak in radians. A number of methods can be employed to derive this equation and the value of the constant K. One method involves a simple manipulation of Bragg's law. Consider a crystal composed of m layers each separated by d and total thickness, $\tau = md$. Multiplying Eq. 2.15 by m and differentiating yields

$$\frac{\Delta\tau}{\Delta\theta_B} = -\frac{m\lambda\cos(\theta_B)}{2\sin^2(\theta_B)} \ .$$ (2.23)

Given that $\Delta\theta$ can be either positive or negative, that the FWHM in the scattered direction is $2\Delta\theta_B$ and that the smallest possible change $\Delta\tau$ is d, combined with Eq. 2.15, this can be re-expressed as

$$\beta(2\theta) = \frac{\lambda}{\tau\cos(\theta_B)}$$ (2.24)

This derivation arrives at a value of unity for K in Eq. 2.22. Another derivation given in Ref. [64] arrives at the same value, assuming a peak line shape which can be approximated to a triangle. Another approach is to use the full kinematic scattering equations and the assumption of Gaussian line shapes to arrive at $K = 0.94$ [65]. More sophisticated approaches use correlation functions or self-affine functions to Fourier transform between the real space object and the observed diffraction pattern. Using such methods the value of K can take any value between $\sim$0.6–1.1 [64, 65, 66]. In principle the value of K can be determined for a given crystal through detailed peak fitting, which includes fitting *exactly* the "tails" of the diffraction peak all the way to the background level; this is not always possible.

As a final comment, the derivation of the Scherrer equation assumes that finite

crystal size is the only contribution to the FHWM. In practice this requires a crystal without defects or strain dispersion and a diffraction experiment making use of a perfectly parallel beam of monochromatic x-rays and a detector with an infinitesimal acceptance angle. This is clearly never satisfied and results in a FWHM comprised of a sum of experimental resolution, a crystal strain distribution and finite size. Thus τ determined using Eq. 2.22 is a lower bound on the true value. Yet despite this obvious limitation the Scherrer equation can be used to determine semi-quantitative differences from different samples of the same material, provided the same experimental apparatus and peak fitting algorithm are used.

Williamson-Hall analysis

As noted above, a strain distribution within a crystal can lead to a broadening of the observed diffraction peaks. If a perfect crystal was subjected to a uniform stress, the lattice spacing would change from its equilibrium value d_0 to some new value d'. The overall effect of such a stress would be a shift in the diffraction peak without any other noticeable changes and allows the determination of *macrostresses*. However if the stress is either local, applied non-uniformly or non-uniform strain dispersion occurs within the crystal then a range of lattice spacings Δd centred around d_0 will diffract over a range $\Delta\theta$ centred about θ_B and contribute to the final FWHM of the diffraction peak. This contribution to the FWHM can be determined by differentiating Eq. 2.15

$$\Delta(2\theta) = \beta(2\theta) = 2\frac{\Delta d}{d}\tan(\theta) \tag{2.25}$$

where $\beta(2\theta)$ is again the contribution to the FWHM in 2θ. The ratio $\Delta d/d$ is simply the fractional change in the lattice spacing but includes both compressive and tensile strains about the mean lattice spacing. The maximum fractional change in lattice spacing is thus half $\Delta d/d$.

Importantly here $\beta(2\theta)$ is dependent upon θ. Reflections at larger values of 2θ

are therefore broader than those at lower values. By contrast, the Scherrer equation has no θ dependence. These two contributions to the FWHM can be separated and the dominant factor determined through Williamson-Hall analysis. Assuming the FWHM of the diffraction peak is dominated by contributions from finite particle size and strain dispersion Eqs. 2.22 and 2.25 can be combined to give

$$\beta \cos(\theta) = \frac{K\lambda}{\tau} + \eta \sin(\theta) \tag{2.26}$$

where $\eta = 2\Delta d/d$. Plotting $\beta \cos(\theta)$ as a function of $\sin(\theta)$ is known as a Williamson-Hall plot and should yield a straight line. The gradient of the line is simply related to the variation in the lattice spacing while the intercept yields information on the contribution to the FWHM from finite particle size.

2.5 X-ray magnetic circular dichroism

The technique of x-ray magnetic ciruclar dichroism (XMCD) is a relatively recent one, having been demonstrated in 1987 [67]. The basic physical principles of the theory behind XMCD can be illustrated using the following semi-classical model [68, 69, 70]. Assume an atom with an initial angular momentum of $\mathbf{J}$ in a quantum state defined as $|MJ\rangle$, with M being the projection of $\mathbf{J}$ along the direction of magnetisation, $M = \mathbf{J}\cdot\hat{\mathbf{m}}$. Suppose now this hypothetical atom absorbs a photon of angular momentum $\boldsymbol{\sigma} = \gamma\hat{\mathbf{k}}$, where γ is $+1$ (-1) for right (left) circularly polarised light and $\hat{\mathbf{k}}$ is a unit vector along the direction of propagation. Conservation of angular momentum dictates $\mathbf{J}' = \mathbf{J} + \boldsymbol{\sigma}$, so $M' = \mathbf{J}'\cdot\hat{\mathbf{m}}$ and $\Delta M = M' - M = \gamma(\hat{\mathbf{k}}\cdot\hat{\mathbf{m}})$. If the magnetisation direction is parallel or antiparallel to the direction of photon propagation, then $\Delta M = \pm 1$. For the simple magnetic atom in Fig. 2.10 this selection rule means only right circularly polarised light can be absorbed, so the atom demonstrates a huge circular dichroism.

For real magnetic materials the picture is qualitatively the same: core shell electrons are excited to vacant states above the Fermi level and, provided $\hat{\mathbf{k}} \cdot \hat{\mathbf{m}} \neq 0$,
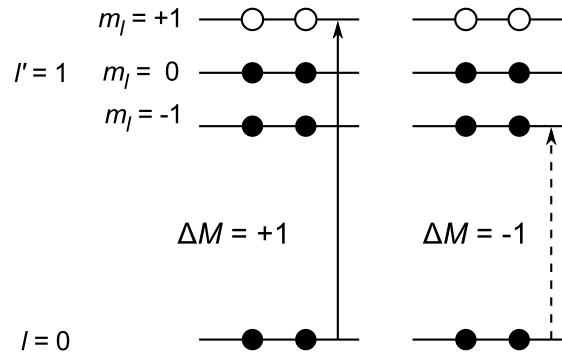
Figure 2.10: *Absorption of circularly polarised photons for the hypothetical atom described in the text.*

the material will demonstrate a degree of circular dichroism. For $3d$ transition elements it is the L edge, or $2p \to 3d$ transitions, which appear to show the largest dichroism, with dichroic signals of up to 25% seen at the L edge of iron and cobalt [71]. However, when spin-orbit coupling is introduced, this simple picture needs extending. Both left and right circularly polarised light can excite electrons from both the L_2 ($2p_{1/2} \to 3d$) and L_3 ($2p_{1/2} \to 3d$) edges [68, 72], with the transition probabilities given by Fermi's golden rule [69]. However, for some magnetic systems, it is possible to make use of the XMCD "sum rules" [73, 74]. These connect the absorption co-efficient of right and left circularly polarised photons, denoted as μ^+ and μ^-, to the groundstate spin and orbital expectation values respectively denoted as $\langle S_z \rangle$ and $\langle L_z \rangle$ through

$$\langle L_z \rangle = -\frac{\int_{L_3}(\mu^+ - \mu^-) + \int_{L_2}(\mu^+ - \mu^-)}{\int \mu} 2\langle N_h \rangle \tag{2.27a}$$

$$\langle S_z \rangle = \frac{\int_{L_3}(\mu^+ - \mu^-) - 2\int_{L_2}(\mu^+ - \mu^-)}{\int \mu} \frac{3}{2}\langle N_h \rangle - \frac{7}{2}\langle T_z \rangle \tag{2.27b}$$

where μ is the total, polarisation-independent x-ray absorption coefficient, $\langle N_h \rangle$ is the number of holes in the conduction band and $\langle T_z \rangle$ is the spin-quadrupole moment [75]. In these equations, the L_2 and L_3 subscripts on the integrals denote the specific edge to be integrated over. In order to use Eq. 2.27b, the $\langle T_z \rangle$ must either be experimentally determined or theoretically approximated, or assumed to be zero. Either way, it is

assumed that the L_3 and L_2 transition edges are sufficiently separated to enable the integrals in Eq. 2.27 to be calculated and that there is no "mixing" between the two edges. This is true for nickel and cobalt, but not true of elements such as manganese and chromium [75, 76].

There are a number of ways in which the dichroic signal can be measured. One method is to directly measure the x-ray absorption co-efficient as x-rays are passed through a magnetised sample. This does, however, rather limit the sample thickness when using soft x-rays ($\sim$600 eV) to access the $3d$ transition metal L edge. Alternatively, either a fluorescent x-ray signal or sample drain current can be measured. Both measure a de-excitation channel for an atom in an excited state, i.e. fluorescent x-ray or Auger electron emission. The rate of de-excitation is directly proportional to the rate at which excitations occur and thus provides a direct way of measuring the dichorism.

Both of these methods have some limitations and special considerations which must be noted. Firstly, the sample drain current is necessarily surface specific, as the current is proportional to the number of Auger electrons which are ejected from the sample surface. This is useful for surface science but this method provides no information beyond the near-surface region. The fluorescent signal will be less surface specific and far from a resonant absorption edge, these fluorescent x-rays can travel thousands of Ångstroms. However, in the soft x-ray regime, Auger emission is the stronger decay channel and above the L_3 absorption edge the fluorescent x-rays are resonantly self-absorbed, limiting their escape depth. Thus, in order to gain magnetic information on the bulk, x-ray resonant magnetic scattering (XRMS) is employed instead.

For a magnetic medium, the energy ($\hbar\omega$) dependent x-ray atomic scattering factor, f, may be written as [78]

$$f = f_0 + f'(\hbar\omega) + if''(\hbar\omega) + m'_\pm(\hbar\omega) + im''_\pm(\hbar\omega) \tag{2.28}$$

where f_0 is proportional to the atomic number, z, and $f'(\hbar\omega)$ and $if''(\hbar\omega)$ are re-
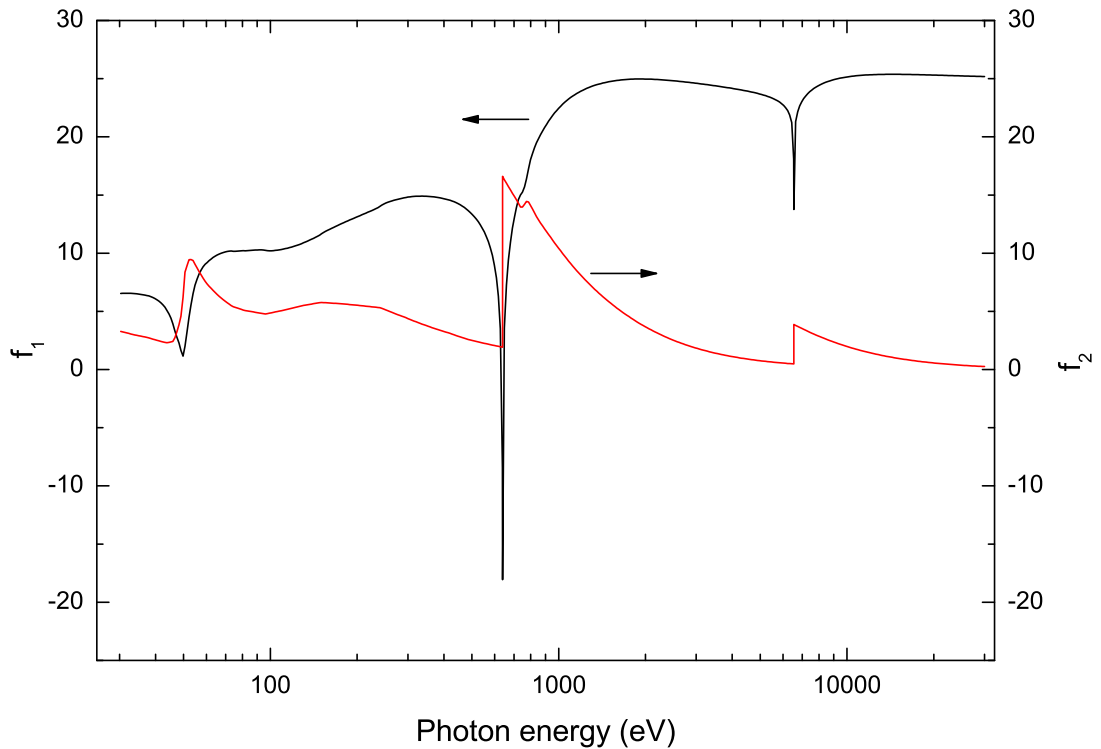
Figure 2.11: f' and f'' for manganese. The manganese L edge occurs at approximately 650 eV. The general forms of $m'_\pm$ and $m''_\pm$ are qualitatively the same. Taken from Ref. [77].

spectively the real and imaginary parts of the complex resonant anomalous scattering factor and are related to each other through the Kramers-Kronig transform. Fig. 2.11 shows example $f'(\hbar\omega)$ and $if''(\hbar\omega)$ data for manganese [77]. The strong absorption manganese L-edge is clearly apparent at approximately 640–650 eV.

In Eq. 2.28, $m'_\pm(\hbar\omega)$ and $m''_\pm(\hbar\omega)$ are the polarisation-dependent ($\pm$) real and imaginary components of the resonant magnetic scattering factor and are also related to each other through the Kramers-Kronig transform. The real components of f define the x-ray dispersion whilst the imaginary components relate to absorption of x-rays. As such, these two terms are of importance in XMCD. The $f''(\hbar\omega)$ term defines the total polarisation-independent x-ray absorption and allows x-ray absorption spectroscopy (XAS), whilst $m''_\pm(\hbar\omega)$ is the term responsible for the observation of XMCD. In the fluorescent and drain current XMCD experiments discussed above, it is only the pure mag-

netic absorptive part $(m''_\pm(\hbar\omega))$ which is measured. However, in XRMS, both $m'_\pm(\hbar\omega)$ and $m''_\pm(\hbar\omega)$ contribute to the experimental data as the incoming and outgoing x-rays set up standing waves within the sample. Depending on the location of the anti-nodes of the standing wave, the experimental data will either be dominated by dispersion (m') or absorption (m''), or contain some arbitrary mix between the two. Because of this, it is not possible to make use of the sum rules in Eq. 2.27 and detailed analysis of the the experimental data is particularly complex, with software packages enabling modelling of experimental data only recently being released.

To conclude, a brief comment is needed on the depth sensitivity of XRMS. With photon energies below the resonant absorption edge, photons penetrate up to hundreds of nanometres into the bulk. However, above the absorption edge, resonant absorption dramatically reduces the penetration depth to a few tens of nanometres.

2.6   Co-axial impact collision ion scattering spectroscopy

Ion scattering techniques have developed as a means of characterising the near-surface composition and for quantitative surface structure characterisation. Such techniques use a mono-energetic beam of noble gas ions incident upon the sample at an angle α with respect to the surface plane. The collisions which take place at the surface are well described by a simple free atom binary collision model as shown in Fig. 2.12. In such a model, an incident atom of mass M_1 is scattered through an angle of θ after striking an atom of mass M_2. By considering the conservation of energy and momentum of both atoms the initial and final energies of the incident ion, E_0 and E_1 respectively, is given by

$$\frac{E_1}{E_0} = \frac{1}{(1+A)^2} \left[\cos\theta_1 \pm \sqrt{A^2 - \sin^2\theta} \right]^2 \tag{2.29}$$

where A is M_1/M_2. This means incident ions elastically scattered from different masses will posses different kinetic energies and travel with different velocities. This provides the spectroscopic element to ion scattering techniques and allows for the determination
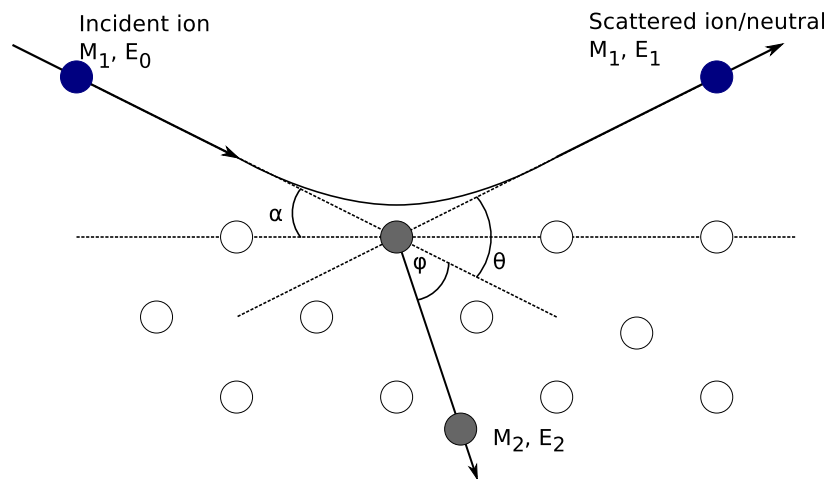
Figure 2.12: *Binary collision model used in ion scattering.*

of the atomic species in the near-surface region.

In co-axial impact collision ion scattering spectroscopy (CAICSS) only atoms which have been backscattered are detected. This means $\theta = 180°$ and leads to a great simplification of Eq. 2.29

$$\frac{E_1}{E_0} = \frac{(A-1)^2}{(A+1)^2}. \tag{2.30}$$

Of importance in CAICISS is the shadowing effect of surface atoms onto atoms in lower layers. As incident ions approach atoms in the surface, they "feel" a strong repulsive Coulombic force which gives rise to the backscattering, and is the CAICISS signal. However, most of the ions in the incident beam are forward scattered. This is shown graphically in Fig. 2.13. The impact parameter, p, defines the distance between the centre of the incident ion trajectory and the centre of the scattering atom. For p close to 0, the incident ion suffers large (almost $180°$) scattering. For larger values of p the incident ion is more weakly deflected from its original trajectory. This interaction creates a region behind the surface atom, the shadow cone, which is shadowed from the incident ion flux. However, one of the important observations from Fig. 2.13 is that the ion flux at the edges of the shadow cone is larger than the average incident beam flux. This effect is known as trajectory focussing. If the edge of the shadow cone happens
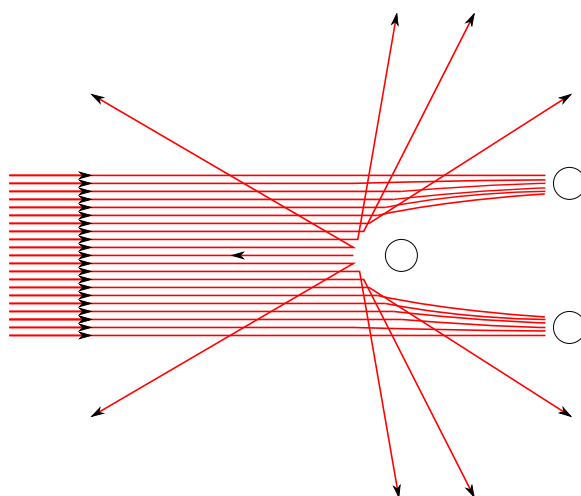
Figure 2.13: *Graphical depiction of the shadowing effect in ion scattering. The region behind a scattering atom is defined as the shadow cone within which the ion flux is zero. The ion flux is increased at the edges of the shadow cone relative to the incident flux, an effect known as trajectory focussing.*

to be incident upon a sub-surface atom, an increase in the backscattered intensity is observed.

Experimental data in CAICISS is acquired along the high symmetry crystallographic directions, which are aligned using the *in situ* LEED. A CAICISS spectrum is obtained by rotating the sample between 0–180° relative to the surface plane and detecting the ions and neutrals which are exactly backscattered. Structure dependent dips and peaks appear in the backscattered signal as a function of angle and correspond respectively to surface atoms blocking or trajectory focussing onto sub-surface atoms. Data analysis proceeds through a trial-and-error process, where a trial structure is simulated and the theoretical data compared against the experimental data. In this work, CAICISS data were analysed using a Monte Carlo approach implemented in the FAN software package. This package does not have an automated geometrical optimisation routine similar to *crfac* in the CLEED package. Consequently Pendry r-factors are not calculated for this technique and geometrical optimisation is performed manually.

2.7   Other techniques

2.7.1   Bulk magnetometry

Two techniques have been used in this project to characterise the bulk magnetic properties of the MnSb films. Vibrating sample magnetometry (VSM) is a technique which works by the principle of magnetic induction. A sample sits in a uniform magnetic field and is vibrated sinusoidally in close proximity to pickup coils. A small current is induced in nearby coils and is related to the time-dependency of the magnetic field through Faraday's law

$$\nabla \times \mathbf{E} = -\frac{\partial \mathbf{B}}{\partial t}. \tag{2.31}$$

The strength of the magnetic field, $\mathbf{B}$, in the vicinity of the pickup coils, changes with the sample magnetisation, $\mathbf{M}$, which in turn is controlled through a constant external magnetic field. Hysteresis loops are then taken by changing the external field and measuring the induced voltage in the pick-up coils.

The second bulk magnetometry technique is the superconducting quantum interference device (SQUID). In this method, a superconducting ring containing two Josephson junctions, one on either "branch" of the ring, is exposed to the magnetisation of the sample. Changes in the size and sign of the magnetisation of the sample results in a measurable change in the resistivity of the Josephson junctions.

In this thesis hysteresis loops of MnSb samples have been acquired using the VSM method whilst sample magnetisation as a function of temperature measurements were acquired using a SQUID.

2.7.2   Scanning electron microscopy

Whilst the ultimate aim of MBE growth is to produce atomically flat samples, imperfections in the target substrate, strain in the overlayer and incorrect growth conditions can

lead to defects and features which vary in size from a few Ångstroms to a few microns. Optical microscopy is limited in lateral resolution by the wavelength of light and cannot detect some of these morphological changes. However, electrons accelerated to an energy of several keV have sub-Ångstrom wavelengths and are therefore able to resolve features down to a few nanometers in size. This is the basis for electron microscopy techniques such as transmission electron microscopy and scanning electron microscopy. In the latter, electrons with typical energies of 1-20 keV are generated either through thermal emission from a hot filament or with a field emission gun and then accelerated and focussed onto the sample using electrodes and electromagnetic lenses. There are a number of contrast and imaging mechanisms that can be employed to probe different features and properties of the surface. All SEM data presented in this work were collected using secondary electron emission. In this mode of operation, the incident electron beam stimulates the emission of electrons from the sample through collisions and by the Auger emission of excited atoms. These secondary electrons emerge from the surface and are accelerated towards a detector through a positive potential. In secondary electron mode, surface topography is the dominant contributor to the image contrast.

Chapter 3

Growth and characterisation of NiSb(0001)

To date, little exists in the literature on the growth of NiSb thin films. Single crystal bulk samples grown by the Bridgman method have confirmed through XRD the crystal structure to be that of NiAs [79]. Studies on polycrystalline samples have shown NiSb to exhibit Pauli-type paramagnetism [17], in agreement with theoretical DFT calculations employing the APW method within the local density approximation [80]. More recently, a DFT study motivated by experimental evidence for the existence of zincblende CrSb [81] has recently been concluded. A summary of these calculations is given in Appendix A.

As discussed in Chap. 1, it is easy to envisage spintronic devices being constructed out of CrSb, NiSb and MnSb given their different magnetic behaviours. However, to date no thin film growth of NiSb on any substrate using any method has been reported in the literature. A number of questions thus remain unanswered, including but not limited to:

- What is the growth orientation of NiSb on III-V (111) substrates?

- What is the growth mode of NiSb(0001) on III-V substrates, e.g. 3D island growth or layer-by-layer growth?

- Can high quality, single crystal NiSb thin films be grown on III-V substrates?

This chapter details the preliminary work undertaken in attempting to answer these questions. In Section 3.1 the MBE procedure to grow NiSb thin films is discussed alongside RHEED images demonstrating reconstruction of Ni- and Sb- rich surfaces.

Preliminary XPS results are presented in Sec. 3.2 and the results of a high resolution XRD study elucidating on the crystal structure of these films is presented in Sec. 3.3.

3.1 Growth of NiSb on GaAs(111)B

Several NiSb thin films have been grown on GaAs(111)B substrates, (10×10) mm in size. The substrates were attached to stainless steel sample plates using a combination of In-Ga-Sn eutectic and indium solder. Once mounted the samples were degreased using acetone and isopropanol before being blown dry with dry nitrogen. Samples were then loaded into a sample preparation chamber via a loadlock. Once under vacuum, substrates were prepared through a 1 hour degas at 420 °C, a 10 minute ion bombard with 500 eV Ar$^+$ at grazing incidence and a 40 minute anneal at 480 °C. The typical RHEED pattern following this procedure was a td(1×3) and is shown in Fig. 3.2.

This section details the growth conditions and the surface reconstructions of three films. The key differences between the three samples are as follows. Sample *A* was grown for 1 hour using a beam flux ratio, J of 6.6 and a Ni BEP of 4.8×10^{-8} mbar. Sample *B* was grown for 25 minutes with $J = 7.0$ and Ni BEP of 1.4×10^{-7} mbar. sample *C* used the same Ni BEP as *B* but J set at 7.4, with a growth time of 10 minutes. All samples were grown using a single stage growth with the substrate held at 420 ± 5 °C throughout. None of the samples were Sb capped after growth. An SEM micrograph of sample *A* is shown in Fig. 3.1. The morphology of this sample is very similar to the mesa morphology seen on MnSb which is discussed in some detail in Chap. 4.

From RHEED observations the initial stages of growth for the three samples are characterised by a rapid loss of fractional order streaks and a weakening of the integer order streak intensity. For samples *A* and *B*, some modulation of the streak intensity and the appearance of some transmission diffraction spots were apparent, with the intensity of these features stronger in sample *A*. These features indicate the existence of
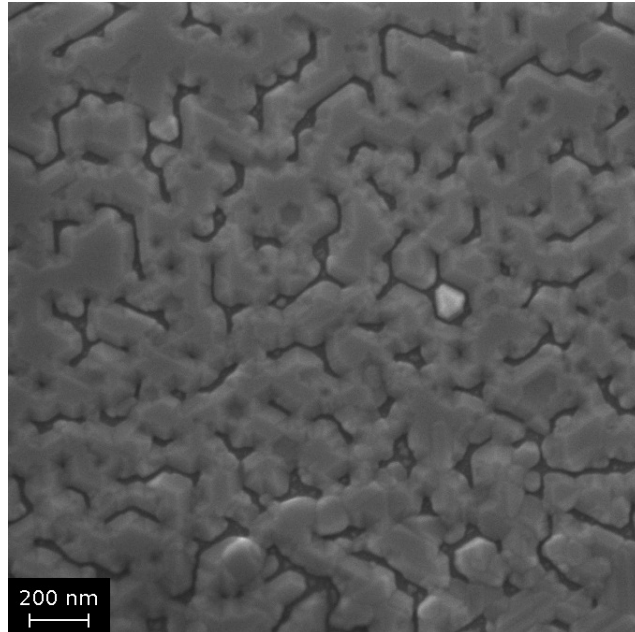
Figure 3.1: *An SEM micrograph of sample* A. *The morphology is very similar to that of MnSb as shown in Fig. 4.1, with flat topped interconnected mesas separated by trenches the height of the film and several nanometres wide.*

a roughened surface with 3D islands. For sample *B* these additional features disappeared after 1 minute to give strong and sharp integer order streaks. For sample *A* the lower beam pressures meant the time for these additional features to disappear was much longer at approximately 5 minutes. Neither transmission diffraction spots nor streak modulation were apparent on sample *C*, with the only changes being a loss of GaAs fractional order streaks and an initial reduction in integer streak intensity. From these RHEED observations it is suggested that NiSb under these conditions grows in a similar manner to MnSb, namely the formation and eventual coalescence of 3D islands [82]. Furthermore, from these RHEED patterns the growth orientation has been determined as NiSb[0001]∥GaAs[111] and NiSb[$2\bar{1}\bar{1}0$]∥GaAs[$\bar{1}10$]. This is as expected and in direct agreement with the thin film growth of other binary pnictides [82, 83, 84].

Once growth was terminated, the samples were exposed to separate beams of antimony and nickel whilst held at the growth temperature. Each sample demonstrated slightly different behaviour under these conditions. Sample *A* showed no appreciable
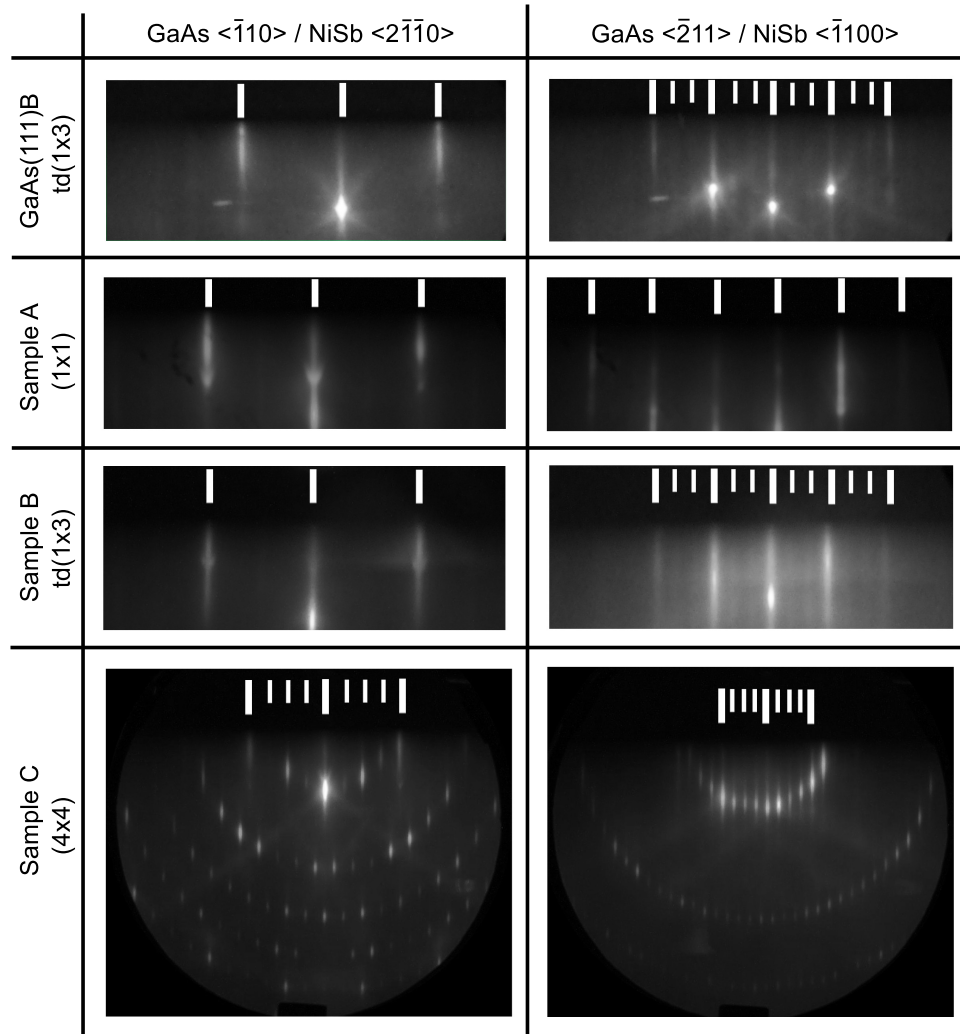
Figure 3.2: *RHEED images taken from a typical GaAs(111)B substrate prior to growth and from all three NiSb films after growth. The white bars are guides to the eye: the longer bars correspond to integer order streaks whilst the shorter bars correspond to fractional order streaks.*

change in the RHEED pattern aside from a marginal decrease in the streak intensity, even after exposure to nickel and antimony beams lasting tens of seconds. This is surprising but may be due to a combination of surface roughness and low BEPs. Sample *B* under nickel exposure changed from a (1×1) to a (6×4) reconstruction. This reconstruction was only metastable and did not last long enough after nickel exposure for photographs to be taken. Under exposure to antimony a td(1×3) pattern was observed, which is similar in behaviour to MnSb [82] and MnAs [85]. In analogy to these

other binary pnictides it is suggested this surface reconstruction originates from chains of antimony on the surface. Finally sample C produced a very sharp and clear surface reconstruction with $(4\times)$ periodicity in all of the high symmetry crystallographic directions with multiple and intense Laue zones. This reconstruction was again unstable at the growth temperature but at room temperature, this surface reconstruction was observed to be stable over several hours. Fig. 3.2 shows RHEED images from a typical GaAs(111)B-td(1×3) substrate and all of the NiSb surface reconstructions which could be photographed.

There are, however, a very limited number of studies in the literature on (4×4) surface reconstructions of hexagonal surfaces. Examples include the surface reconstruction of Ga-polar GaN(0001) [87] and the germanium-induced reconstruction on SiC [88]. Both reconstructions are expected to be III-V-like so their applicability to NiSb is unclear. Examples of (4×4) reconstructions on metals include the sub monolayer coverage of tin and lead on Rh(111) [89], however this reconstruction is thought to arise due only to the Pb–Pb bond length being 4/3 that of the Rh–Rh.

The picture is made more complicated by the fact a number of different surface nets may yield the same observed diffraction pattern. Two inequivalent (2×2) sub units may be arranged in such a way as to generate a (4×4). In addition, there are two other possible surface structures, depicted in Fig. 3.3, which result in the same RHEED pattern: a triple domain (2×4) and a triple domain centred (4×4). Consequently, it is not possible on the basis of RHEED observations alone to conclude either what the surface structure or reconstruction actually is. Atomic resolution scanning tunnelling microscopy images should be able provide some indication given the three surface nets are very different in both size and shape.
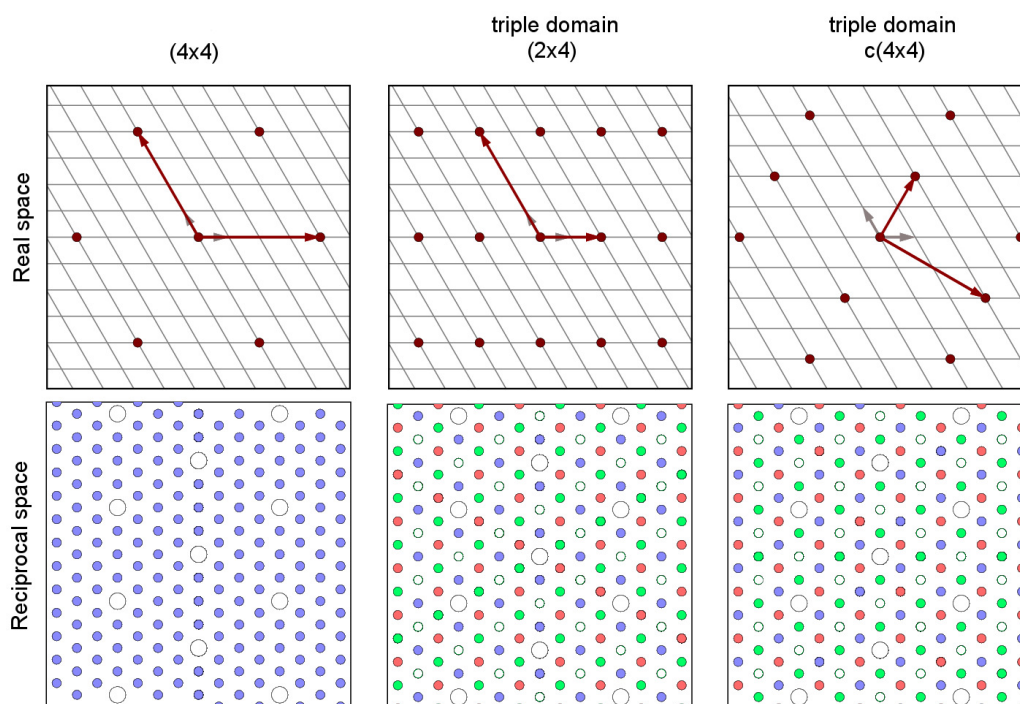
Figure 3.3: *Representations of the possible surface structures giving rise to the observed NiSb reconstruction. In the top three panels, the (1×1) surface mesh is drawn in grey with surface lattice vectors in red. The large open (small closed) circles in the reciprocal space representations are integer (fractional) order spots. The three different colours relate to the three different domains with small white open circles being common to all three domains. The figure was made with the assistance of LEEDpat [86].*

3.2 X-ray photoelectron spectroscopy

A preliminary XPS study has been carried out on sample *A* at 90° TOA. The sample was neither chemically etched *ex situ* nor subjected to ion bombarding and annealing procedures *in situ* and scanned entirely "as-loaded." Scans were taken of the Ni 2p, Sb 3d and O 1s, Sb 4d, C 1s, Ga 2p, Ga 3d and As 3d regions, as well as a "survey" scan from 0–1360 eV. Fig. 3.4 shows the survey scan, Ni $2p_{3/2}$ and As 3d, Sb 4d and Ga 3d regions. After subtraction of a Shirley background, elemental peak areas were found for nickel, antimony, carbon and oxygen. These results are tabulated in Tab. 3.1.

The first thing of note from these data is that the surface is dominated by oxygen and carbon contamination. This is to be expected for an air-exposed sample which has
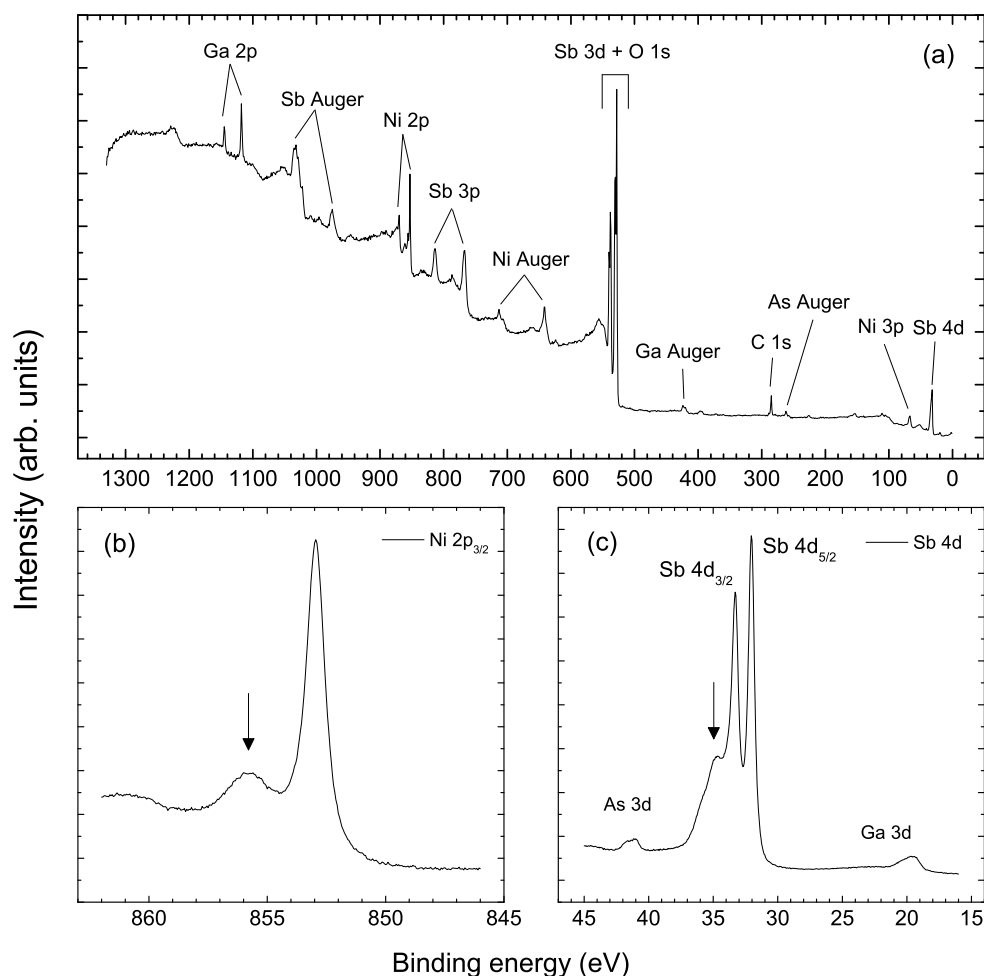
Figure 3.4: *XPS data for sample* A *as-loaded. (a) Survey scan with the main spectral features labelled. (b) Ni $2p_{3/2}$ region. (c) Sb 4d region. The arrows in (b) and (c) indicate respectively Ni-oxide and Sb-oxide features. Both of these features are considerably less intense than those observed on air-contaminated MnSb [90]*

not been subject to any cleaning treatments. Interestingly, the nickel and antinomy regions shown in Fig. 3.4(b) and (c) are not dominated by Ni- and Sb-oxides. Oxide contamination is a particularly difficult problem with air-exposed MnSb, as up to 5 nm of Mn-oxides form, with these oxides being resistant to *in situ* IBA treatments [90]. The second thing to note is the antimony-to-nickel peak area ratio is almost exactly two. However, peak fitting shows the Ni-O $2p_{3/2}$ peak area is $\sim$7 times smaller than the Sb-O 4d peak area. Thus it is suggested that the reason for the high Sb:Ni ratio

Table 3.1: *Normalised counts per second (CPS) of the main peak regions and the atomic percentage composition. As expected, the surface stoichiometry is dominated by carbon and oxygen.*

Core level	Normalised CPS	Percentage
O 1s	9,394	59.0
C 1s	3,555	22.3
Sb 3d$_{5/2}$	1,982	12.5
Ni 2p$_{3/2}$	988	6.2

is due to an oxidised antimony-rich surface. Finally, gallium and arsenic features are observed. These features are likely to arise due to the mesa morphology shown in Figure 3.1. However gallium segregation in MnSb thin films has been observed [91] and this remains a possibility in NiSb without further experimental evidence.

3.3 X-ray diffraction studies of NiSb films

The three samples discussed in the previous section were studied using hard x-ray diffraction. Scattering data along the surface normal for sample *A* was acquired using an in-house Philips X'Pert PANalytical diffractometer. Scattering data for samples *B* and *C* at 50 K and 300 K were acquired using beamline X22C at the National Synchrotron Light Source, Brookhaven National Laboratory.

These XRD data are presented in Fig. 3.5. The most intense reflections are easily indexed to (111) and (0001) planes of GaAs and NiSb respectively. From these data, the lattice parameter of the GaAs substrate for samples *B* and *C* was calculated using a least squares minimisation on the eight GaAs reflections, and assumed separate 2θ detector offsets for the two samples. The value of a_{GaAs} at 300 K for samples *B* and *C* has been calculated as 5.654(6) Å and 5.653(6) Å respectively. The accepted value of 5.6533 Å [92] falls within the margin of error of both values. Furthermore, by combining the 50 K and 300 K data values, the linear expansion coefficient, α, for
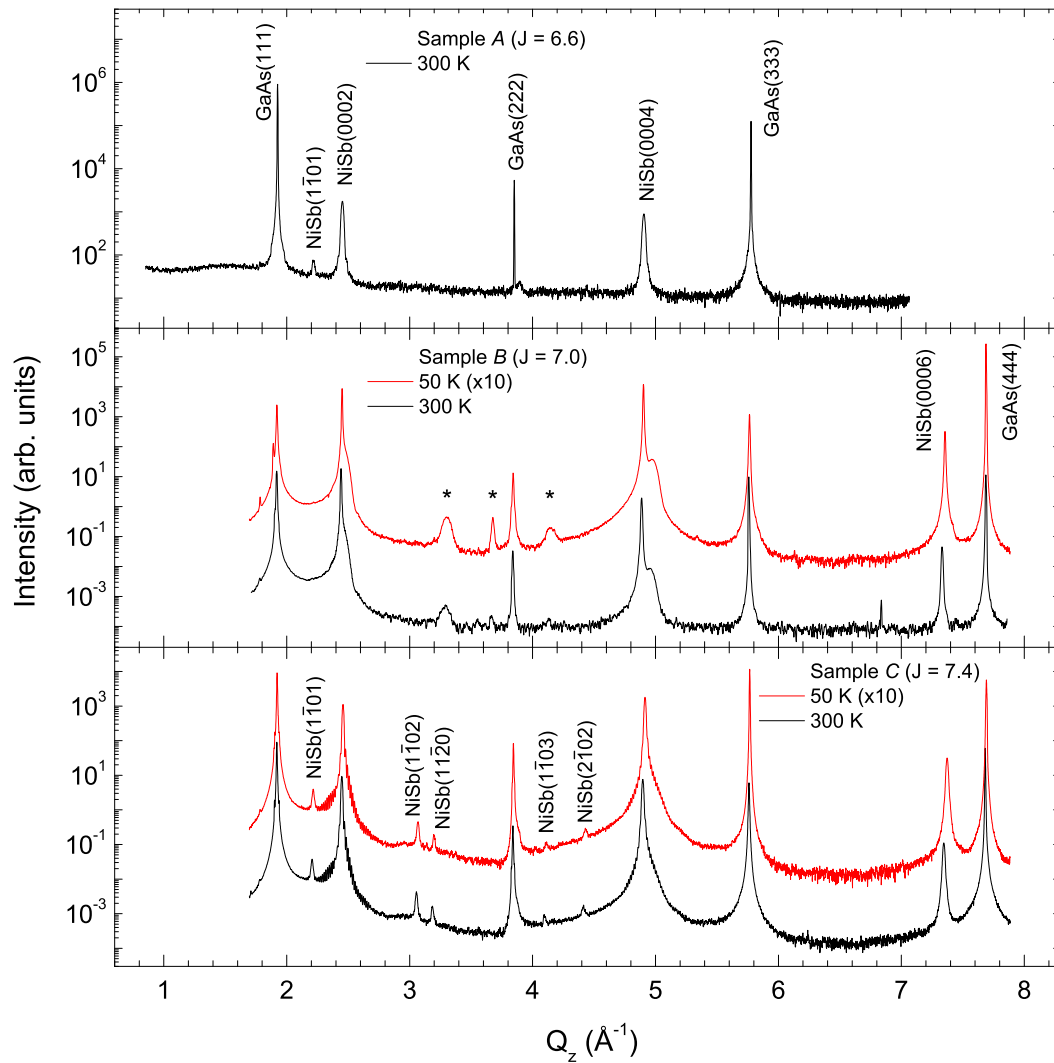
Figure 3.5: *Hard x-ray θ–2θ scattering of the NiSb films. Sample* A *data were acquired in-house whilst samples* B *and* C *were acquired at the NSLS at 50 K and 300 K. (0001) and (111) reflections from the NiSb epilayer and GaAs substrate are labelled accordingly. Peaks marked with an asterisk remain unindexed.*

samples *B* and *C* have been calculated as $5.6(1) \times 10^{-6}~K^{-1}$ and $5.2(1) \times 10^{-6}~K^{-1}$ respectively. Whilst these values are in broad agreement with a published value at 300 K of $5.87 \times 10^{-6}~K^{-1}$ [92] it must be noted that the temperature control of the sample leads to an inherent uncertainty of ± 5 K and α for GaAs changes sign at $\sim$50 K [92].

The c lattice parameter and α for NiSb can be calculated from these data using the same 2θ offsets determined when calculating a_{GaAs}. For sample *B* these

Table 3.2: *A summary of the reference and experimental lattice parameters at 50 K and 300 K. Values for the thermal expansion co-efficient, α are given for samples* B *and* C. *The large error in α is due to the uncertainty associated with the sample temperature.*

		Lattice parameter (Å)		α
		50 K	300 K	
GaAs	Reference [92]	5.645	5.653	5.87×10^{-6}
	$J = 6.6$	N/A	5.648(5)	N/A
	$J = 7.0$	5.646(6)	5.654(6)	$5.6(5) \times 10^{-6}$
	$J = 7.4$	5.646(6)	5.653(6)	$5.2(5) \times 10^{-6}$
NiSb	Reference [79]	N/A	5.141	Unknown
	$J = 6.6$	N/A	5.125(5)	N/A
	$J = 7.0$	5.116(5)	5.132(5)	$1.1(1) \times 10^{-5}$
	$J = 7.4$	5.099(5)	5.119(5)	$1.6(2) \times 10^{-5}$

are 5.132(1) Å and $1.1(1) \times 10^{-5}$ respectively and for sample *C* are 5.119(1) Å and $1.6(1) \times 10^{-5}$ respectively. A previous publication by Ogarev and co-workers reported the c lattice parameter of bulk grown NiSb to be 5.141 Å [79], which lies outside the margins of error in this experiment.

The GaAs lattice parameter for sample *A* was also calculated using a least squares method on the three accessible reflections assuming a 2θ offset, but was calculated separately from samples *B* and *C*. The lattice parameters derived from these data for GaAs and NiSb are 5.648(5) and 5.125(6) Å respectively. Owing to the lack of any cooling stage on the X'Pert diffractometer, data could not be acquired at 50 K and the thermal expansion coefficient could not be derived. As with samples *B* and *C*, the GaAs lattice parameter agrees within experimental error with accepted values whilst the lattice parameter disagrees with the value reported by Ogarev and co-workers.

In addition to these strong GaAs and NiSb reflections, a number of unidentified peaks are also apparent. Firstly, the additional reflections in sample *C* could originate from misoriented NiSb crystallites. Tab. 3.3 contains a summary of the peak positions, the indexing of these peaks and their associated theoretical positions based upon lattice parameters of $a = 3.953$ Å and $c = 5.119$ Å. The reciprocal space map presented in Fig. 3.6 supports this hypothesis; the reflection at 2.2 Å^{-1} in Q_z is very broad in Q_x

Table 3.3: *Summary of the additional reflections in sample* C *with the assigned NiSb plane. Predicted peak positions have been calculated using* $a = 3.953$ Å *and* c $=$ *5.119 Å.*

Lattice plane	Predicted Q_z (Å^{-1})	Experimental Q_z (Å^{-1})
($1\bar{1}01$)	2.208	2.2(1)
($1\bar{1}02$)	3.065	3.06(1)
($11\bar{2}0$)	3.179	3.19(1)
($1\bar{1}03$)	4.114	4.09(1)
($2\bar{1}02$)	4.416	4.41(1)
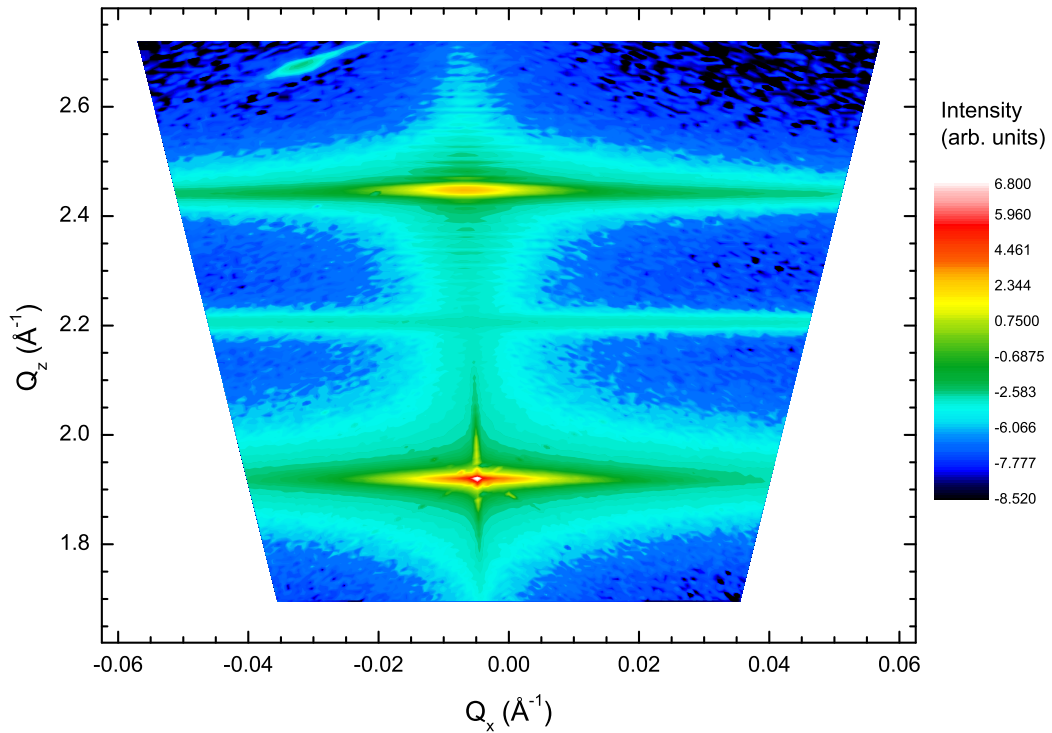
Figure 3.6: *Reciprocal space map of sample* C *in the vicinity of the NiSb(0002) reflection. The reflections at* $Q_z = 2.45$ Å^{-1} *and 1.9 Å^{-1} correspond to GaAs(111) and NiSb(0002) respectively. The additional feature in the top left of the figure is due to multiple scattering.*

and has an appearance similar to a powder diffraction ring.

The unidentified reflections in sample *B* are more complicated to interpret. The shoulders which appear on the NiSb (0002) and (0004) reflections may originate from
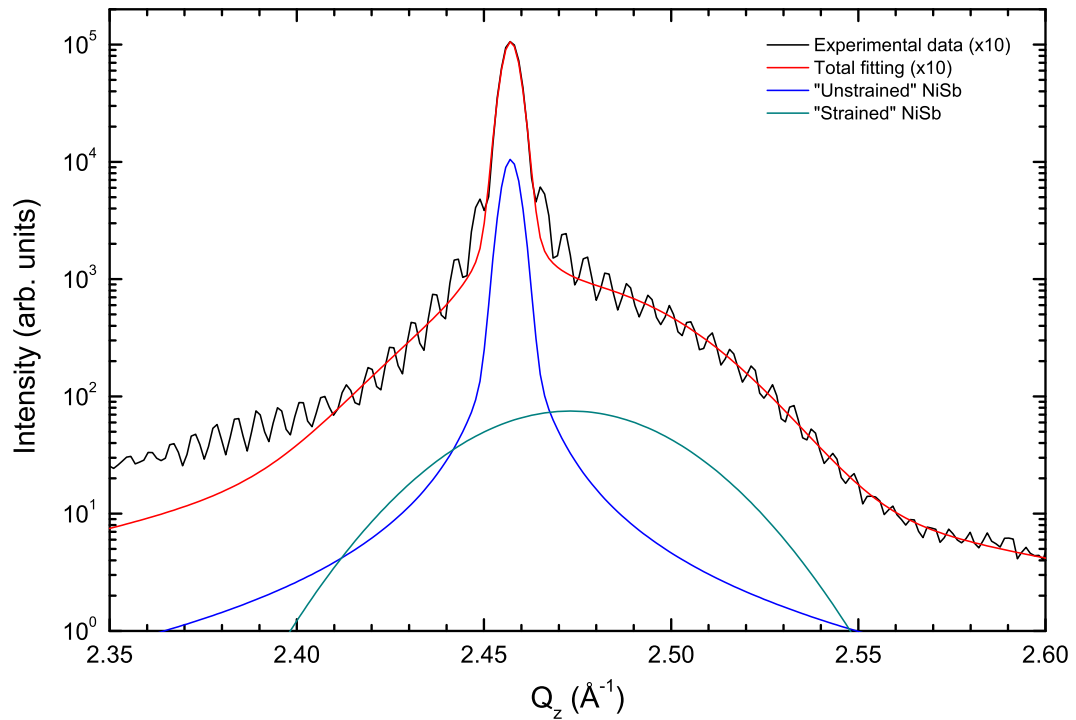
Figure 3.7: *Peak fitting for the NiSb (0002) reflection at 300 K in sample* B. *Two pseudo-Voigt functions (blue and green lines) were fitted to the experimental data (black line).*

strained NiSb in the vicinity of the NiSb/GaAs interface under an approximately volume-conserving distortion. Under this assumption, the volume of the unit cell will remain close to its bulk value of 69.57 Å^3 whilst the in-plane lattice parameter expands to match that of GaAs, namely 3.9975 Å. To test this hypothesis the NiSb (0002) and (0004) reflections were fitted using two pseudo-Voigt functions. The final fits are shown in Figures 3.7 and 3.8. The key parameters in this analysis are the position of the two peaks, labelled for convenience as "unstrained" and "strained" NiSb, and their associated FWHM. These values are given in Tab. 3.4. The positions of the "strained" NiSb peak give c lattice parameters of 5.10(1) and 5.05(1) Å. Under the assumption that a_{NiSb} has increased to match that of GaAs, the cell volume as given by these two c parameters are 70.5(1) and 69.9(1) Å^3 respectively, which is in reasonable agreement with the unstrained cell volume.
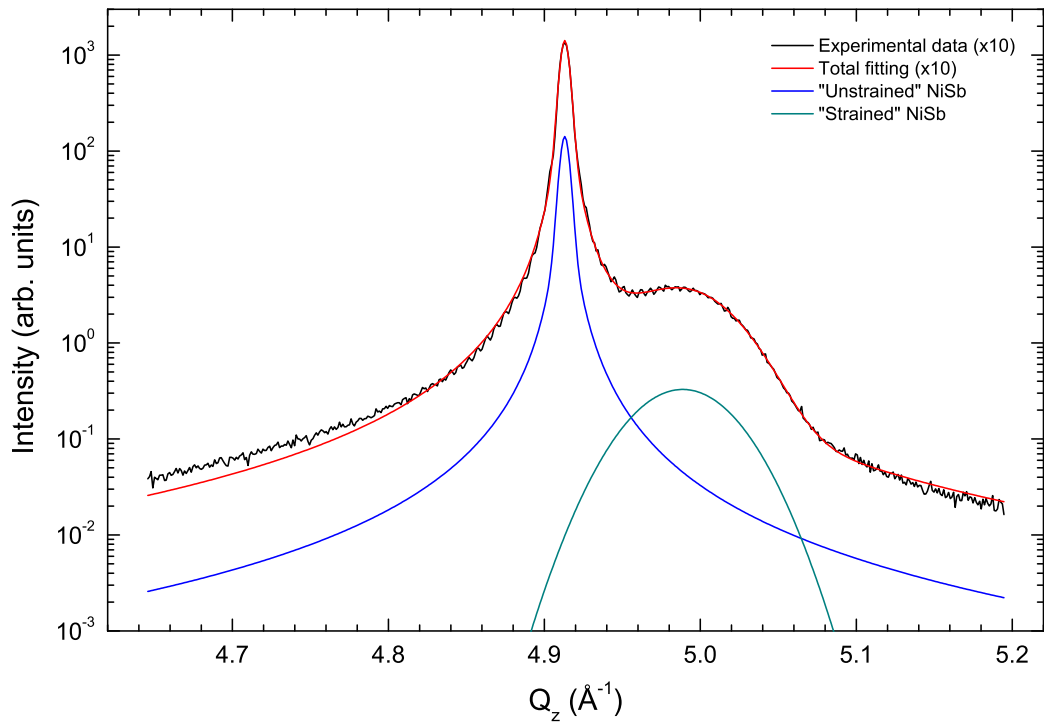
Figure 3.8: *Peak fitting for the NiSb (0004) reflection at 300 K in sample B. Two pseudo-Voigt functions (blue and green lines) were fitted to the experimental data (black line).*

Table 3.4: *Fitting details of the NiSb (0002) and (0004) reflections. The c lattice parameter is calculated from the peak position whilst the grain size is calculated using the FWHM in the Scherrer equation with $K = 0.9$.*

Reflection	Position (Å^{-1})	FWHM (Å^{-1})	c (Å)	Grain size (Å)
0002	2.47	0.11	5.10	108.1
0004	4.97	0.13	5.05	97.2

However there are three reasons as to why a strained NiSb layer may not be the source of these shoulder peaks. Firstly it is reasonable to assume that any such strained layer would be a property of the interface, which is NiSb/GaAs(111)B in this case. Given that the principal difference between the three samples is the beam flux ratio, it is expected that any strained layer induced by the epitaxial growth would be common to all three samples. This does not appear to be the case.

Secondly, the FWHM as determined from the peak fitting can be used in the Scherrer equation (Eq. 2.22) to estimate the size of the grains (or thickness of the layer) giving rise to the anomalous reflections. Taking the constant, K, in the Scherrer equation to be 0.9, the grain size is estimated to be 108 Å and 97 Å as deduced from the (0002) and (0004) reflections respectively. A more precise estimate of the size of the "strained" layer can be obtained using the thickness fringes evident in Fig. 3.7. There are two frequencies to the thickness fringes: one with a frequency of 0.007 Å^{-1} and a beat frequency of 0.058 Å^{-1}. The beat frequency is taken to originate from the "strained" layer and provides an estimate of the layer thickness of 108 Å. This is in remarkably good agreement with the values derived using the Scherrer equation, leading to the conclusion that the "strained" grains are in fact $\sim$100 Å in size. This is surprisingly large. Hypothetically it is possible for a strained layer of this thickness to exist if the bulk modulus of the material is small. However, this quantity is not known, making it difficult to ascertain on a purely energetic basis if this is plausible.

Thirdly, the FWHM between the two peaks is of a comparable size. From Williamson-Hall analysis described in Sec. 2.4 the FWHM of peaks from related planes will increase proportionally to $\tan(\theta)$ if there is strain dispersion within the material. The FWHM of the shoulder peak fits are approximately the same, suggesting strain dispersion is not the dominant factor contributing to the FWHM. Consequently, there should be a third "shoulder" peak at approximately 7.5 Å^{-1} which isn't the case. Given these three problems it seems unlikely that a strained NiSb layer can account for these shoulders. However, without further evidence to the contrary it cannot be definitively ruled out.

Of the other unidentified reflections theoretical peak positions based upon the cubic lattice parameter determined through DFT were compared against the experimental data. The details of the calculations are given in Appx. A with the expected peak positions given in Tab. A.2. From these positions it is clear that zinc-blende NiSb cannot be the cause of any of the additional reflections.

It is seen in XPS data that some oxidation has occurred at the surface, and whilst the level of oxidation in these films is smaller than that observed with MnSb, a small Ni-oxide feature is clear in the presented XPS data. It is possible that, given a thick enough oxide layer, reflections originating from NiO would be seen. However, none of the calculated peak positions for NiO given in Appx. A correlate with those in the experimental data.

A graphical representation of Bragg's law, as prescribed in Sec. 2.4, was used in an attempt to fit all or some of the reflections to a cubic lattice, or a hexagonal lattice with basal planes parallel to those in the n-NiSb film. However, none of the additional reflections can be adequately indexed onto either face or body centred cubic lattices or (000l) reflections from a hexagonal lattice. The reflections at $Q_z = 3.3$ Å^{-1} and 3.65 Å^{-1} can in principle be indexed to a primitive cubic structure with a lattice parameter of 4.43 Å but this identification is extremely unlikely as no compound containing any combination of Ga, As, Sb or Mn forms a *primitive* cubic structure.

A number of other possibilities have been explored, but have all been subsequently rejected. Firstly, spectral features originating from gallium were observed in the XPS data presented in Sec. 3.2. These features may arise from gallium in the substrate, but gallium segregation has been observed in other films, notably MnSb [91]. As such it is possible that gallium has segregated from the interface into the NiSb epilayer. The formation of GaSb or (Ga,Ni)Sb crystallites near the interface are conceivable, but both structures are cubic. As discussed above, none of the observed reflections index onto a face centred cubic lattice, ruling out both of these possibilities. However, for completeness, predicted peak positions based on GaSb and for (Ga,Mn)Sb, with 5 at.% of Mn, were calculated and are given in Appendix A.

Other possible explanations include off-stoichiometric crystallites, namely $Ni_x Sb$ and $NiSb_2$ and elemental antimony. However, these can be rejected almost immediately. Excess Ni atoms in NiSb form a solid solution and sit in Sb antisites, increasing the volume of the unit cell [93]. As such, the overall effect of excess Ni in a NiSb epilayer

would be a broadening of the NiSb reflections and not the appearance of a whole new family of reflections.

It also seems unlikely that elemental antimony or $NiSb_2$ would be present in these epilayers. Under our growth conditions the desorption rate of excess antimony from the surface should be greater than the arrival rate $(T_{sub} > T_{cell})$, rendering the possibility of excess antimony incorporation as either elemental antimony or $NiSb_2$ extremely small. However, to definitively rule out this possibility, Q_z values corresponding to reflections from elemental antimony and $NiSb_2$ were calculated. Again, none of these theoretical reflections matched the experimental data (see Appx. A).

The peak positions for elemental copper and aluminium have also been calculated and compared with the data. The X22C beamline and in-house diffractometers make use of either copper or aluminium sample holders and aluminium attenuators. It is possible that some of these peaks originate from the beam clipping the sample holder or diffraction from the polycrystalline attenuator could give rise to some of these observed features. However it is clear from the predicted peak positions in Tab. A.2 that neither of these can account for the unknown reflections.

Peak positions corresponding to elemental indium were calculated in a final attempt to identify these additional reflections. As explained in Chapter 4 our GaAs substrates are attached to sample plates using a combination of indium solder and In-Ga-Sn eutectic. Grown samples once extracted from the growth chamber are carefully removed from the sample plates, but some indium and eutectic is inevitably left behind on the back of the sample. Crystalline indium was investigated as an origin of the unknown reflections between Q_z 3.3 Å^{-1} and 4.2 Å^{-1}, particularly as these reflections diminish considerably upon heating the sample from 50 K to 300 K. Again however, theoretical peak positions do not coincide with the experimental data so this hypothesis has also been rejected.

Finally, the only other obvious explanation of these unidentified features in sample *B* is multiple scattering events. Whilst multiple scattering is not a particularly domi-

nant factor in XRD, multiple scattering is seen in some cases, for instance in Fig. 3.6. However, it is not possible to determine if these reflections are from multiple scattering events from these data already obtained and presented.

3.4   Epitaxial NiSb growth conditions

On the basis of the presented data, the following growth conditions are expected to produce high quality NiSb thin films and are based on the conditions used for sample C:

- $J \sim 7.5$

- $\mathrm{Ni}_{BEP} \sim 1.4{\times}10^{-7}$ mbar

- $T_{sub} = 420$ °C.

The samples grown with a smaller J showed the worst RHEED reconstruction and in the case of sample B had some XRD peaks which could not be adequately identified. Of course, more experiments will need to be conducted, but on the basis of the XRD, these conditions will produce epitaxial NiSb(0001) films on GaAs(111)B substrates.

3.5   Conclusions

To conclude, highly crystalline epitaxial NiSb films have been grown on GaAs(111)B substrates for the first time and oriented NiSb[0001]∥GaAs[111] with NiSb[2$\bar{1}\bar{1}$0]∥GaAs[110]. The 300 K c lattice lattice parameter for the three samples has been calculated as 5.125(5), 5.132(5) and 5.119(5) Å for samples A, B and C respectively. For the first time, surface reconstructions have been observed on NiSb(0001) thin films. The Sb-rich td(1×3) surface structure is believed to be similar to that of other binary pnictides, i.e. two-thirds of a monolayer of antimony arranged in chains on the surface. In addition, a (4×6) and "(4×4)" surface reconstructions have also been observed. Both reconstructions originate from the deposition of Ni onto (1×1) NiSb surfaces and neither have

been observed on (0001) planes of other binary pnictides. Moreover, the identification of the (4×4) is only tentative, as three different surfaces could give rise to the observed diffraction pattern.

An XRD study shows the films to generally be of a high quality although some unexpected additional reflections have been observed. Of these, some are attributed to small NiSb crystallites randomly oriented within the epilayer. Shoulders on some NiSb reflections may be the result of a thick strained layer at the interface, although this interpretation requires further experimental evidence. Finally, some extra reflections originate from an as yet entirely unknown source.

Chapter 4

Epitaxial growth of MnSb(0001) films

The first Warwick-based growth experiments of MnSb on III-V substrates were undertaken by Dr Stuart Hatfield under the supervision of Dr Gavin Bell between 2003 and 2006. These initial experiments were particularly encouraging, with cross sectional SEM micrographs showing a sharp interface without any chemical intermixing. Hatfield briefly investigated the J versus T_{sub} phase space in order to determine the optimum growth conditions. As part of that study, careful RHEED observations and STM of MnSb epilayers of thicknesses up to a few monolayers were conducted. Hatfield concludes that the optimum growth conditions were $J = 8$, $T_{sub} = 400$ °C and $Mn_{BEP} = 1 \times 10^{-7}$ mbar and that growth proceeds by the coalescence of epitaxial 3D islands which strain relax within a few monolayers [94].

One of the peculiarities of the MnSb growth work done to date is the observation of "mesa" morphology on MnSb(0001). It was seen that samples removed from the growth chamber typically exhibited a two-tone surface, where some parts were shiny and others, a white colour. The percentage of the surface that was shiny/white varied from sample to sample. Scanning electron microscopy (SEM) studies performed on samples ranging from entirely white to entirely shiny showed large scale changes in the surface morphology. Fig. 4.1 shows typical examples of white (top panels) and shiny (bottom panels) surface morphology. The striking quality of the white surfaces are the flat topped mesas separated by trenches up to tens of nanometres wide and hundreds of nanometres deep. The shiny regions are practically featureless on the micron and sub micron scale, with the exception of some MnSb crystallites protruding from the surface. Occasionally, features shown in d) are observed only in shiny regions. These
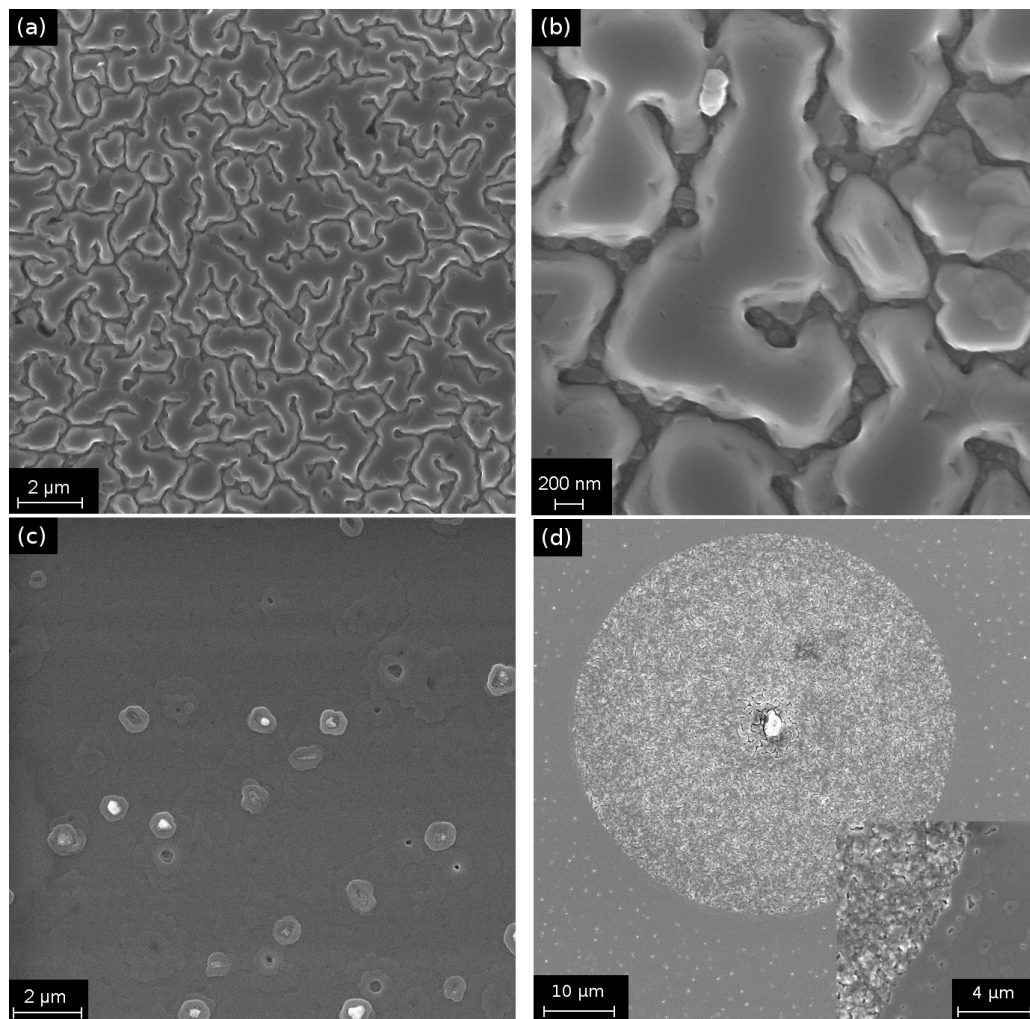
Figure 4.1: *Scanning electron micrographs of the two main MnSb(0001) surface morphologies. (a) and (b) show the "mesa" morphology, composed of flat topped MnSb crystallites separated by trenches 10s of nanometres wide and hundreds of nanometres deep. (c) and (d) are from flat MnSb samples.*

features are thought to occur due to the presence of a condensation nucleus, such as a dust particle, which preferentially reacts to one of the growth elements. This results in the surrounding region having a different effective BEP ratio leading to a radically different surface morphology. The transition from this region into a "normal" region is very abrupt, as shown in the inset.

Finally, one of the most interesting recent results to have been obtained is the observation using transmission electrom microscopy (TEM) of wurtzite and cubic MnSb
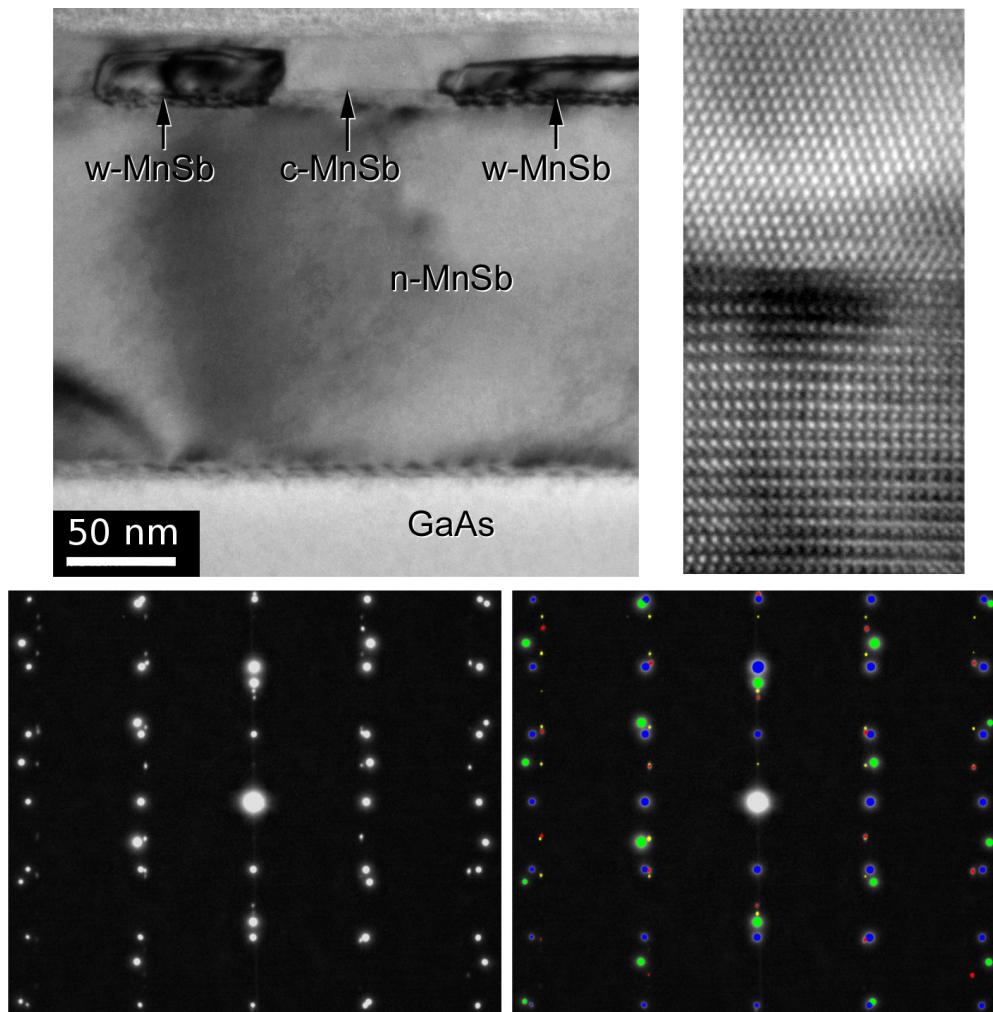
Figure 4.2: *High resolution TEM images and selected area diffraction (SADP) patterns from a MnSb(0001) thin film. The HRTEM image in the top left of the image shows the GaAs(111) substrate with a n-MnSb epilayer containing c-MnSb and w-MnSb crystallites. The HRTEM image in the top right is a close-up of the interface between n-MnSb and c-MnSb which shows a clear change in the structure. The SADP shown in the bottom left is indexed in the bottom right: green circles correspond to GaAs(111), n-MnSb are blue, c-MnSb are red and w-MnSb are yellow.*

crystallites (w-MnSb and c-MnSb) within niccolite MnSb (n-MnSb) epilayers. Some images taken from these experiments are given in Fig. 4.2. The top-left image in this figure shows clearly the different niccolite, wurtzite and cubic regions within the epilayer. The image in the top-right is a close-up of the interface between n-MnSb and c-MnSb and shows the sharp change in crystal structure. The bottom two images are selected

area diffraction patterns (SADP) from a region containing all three phases. The bottom-left image is the raw data and the bottom-right is the same data but indexed as follows: green circles are diffraction beams from the GaAs(111)B substrate, blue circles are from n-MnSb, red from c-MnSb and yellow pertain to w-MnSb. This is a unique observation with no comparable results for MnSb or any other BP in the literature.

In this chapter, the conditions used to grow MnSb(0001) are given in Sec. 4.1. The changes and additions to the growth procedure which have been introduced during this project will be introduced, specifically a new two-stage growth method and an antimony capping stage. In Sec. 4.2 a combined XPS, SEM and LEED study will show the results of a surface preparation investigation. Sec. 4.3 presents the work carried out in an attempt to understand the reasons behind the macroscopical surface morphology and the formation of c-MnSb and w-MnSb. Finally a summary of the experimental results is given in Sec. 4.4.

4.1 Growth of MnSb(0001) on GaAs(111) substrates

All MnSb thin films used during this work were grown on GaAs(111)B substrates. These substrates were prepared in the way described in Sec. 3.1. The typical RHEED pattern following this procedure was a td(1×3) and is shown in Fig. 4.3.

Following this preparation, all MnSb samples were grown using the following two-stage growth method:

- Stage 1:

    - $J = 6.5$ (Mn$_{BEP} \sim 1.2$–1.5×10^{-7} mbar)

    - $T_{sub} = 350$ °C

    - t $= 60$ s

- Stage 2:

    - $J = 6.5$ (Mn$_{BEP} \sim 1.2$–1.5×10^{-7} mbar)
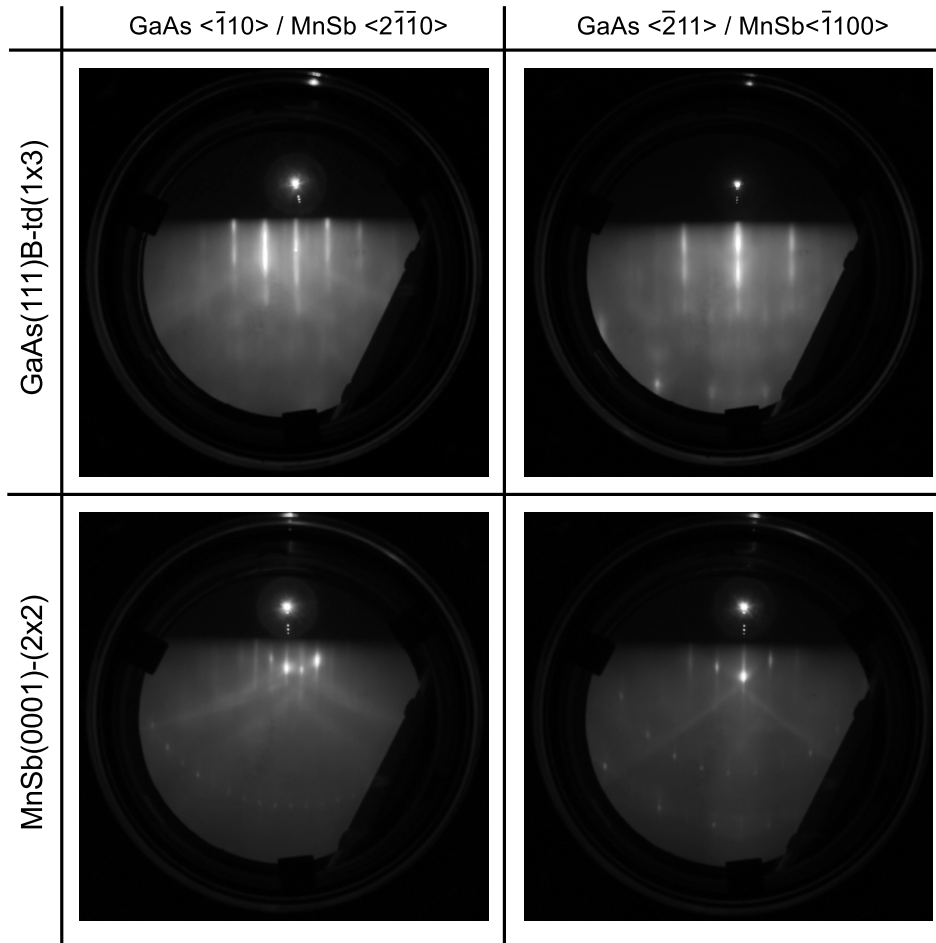
Figure 4.3: *RHEED patterns from GaAs(111)B substrates after preparation and MnSb(0001) thin films after growth.*

- $T_{sub} = 420\ ^\circ C$

- t $\geq$ 2 minutes

The two stage methodology was used in an attempt to limit the fraction of the epilayer adopting the mesa morphology shown in Fig. 4.1(a) and (b). The vast majority of samples grown using this procedure produced a sharp and intense (2×2) diffraction pattern (Fig. 4.3) and were largely free of the white surface which characterises the mesa morphology. This is important, as smooth surfaces are necessary for quantitative surface structure determination as well as for technological applications. However, some samples still emerged from the growth chamber with mesa morphology in some regions
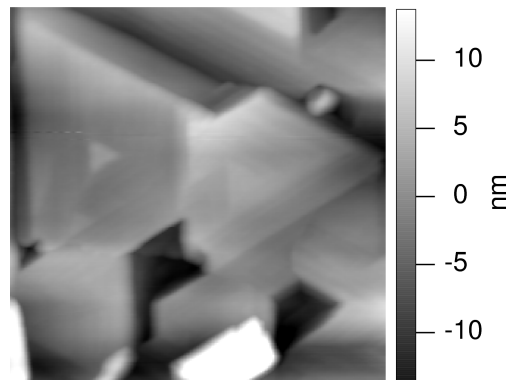
Figure 4.4: *Atomic force micrograph of a MnSb epilayer after the Sb-capping procedure described in the text. The triangular features are epitaxial antimony islands.*

of the surface.

The most recent development to the growth procedure is the addition of an antimony capping stage. This third stage makes use of the same Sb_{BEP} as the first two stages but $T_{sub} = 250$ °C and t = 2 minutes. During this capping stage the (2×2) diffraction pattern changed to a (1×1), before changing to the Sb-rich td(1×4) reconstruction. In turn this pattern faded to give long and broad (1×1) streaks with a high background. Atomic force microscopy measurements showed Sb-capped samples had surfaces covered with triangular features (Fig. 4.4). These features are believed to be crystalline antimony which gives rise to the (1×1) diffraction pattern even after two minutes of deposition.

4.2   Preparation of MnSb(0001) surfaces

Initial XPS measurements carried out by Hatfield on MnSb(0001) epilayers exposed to atmospheric conditions showed heavy oxidation with Mn-oxides being resistant to IBA treatments. In this study, XPS experiments were performed on a smooth MnSb epilayer which did not display the mesa morphology after it had been exposed to atmospheric conditions. Data were acquired as-loaded and after further preparation treatments: after a 10 s *ex situ* HCl etch; after 1 hour anneal; and after 10 minute Ar^+ ion bombard (IB).
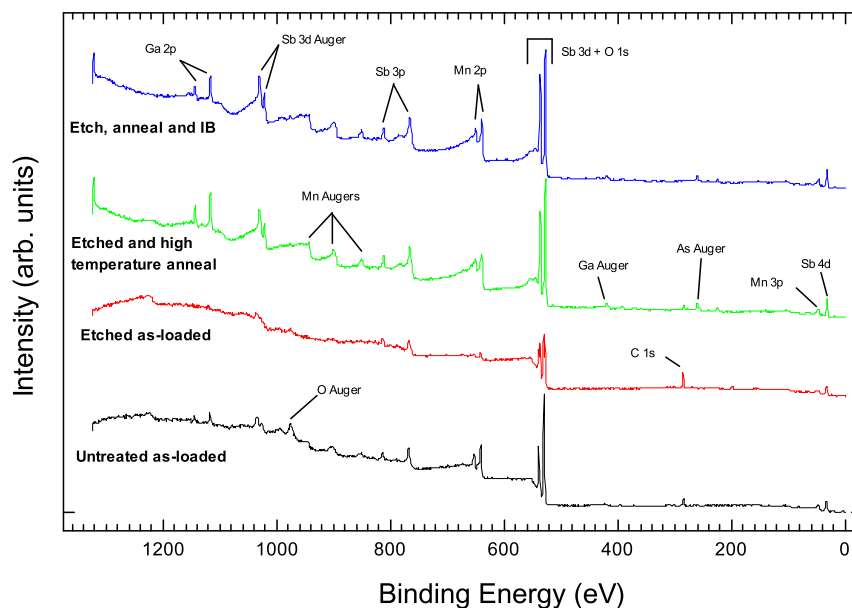
Figure 4.5: *Survey XPS scans of the MnSb(0001) as-loaded and after sequential treatment stages.*

The aim of this study is to define an overall treatment method which produces clean MnSb(0001) surfaces with the (2×2) surface reconstruction.

Survey scans after each treatment method are given in Fig. 4.5. Scans are offset vertically for clarity. The sample as-loaded is dominated by oxygen with a strong Mn 2p signal relative to the Sb 3p indicating a manganese-rich surface. The 10 second HCl acid etch strongly reduces the O 1s and Mn 3p features, however the etch has little effect on the C 1s feature. The subsequent anneal results in a strong increase of the Sb 3p, Sb 3d and Auger features and signals a marked improvement in the surface stoichiometry. In addition, the C 1s feature is strongly reduced but pronounced Ga 2p and arsenic Auger signals appear. The Ar$^+$ IB does little to change the overall appearance of the survey scan.

The strong Ga 2p and arsenic Auger signals after the anneal is a troublesome result. A previous study of MnSb growth showed gallium segregation from the substrate [91], but no segregation of arsenic was observed. The presence of both gallium and arsenic features in an otherwise flat sample indicates likely disruption to the surface
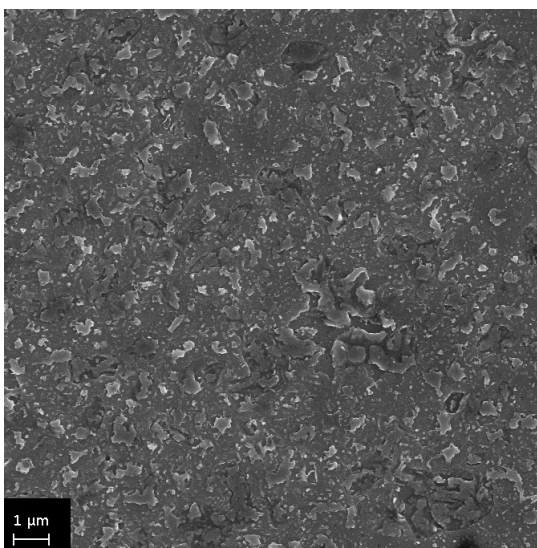
Figure 4.6: *SEM micrograph of the MnSb after the XPS experiments. Severe damage to the MnSb epilayer is evident leading to the gallium and arsenic signals after the "high temperature" anneal described in the text.*

layer. Scanning electron microscopy was performed on this sample at Warwick after the XPS experiments. A typical SEM micrograph showing large scale disruption to the epilayer can be seen in Fig. 4.6. It is believed the surface has been over annealed, probably above its non-congruent temperature. For this reason the data in Figs. 4.5 and 4.7 has been labelled as "high temperature" anneal.

Despite the damage done to the surface during the anneal phase a number of important conclusions can be drawn through peak area analysis of this sample and through observing changes in the Mn 3p and Sb 4d peak shapes shown in Fig. 4.7. Firstly the as-loaded scan is totally dominated by oxygen and carbon, the two species between them contributing $(58 \pm 2)\%$ to the surface composition. The Sb 4d region shown in Fig. 4.7(b) shows a large feature at 34–36 eV which is attributed to Sb-oxides. The surface Sb/Mn ratio calculated using the Mn 3p and Sb 4d peak areas is (0.78 ± 0.02) at this stage. The corresponding values after the etch show the Sb/Mn ratio has increased to (1.13 ± 0.03) whilst the oxygen composition has dropped significantly to $(13.3 \pm 0.4)\%$. This is still a significant amount of oxygen, but it should be noted
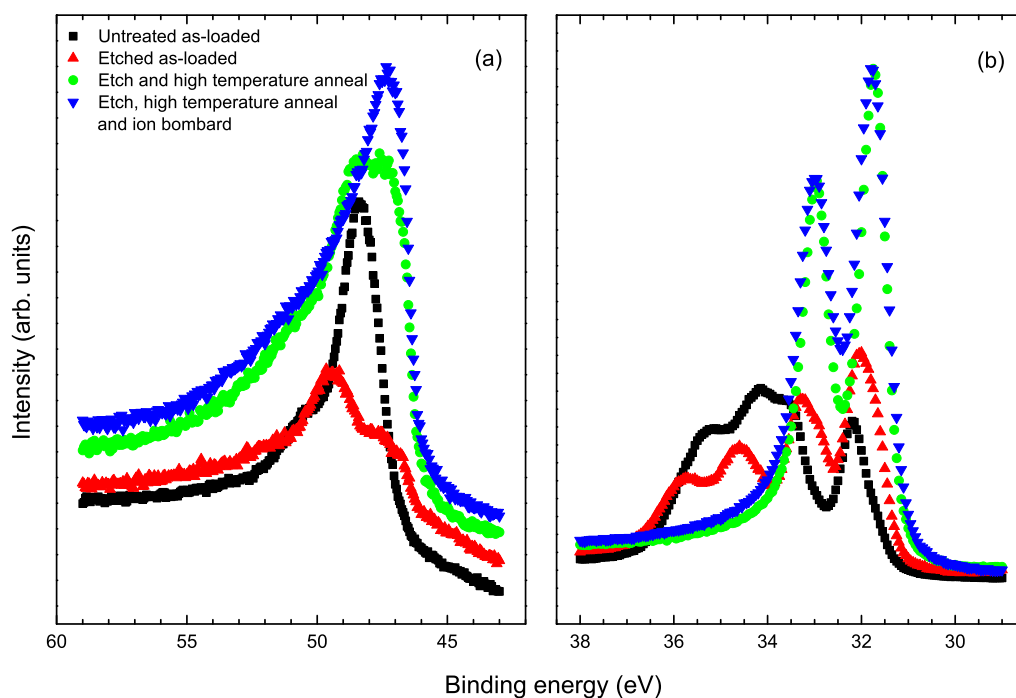
Figure 4.7: *XPS data taken from an air-contaminated MnSb(0001) sample as-loaded and after several sequential treatment stages. (a) Mn 3p region. Multiple components are evident in this region with the peak at 48.5 aV being ascribed to Mn-oxides. The peak at 47 eV is attributed to a Mn-Sb bonding configuration. (b) Sb 4d region. The peaks at approximately 34.5 eV and 35.5 eV arise from Sb-oxides. The doublet at 31.5 and 33.0 eV correspond to the Sb-Mn bulk bonding configuration.*

that the chemical fume cupboard in which the etch was conducted is not by the XPS chamber, the base pressure in the preparation chamber is only 10^{-8} mbar and that there was no way to efficiently dry the sample after rinsing in de-ionised water post-etch. As a result, a certain degree of re-oxidation will have occurred. Still, the Mn 3p peak shape has changed dramatically as a result of the etch with the appearance of a low BE peak at approximately 46.5 eV, whilst the high BE Sb-oxide peak remains. This indicates the etch has preferentially removed Mn-oxides and left the surface Sb-rich. The anneal stage leads to a total loss of this high BE Sb-oxide peak and a sharpening up of the low BE Mn 3p peak. However at this stage in the treatment the surface Sb/Mn ratio has dropped to (0.71 ± 0.02), meaning the anneal has acted to remove excess antimony from the surface. Finally, after the IB, the surface Sb/Mn ratio has
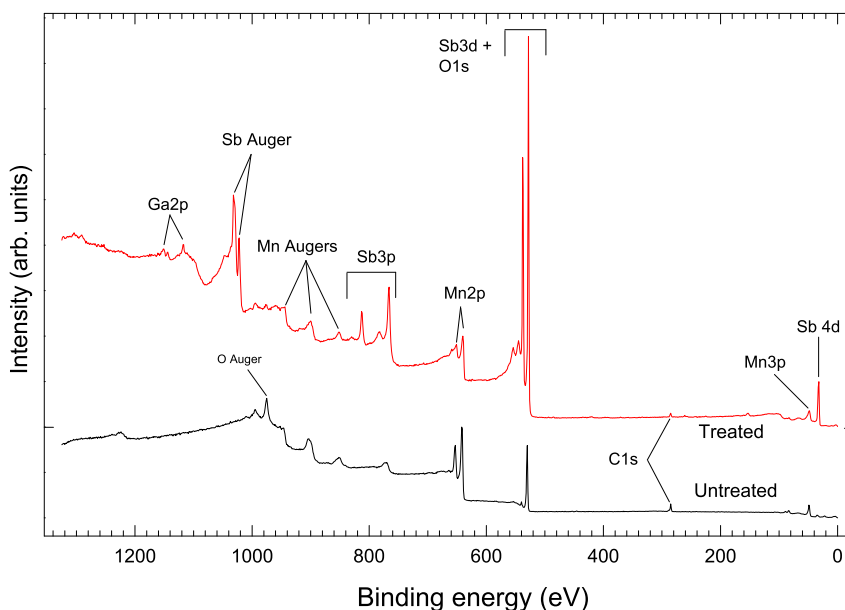
Figure 4.8: *XPS survey scans of a MnSb(0001) thin film exposed to atmosphere as-loaded and after the treatment method described in the text.*

increased to (0.82 ± 0.02) with little change in the Sb 4d peak shape, indicating the preferential sputtering of manganese over antimony in the near surface region.

From these observations an ideal surface preparation method is suggested to be:

- 10 s HCl etch in 18 M strength acid followed by rinsing in de-ionised water, blown dry with a high pressure dry nitrogen source and immediate insertion into vacuum

- Degas at 300 °C for 30 minutes

- Ion bombard using Ar^+ at 500 eV for 10 minutes

- Flash anneal to 375 °C.

The efficacy of this preparation method is evident in the XPS survey scans in Fig. 4.8 and the LEED image presented in Fig. 4.9(a). The XPS shows a marked reduction in the O 1s feature and the appearance of several antimony peaks. No carbon is found to exist on the sample after the treatment, with just a slight appearance of Ga 2p features. The origin of this weak signal is believed to be due to some gallium segregation as opposed

(a)   (b)
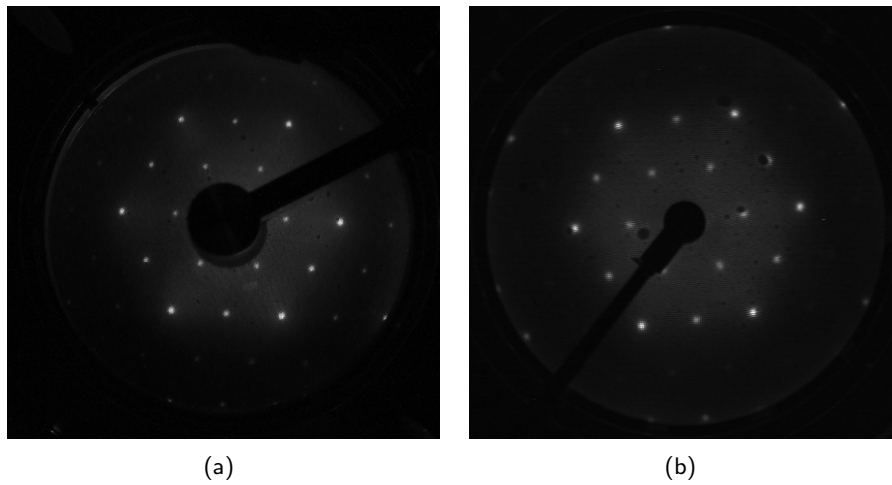
Figure 4.9: *(a) 55 eV LEED image taken at the MEIS facility of an uncapped MnSb thin film after HCl etching and IBA. (b) 60 eV LEED pattern for an Sb-capped MnSb thin film after IBA cycles only. This figure is from the LEED I-V data discussed in Chap. 6.*

to disruption of the overlayer [91]. The diffraction pattern in Fig. 4.9(a), obtained from an air-exposed MnSb(0001) prepared using the above method, shows a clear (2×2) pattern with sharp integer and fractional order streaks with a low background. These are necessary requirements before any quantitative surface structure determination work can be conducted. This preparation method has been used throughout this thesis where uncapped MnSb(0001) have been transported in air.

Briefly, the preparation of MnSb(0001) epilayers which have been capped is very similar to the procedure outlined above for uncapped MnSb(0001). The Sb-cap physically passivates the underlying manganese from reacting with atmospheric oxygen and so the HCl etching step is no longer required. Removing Sb-oxides is a simple case of gentle ion bombarding and annealing, repeated as necessary with care taken not to maintain the substrate temperature above $\sim$375 °C. The surface diffraction pattern from an Sb-capped sample after this treatment is given in Fig. 4.9(b).

4.3 J dependent study of MnSb(0001)/GaAs(111)

The purpose of this investigation was to ascertain if there is any correlation between J and the observed surface morphologies (shiny/white) or the polymorphism seen with TEM. To this end a set six of samples were grown for a total of 30 minutes each (estimated thicknesses of ∼180 nm) using the two stage method outlined in Sec. 4.1 with J varied between 6.6 and 7.5. To keep the number of variables to a minimum the manganese BEP was kept between 1.1–1.2×10^{-7} mbar and the antimony BEP varied to obtain the desired J. The RHEED was monitored during growth with SEM and XRD performed after growth. A summary of the growth conditions and RHEED observations is given in Tab. 4.1.

From the RHEED observations, the broad trend is that samples grown with J equal to or larger than 7.3 grew with a (1×1) surface structure throughout the growth and gave diffraction patterns which had higher backgrounds relative to the other samples. There was, however, a large degree of variability in the sharpness and periodicity of the RHEED pattern below this value.

4.3.1 Surface morphology

The final surface morphology of the MnSb epilayers was studied using SEM. The centre regions of both samples C and F were visibly shiny and were relatively featureless on the micronscale in the SEM. However, the edges of both samples have a complex surface microstructure, as shown in Fig. 4.10. Regions of the surface up to 5×2 mm were covered with protrusions which appear bright in the SEM images. Underneath the protrusions, a hexagonal crystal is evident, but it is far removed from the either the smooth or the mesa morphology which has typically been seen in the past. In contrast, samples A, B and D were smooth and flat on the micron and sub-micron scale. Both A and D were visibly shiny with the exception of small mesa terraces located at one corner of each sample. Sample B was also visibly shiny save for a region covering ∼20%

Table 4.1: *A summary of the MnSb(0001) samples grown for the J dependency study.*

Sample	J	RHEED observations
A	6.6	Grew as a (2×2) pattern throughout. No transmission diffraction features.
B	6.7	Initially high background and weak pattern. Sharpened up towards the end of growth. Grew (1×1) throughout.
C	7.0	Initial growth characterised by a very poor and weak (1×1). Ended up as a very sharp (1×1). Could not obtain (2×2) surface reconstruction at the end.
D	7.2	Initial pattern was a faint (1×1), before sharpening up into a (2×2). Final pattern was an intense and sharp (2×2).
E	7.3	Grew (1×1) throughout. Initially a very weak (1×1) with faint streaks relative to the background, but sharpened up considerably by the end.
F	7.5	Grew (1×1) throughout. Final streak intensity was very faint relative to the background.

of the surface which consisted of the protrusions seen on samples *C* and *F*. Finally, the surface of sample *E* was largely covered with the mesa morphology.

To a first approximation it would seem that a J of <7.2 produces the smoothest samples with the best morphology, whilst a larger J gives rise to more complex surface morphologies. Moreover, the quality and reconstruction of the final RHEED pattern correlates directly with the surface morphology, with sharp (2×2) patterns indicating a smooth surface whilst samples which grew (1×1) with higher backgrounds had large regions of the surface showing a more complex morphology.

However, all of the samples had more than one surface morphology, even if the second morphology was confined to a small patch in one corner of the sample. Moreover, the transitions between "smooth" and "rough" regions is extremely abrupt, similar to that seen in Fig. 4.1(d). This suggests that the growth of MnSb on GaAs(111)B substrates is very sensitive to the beam flux ratio. Both the manganese and antimony cells are mounted onto the growth chamber through $2\frac{3}{4}''$ flanges, but for historical reasons, the manganese cell is recessed further down the feedthrough and is thus further from the
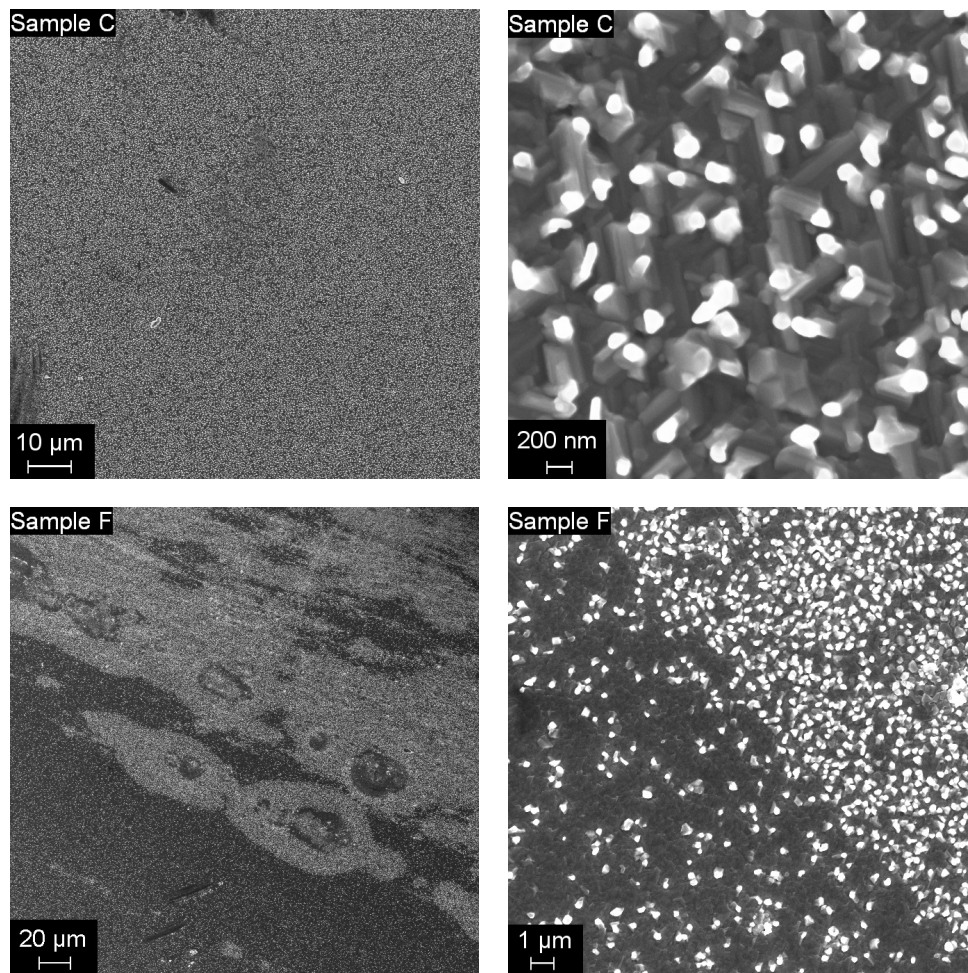
Figure 4.10: *A selection of SEM micrographs for samples* C *and* F. *Both samples show microstructures previously unseen on MnSb(0001) surfaces. Both surfaces have large regions (>100 μm) covered with protrusions which appear bright in the micrographs. The boundary between the "light" and "dark" regions in sample* F *is abrupt.*

sample. This leads to much greater collimation of the manganese beam flux relative to the antimony which can give rise to a variation in J of up to 10% across a 10×10 mm sample [94]. This was not considered to be a significant problem at the time the MBE chamber was commissioned, but these SEM observations indicate that the growth is in fact very sensitive to the local beam flux ratio.

4.3.2   X-ray diffraction

The XRD data presented in Fig. 4.11 is a Q_z scan of the MnSb films and was obtained using an in-house Philips PANalytical X'Pert x-ray diffractometer. The first thing to note is the lack of any clear trend in J between the different samples. This may be due to the variation in J of up to 10% across a sample which was mentioned above. The diffractomer used for these experiments is line focussed, essentially meaning a strip with a width of $\sim$5 mm is incident upon the sample. In all likelihood a range of effective local J values contributes to the diffraction pattern for each sample but it is unclear what this range is.

The most intense diffraction features in these data are readily indexed to n-MnSb(0001) and GaAs(111) planes and are labelled as such in Fig. 4.11. The GaAs and MnSb c lattice parameters can be calculated from these indexed reflections. The lattice parameter of the GaAs substrates is calculated separately for each dataset using a least squares minimisation method under the assumption of a constant 2θ offset which differs from sample to sample. This offset is then used to find the c lattice parameter of the n-MnSb epilayer and of the c-MnSb crystallites when present. The lattice parameter values determined using this method are given in Tab. 4.2. The determined values for GaAs agree within experimental error to the accepted value of 5.6533 Å [92]. The value for c in n-MnSb agree closely with those published [95, 96] for all samples except for sample D, which shows a difference of approximately -0.5%. This n-MnSb layer is under a compressive strain and may be indicative of a volume conserving distortion, although the origin of such a distortion is unclear.

In addition to the GaAs and n-MnSb reflections, some diffraction features in the data for samples B and F can be indexed onto c-MnSb (111), (222) and (333) planes. From these reflections the lattice parameter of the c-MnSb crystallites is found to be 6.542(5) Å and 6.507(5) Å respectively for samples B and F (Tab. 4.2). From the SADP presented in Fig. 4.2 the lattice parameter of the cubic crystallites is found to be
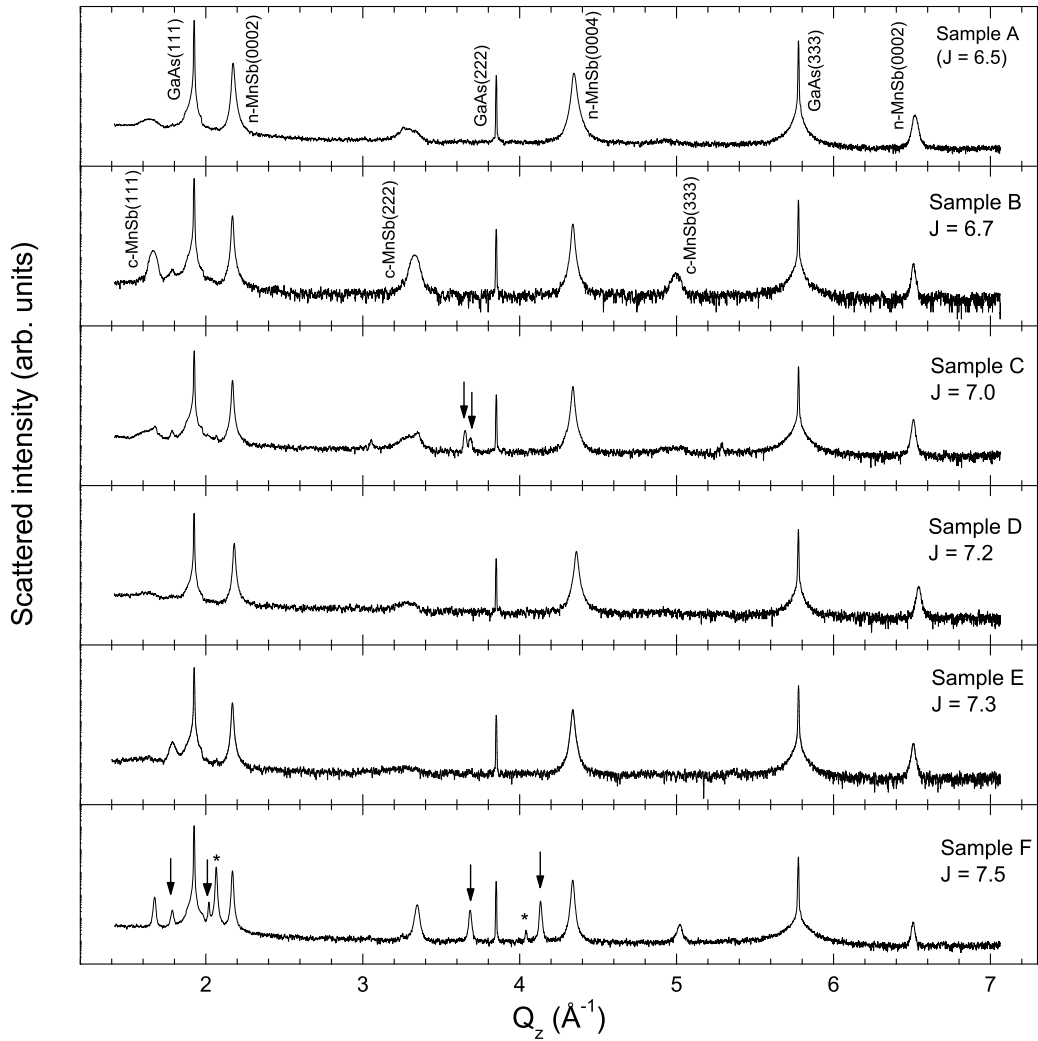
Figure 4.11: *Hard x-ray θ–2θ scans of the MnSb films. Reflections corresponding to GaAs(111), n-MnSb(0001) and c-MnSb(111) are indexed accordingly. Reflections marked with an asterisk are (1$\bar{1}$01) and (2$\bar{2}$02) reflections, originating from small misoriented MnSb crystallites. Reflections marked with arrows are unidentified.*

6.502 Å, which is in very close agreement with the value found for c-MnSb in sample *F*. The discrepancy with sample *B* is likely due to a macroscopic strain, as this would lead to a systematic shift of the XRD diffraction peaks. On this basis, the Williamson-Hall analysis (Eq. 2.26) can estimate the amount of strain dispersion. In this case, the maximum fractional change in the lattice parameter, η, for samples *B* and *F* has been calculated as 0.008 ± 0.001 and 0.005 ± 0.001 respectively. It must be noted that

Table 4.2: *Lattice parameters of GaAs, n-MnSb and c-MnSb calculated from the reflections labelled in Fig. 4.11.*

Sample	GaAs a ($\pm$ 0.001 Å)	n-MnSb c ($\pm$ 0.001 Å)	c-MnSb a ($\pm$ 0.005 Å)
A	5.653	5.797	-
B	5.654	5.794	6.542
C	5.654	5.794	-
D	5.653	5.765	-
E	5.653	5.795	-
F	5.653	5.794	6.507

the analysis from which these values are derived makes use of a limited number of data points. This necessarily gives rise to the large error bars, but there is a clear difference in the strain state of the two different crystallites, with the crystallites in sample *B* under ∼50% more strain. Moreover, from this analysis the crystals giving rise to these reflections are approximately 4 times larger in sample *F* than in *B*.

Further to the peaks already discussed, there are a number of unidentified reflections. Of particular interest are features in the data for samples *A* and *C* around the positions cubic reflections would be expected, specifically at Q_z ∼1.67 and 3.35 Å^{-1}. These regions are shown in Fig. 4.12, with data for samples *A* and *C* offset vertically for clarity. The (111) and (222) reflections for sample *C* have similar shapes indicating they originate from the same crystallite but are clearly composed of multiple peaks. These features may arise due to a tetragonal distortion of a cubic MnSb lattice. The (222) reflection in sample *A* supports this hypothesis, as the shape is very similar but reversed relative to sample *C*. Such a distortion is predicted in a DFT study by Zheng and Davenport [97] who claim the ideal cubic structure ($c/a = 1$) is mechanically unstable, leading to a tetragonal distortion. This appears to be the case here.

The other reflections apparent in Fig. 4.11 are more complex to interpret. It is observed in XPS that gallium segregates from the substrate into the overlayer, rendering the formation of cubic intermetallics such as (Ga,Mn)Sb and (Ga,Mn)As a possibility.
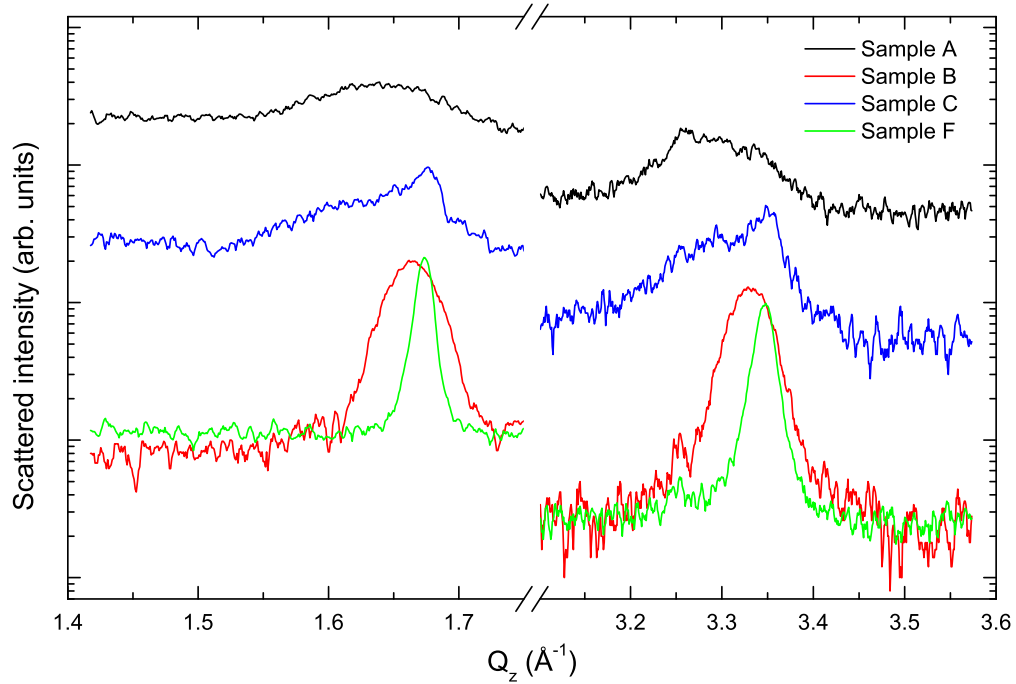
Figure 4.12: *Region around the c-MnSb (111) and (222) reflections for Samples* A, B, C *and* F. *Data for samples* A *and* C *are offset vertically for clarity. The shape of the diffraction features for samples* A *and* C *are due to a tetragonal distortion of c-MnSb crystallites.*

The lattice parameters of these phases are approximately 5.7 Å for (Ga,Mn)As [98] and 6.1 Å for (Ga,Mn)Sb [99, 100], with the precise value of a depending on the Ga/Mn stoichiometry. The reflections at $Q_z = 2.02$ and 4.04 Å^{-1} can be indexed using the graphical method outlined in Sec. 2.4 to $(h^2 + k^2 + l^2) = 4$ and 16 respectively. These peaks may originate from (002) and (004) planes of a cubic lattice with a equal to 6.221 Å and oriented (001)‖MnSb(0001), or from (0002) and (0004) planes of a hexagonal lattice with c also equal 6.221 Å and oriented (0001)‖MnSb(0001). (Ga,Mn)Sb formation in the vicinity of the interface could give rise to a cubic crystal with this lattice parameter, but only if 30% of the gallium was substituted for manganese. This crystal would need to be oriented (001)‖GaAs(111), which is not expected. Furthermore, these reflections do not arise from w-MnSb inclusions. Theoretical calculations of w-MnSb have determined the c parameter to be 7.138 Å [20] whilst the TEM SADP pattern

showed the c parameter to be 7.003 Å. Given these uncertainties, the precise identification of these two reflections is unknown, but the lattice parameter of the crystal is 6.221 Å.

Of the other reflections, those at $Q_z = 2.067$ Å^{-1} and 4.133 Å^{-1} in sample *F* could originate from either (001) oriented crystallites of (Ga,Mn)Sb with 5 at.% of Mn, or from $(1\bar{1}01)$ and $(2\bar{2}02)$ planes in MnSb. Whilst an intermetallic with this particular chemical composition is plausible, the orientation of the crystal again seems unlikely. As such, these reflections are believed to originate from MnSb$(1\bar{1}01)$ crystallites.

Finally reflections at $Q_z = 1.787$, 2.019, 3.652, 3.685 and 4.133 Å^{-1} in the data for samples *C* and *F* remain unindexed. In addition to checking these reflections against the predicted peak positions for all the MnSb polymorphs and Ga-Mn intermetallics, elemental copper, aluminium, indium, antimony as well as MnO, Mn$_2$Sb and MnSb$_2$ were checked as possible sources for all of the additional reflections. The predicted peak positions are summarised in Appx. A, but suffice to say, none of these predicted reflections match these unindexed peaks.

4.4 Conclusion

To conclude, MnSb(0001) with a c lattice parameter of 5.795(2) Å have been successfully grown on GaAs(111)B substrates. These films were grown using a new two stage growth procedure as this limited the amount of surface displaying the "mesa" morphology. A third antimony capping stage has been added to the growth procedure. It has been shown that this cap is easily removed through careful IBA cycles, resulting in a (2×2) surface reconstruction. Uncapped thin films can be prepared using a simple HCl and IBA method, after which the surfaces are seen to be free of contamination, well ordered and reconstructed, which are necessary requirements before undertaking quantitative surface structure determination work. However, annealing above ∼375–400 °C results in large scale disruption to the epilayer. Moreover, it has been observed that

the surface morphology of MnSb(0001) is particularly sensitive to the local beam flux ratio. Variations in J of a few percent result in large scale morphological changes in the epilayer, with a previously unseen surface morphology having been discovered during this work.

An XRD investigation of MnSb thin films show some reflections which cannot be indexed onto any obvious material or compound. However, of much greater significance is clear, unequivocal evidence for c-MnSb crystallites within four of the six samples investigated. Each of these c-MnSb crystallites appear to be in different strain states. The mechanism which drives the formation of c-MnSb within these films is unclear, but the result is unique, with no similar results documented within the literature for MnSb or any other BP.

Chapter 5

Magnetic properties of epitaxial MnSb(0001)

Bulk MnSb has a magnetic moment of 3.3 μ_B per manganese atom with a reported Curie temperature (T_c) of between 550 K and 590 K [95, 101, 102]. To characterise the magnetic properties of the MnSb thin films vibrating sample magnetometry (VSM) and the superconducting quantum interference device (SQUID) were used to collect hysteresis loops and magnetisation versus temperature (MvT) curves respectively. Circularly polarised soft x-ray spectroscopy experiments were performed on thin films of MnSb(0001) in order to characterise the surface magnetic properties.

5.1 Bulk magnetometry

VSM and SQUID experiments were conducted in-house on MnSb(0001) samples of approximately 2×2 mm. Samples were mounted on polyetherether ketone (PEEK) sample holders using polytetrafluoroethylene (PTFE) tape. The combined PEEK holder and PTFE tape had a small diamagnetic response which was measured separately and subtracted from the MnSb(0001) hysteresis data. The GaAs substrates also have a small diamagnetic response which was not taken into consideration.

Hysteresis loops acquired with the applied field parallel and perpendicular to the sample surface are shown in Fig. 5.1. The negative gradient apparent in both data sets at large field are a diamagnetic contribution to the overall magnetisation from the GaAs substrate. From these data MnSb thin films show an "easy plane" and "hard axis" type magnetisation response which is in agreement with first principles calculations and experimental results of the MnSb magnetocrystalline anisotropy energy [101, 103]. The inset in Fig. 5.1 is a close up around the origin of the in-plane magnetisation. The
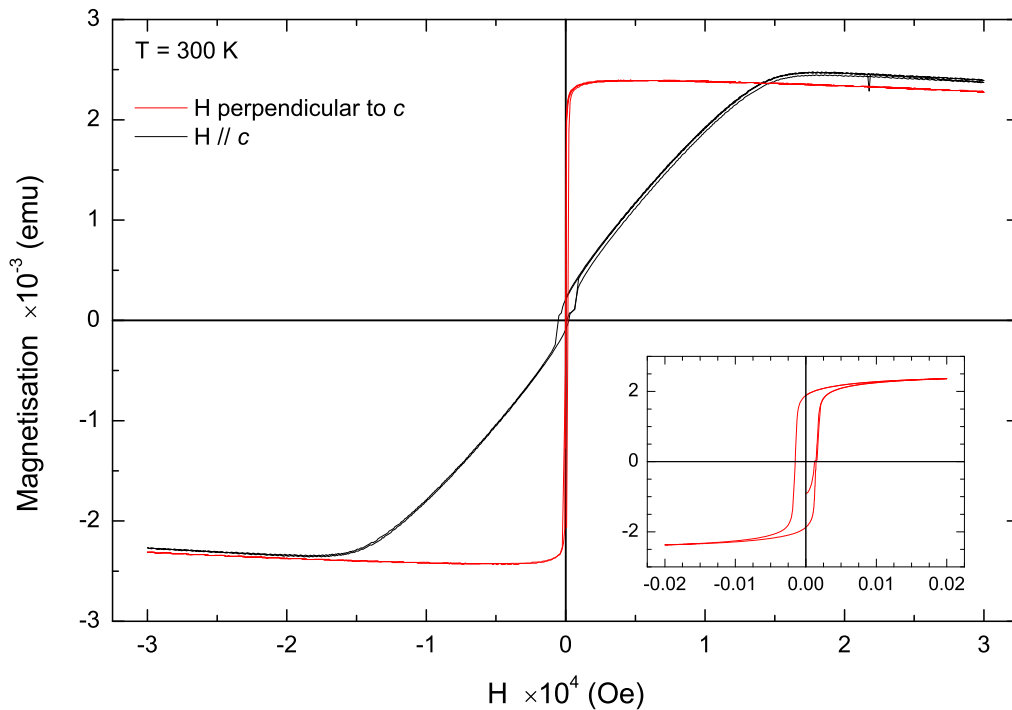
Figure 5.1: *Hysteresis loops of MnSb(0001) with the applied field in-plane and out-of-plane. The sample has an easy plane and hard axis parallel to <0001>. The inset shows a close up of the in-plane magnetisation data. The coercive field is found to be (14.7 ± 0.5) Oe with a remnant magnetisation of (0.79 ± 0.05)M_{sat}.*

coercive field, H_c is found to be (14.7 ± 0.5) Oe in-plane with a remnant magnetisation of (0.79 ± 0.05)M_{sat}. The value for the coercive field is considerably smaller than the previously published values of 120–560 Oe [104, 105, 106]. It must be noted that the quality of the thin films used in those experiments was relatively low, being either polycrystalline or highly textured and granular, which is in contrast to the high quality and well oriented samples grown in this study. Finally on the basis of a crude estimate of the epilayer thickness the saturation magnetisation is found to be (3.1 ± 0.5) μ_B per manganese atom. This is in broad agreement with published values.

Magnetisation versus temperature data was acquired using the SQUID on a sample of thickness 250 nm and is shown in Fig. 5.2. The data was acquired in the presence of a 4 kOe external field applied parallel to the sample surface ($H_0 \perp c$) with the temperature ramped down from 740 K to 317 K. From these data the T_C is estimated
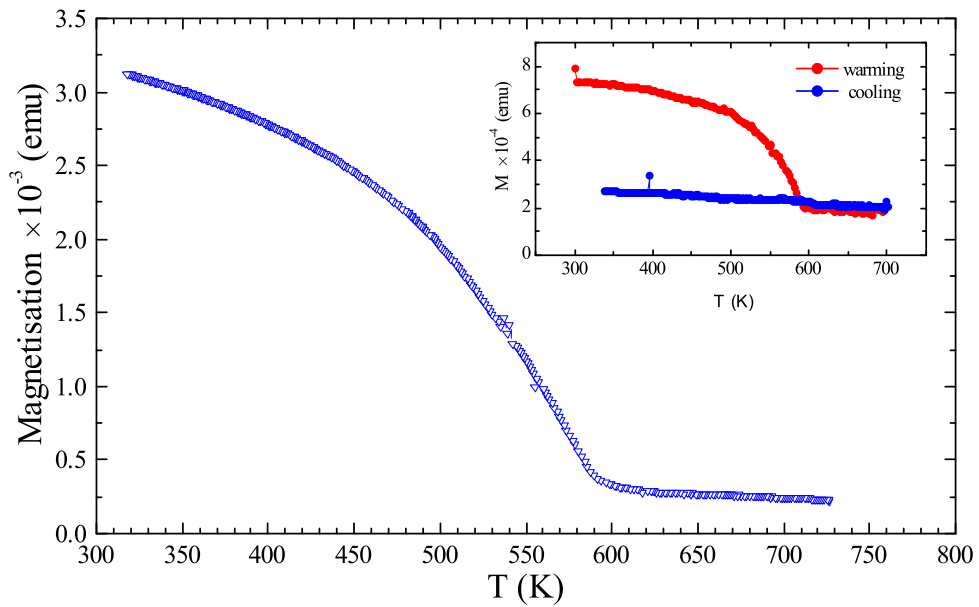
Figure 5.2: *Magnetisation versus temperature for a 250 nm thick MnSb(0001) film in a 4 kOe external field applied parallel to the sample surface. The T_C for this sample is found to be 590 K. The inset shows equivalent data for a sample with a thickness of 50 nm. The sample shows the correct behaviour during heating but shows no ferromagnetism upon cooling, demonstrating the sample has decomposed during the heating cycle.*

to be 590 K which is in very good agreement with published values. The inset in Fig. 5.2 shows equivalent data for a sample with an estimated thickness of 50 nm. Upon heating the sample shows the correct behaviour and has a T_c similar to that of the thicker film. However there is no ferromagnetic moment apparent as the film is cooled. It should be noted that the atmosphere within which the sample sits is a poor vacuum with helium being the dominant residual gas. As such, and with specific reference to the the XPS and SEM results in Sec. 4.2, it is believed the loss of ferromagnetic ordering is a result of thermal decomposition during the prolonged heating cycle and not extreme oxidation from heating the thin epilayer in an atmosphere containing a large partial pressure of oxygen.

5.2 Polarised soft x-ray spectroscopy

Soft x-ray spectroscopy experiments were performed at beamline X13A at the NSLS, USA [107]. Two thin film samples of approximately 50 nm thickness were prepared according to Sec. 4.1. Sample *A* was uncapped and scanned before and after a HCl etch and sample *B* was Sb-capped and scanned as-loaded only. The purpose of these experiments was to determine whether the MnSb(0001) surface is itself magnetic and if a magnetic surface could be recovered from a sample which had been oxidised through exposure to atmospheric conditions. To do this two different experimental geometries were chosen to exploit the capabilities of the X13A beamline. At a grazing angle of incidence slightly larger than the critical angle, x-ray resonant magnetic scattering (XMRS) and total electron yield (TEY) data were recorded, whilst at larger angles of incidence only the TEY data can be recorded. Of the two, XMRS probes mostly the "bulk" of the film while TEY measurements are approximately as surface sensitive as Auger electron spectroscopy. The two geometries then enable a comparison between the surface and bulk magnetic properties to be drawn. There are however some complications which will become clear that prohibit detailed sum-rule analysis for the TEY data. For all samples, data was taken at the Mn $L_{2,3}$ edge and the Sb $M_{4,5}$. As the Sb M absorption edge data is particularly weak and shows no dichroism, whilst the Mn L absorption edge and dichroism signals are strong, the Sb M edge data is omitted from the following for the purposes of brevity.

Fig. 5.3 shows the TEY XAS and flipping ratio data taken for both sample *A* and *B*. Complex fine structures are observed in all three datasets, with the L_3 edge consisting of three components and the L_2 edge consisting of two. The XAS for sample *A* after etching changes dramatically, with higher energy components at both the L_3 and L_2 reduced in intensity. These features are attributed to Mn-oxide species which are removed with the HCl etch. Even after the etch, the two L edges are composed of multiple features. Such fine structure is seen in other manganese materials and
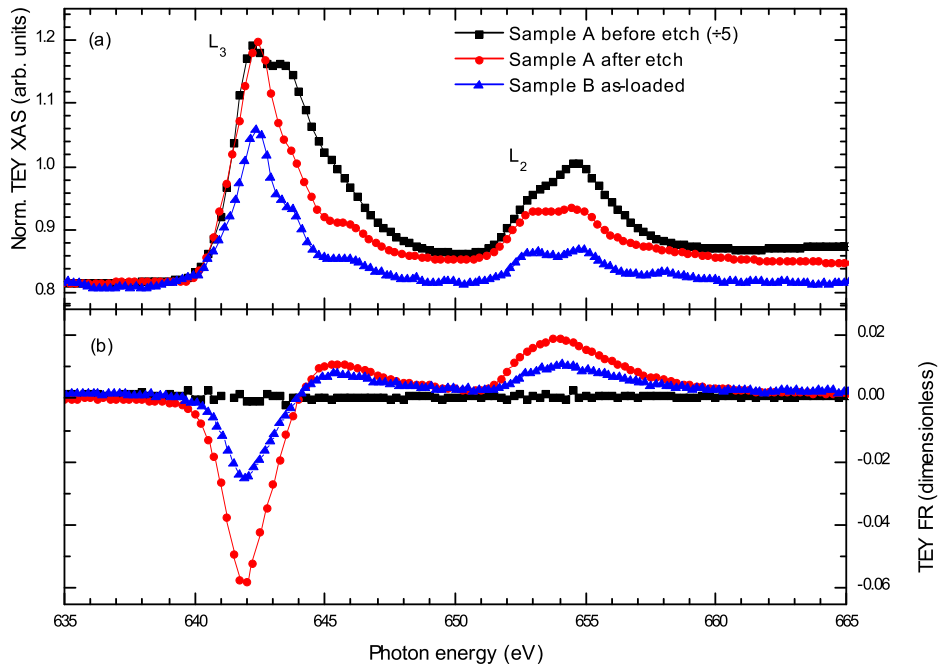
Figure 5.3: *Drain current XAS and FR data for samples* A *and* B*. The fine structure in both the* L_3 *and* L_2 *edges is seen in other high spin manganese systems where the moment is localised on the atomic site.*

structures, such as NiMnSb [108] and various manganese surface alloys [109, 110], where the manganese atoms are in a high spin state and the moment is localised on the atomic site. This picture is consistent with the original calculations of Coehoorn, Haas and de Groot [13]. The TEY FR (Fig. 5.3(b)) shows a strong dichroism signal after the etch where one had not been present beforehand. This indicates a non-magnetic layer, assumed to be Mn-oxides, has been removed by the HCl etch. The TEY XAS and FR data for sample *B* lacks the high energy features associated with Mn-oxides and has the same overall structure as sample *A* after etching. This indicates the Sb-cap has prevented oxidation of the surface but is sufficiently thin for the Mn signal to be detected. It should be noted that the change in TEY FR intensity between sample *A* etched and sample *B* is simply related to the Sb cap; photoemission of Sb 3d electrons will contribute to the total drain current but will have no spin dependence.
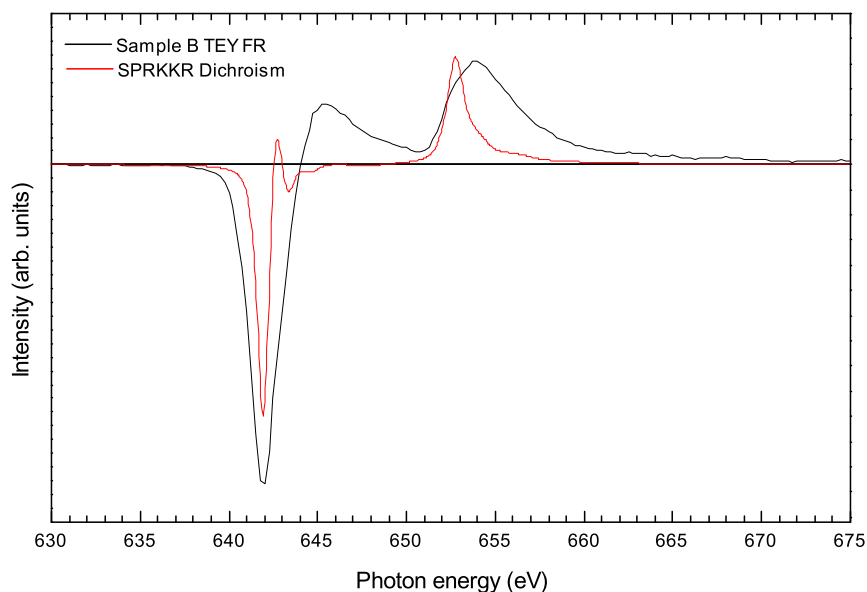
Figure 5.4: *Field averaged TEY FR data for sample* B *and predicted XMCD spectrum for MnSb(0001) bulk given by KKR calculations.*

A crude estimate can be made of the Mn-oxide layer thickness from the data in Fig. 5.3. The TEY signal is simply a sample drain current which is proportional to the number of Auger electrons which escape the surface and enter the vacuum which in turn is proportional to the transition rate from core $2p$ to valence $3d$ electronic states. Using the IMFP program by NIST [111] a 650 eV electron in MnO has a mean free path of approximately 2.0 nm. Under the assumption that 95% of an Auger signal comes from a depth of 3 IMFPs the MnO layer must be approximately 6 nm thick. This is a very thick oxide layer and represents $\geq 10\%$ of the total film thickness for this sample.

Detailed analysis of these TEY FR data to obtain information on the underlying electronic properties is prohibitively complicated with MnSb. The sum rule analysis, which works for simple ferromagnets such as nickel and iron, is known to breakdown with manganese. The reason for this is a strong $2p$–$3d$ Coulomb interaction which acts to mix the $j = 1/2$ and $j = 3/2$ states [112], which breaks the initial assumptions of the sum rule analysis. This is a well known phenomenon for some $3d$ transition metal elements where the spin-orbit interaction is of the same order as the exchange splitting

and is seen, for instance, with manganese, vanadium and chromium [76, 113].

However, an attempt to correlate these experimental results with theoretical calculations of the bulk was made using the SPRKKR DFT code [114]. The correct DOS and magnetic moment per manganese atom was found in these calculations, but as seen in Fig. 5.4, the agreement between the theoretical XMCD and experimental TEY FR is poor. In the first instance, the calculated separation between the L_3 and L_2 edges is smaller than the experimental value obtained in this work. Secondly, whilst the KKR calculations gets the magnetic moment per manganese atom correct, it aligns the spins parallel to the c-axis, which is contrary to previous calculations and experimental observations [101, 103]. Unfortunately the precise details of the calculation are not known. Specifically, it is unclear how accurately the calculation deals with the spin-orbit interaction of the $3d$ states, the interaction between the core-hole and excited $3d$ electron, the spin-orbit interaction of the core-hole and "diffuse magnetism" involving s electrons [76]. All of these factors are known to be important to a larger or lesser degree in other magnetic systems [70, 115, 116] which suggests a more detailed theoretical investigation is required.

Hysteresis loops for sample A taken using the XRMS and TEY methods are presented in Fig. 5.5. The hysteresis loops are determined by measuring the dependency of the FR at a constant photon energy of 642 eV as a function of applied field. This energy is chosen as it gives rise to a large dichroic signal but is below the resonant absorption edge. As expected, sample A before HCl etching shows no hysteresis using the TEY methods as the surface displays no dichroism. However clear hysteresis is apparent in the XRMS measurements and indicates the bulk of the film is magnetic. After the etch hysteresis loops in the TEY and XRMS data demonstrates the whole of the film is in a ferromagnetic state. Of interest is H_c, which changes from 64 Oe before the etch to 39 Oe afterwards. It has already been noted that the Mn-oxide layer represents up to 10% of the total film thickness. The change in H_c may then simply be due to the removal of antiferromagnetic MnO. AFM-FM coupling is a local
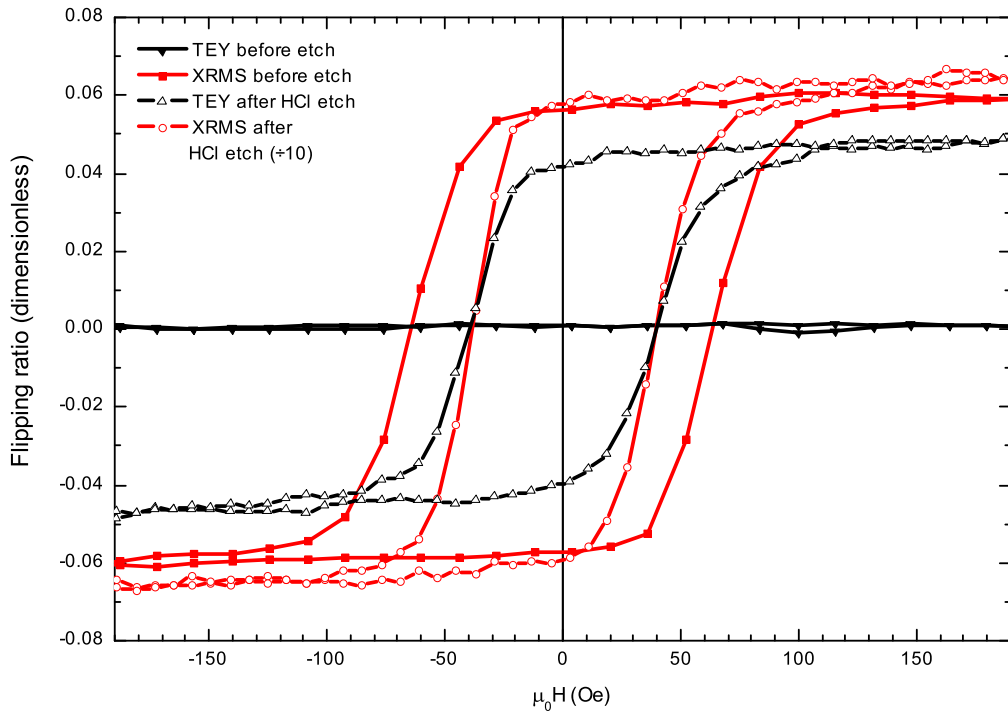
Figure 5.5: *Drain current and XRMS FR hysteresis loops taken with a photon energy $h\nu = 642$ eV. Before acid etching no hysteresis is seen in the TEY. The clear hysteresis in the XRMS demonstrates the bulk of the thin film. Hysteresis is seen in both the TEY and XRMS in sample B and indicates the whole film is in a ferromagnetic state. The change in the XRMS H_c is possibly related to the loss of antiferromagnetic Mn-oxides locally pinning the ferromagnetic moment in random directions.*

phenomenon but the MnO layer has not been set in a magnetic field so the local AFM spin arrangement is essentially random. This means local ferromagnetic moments at the MnSb/MnO interface are antiferromagnetically pinned in a random orientation with the overall effect being a widening of the hysteresis curve [117].

As a final comment the depth sensitivity of the two different XMCD techniques was briefly discussed elsewhere, but essentially the TEY probing depth is governed by inelastic electron scattering events. For MnSb a 650 eV electron has an IMFP of ~5 nm which equates to between 8 and 9 unit cells. The detected TEY signal shows clear dichroism but it is not clear from this technique if the final one or two atomic layers themselves carry a magnetic moment. To elucidate this point spin-polarised low energy electron microscopy (SPLEEM) experiments on MnSb thin films grown at Warwick have
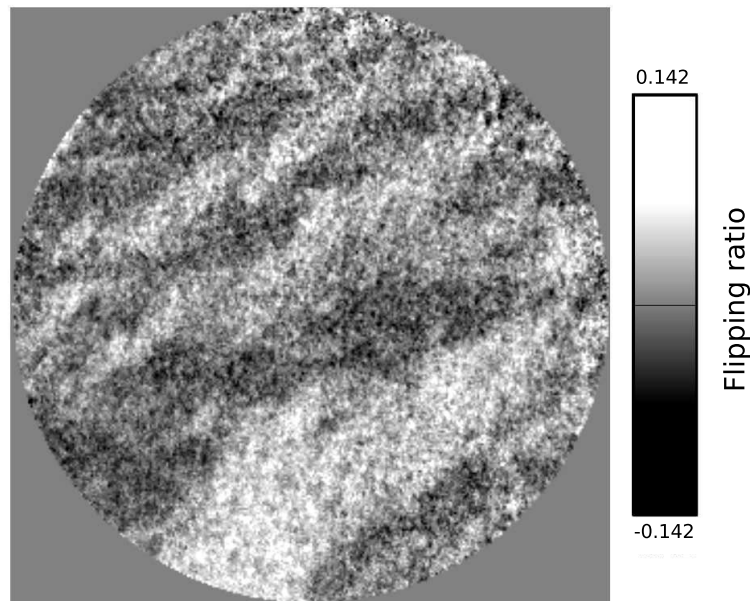
Figure 5.6: *Magnetic contrast in a SPLEEM image of MnSb sample after exposure to atmosphere and reprepared using the method given in Sec. 4.2. The clear magnetic contrast indicates the top few atomic layers possesses a magnetic moment.*

been performed at the National Centre for Electron Microscopy, Berkeley, California. In these experiments, spin-polarised electrons with an incident kinetic energy of 6.5 eV guarantees the detected signal originates from the top few atomic layers. Magnetic contrast is obtained by taking two images with the incident electron polarisation vector of one image rotated $180°$ relative to the other and defining a flipping ratio $(I_1 - I_2)/I_1 + I_2$), as in XMCD. The magnetic contrast seen in Fig. 5.6 was from an air-exposed MnSb(0001) thin films which had been prepared according to the treatment recipe discussed in Sec. 4.2 and showed the (2×2) surface reconstruction. This indicates that the final two atomic layers of the (2×2) surface reconstruction are magnetic and that the MnSb thin film needs to be clean and well ordered before a net ferromagnetic moment is obtained [118].

5.3 Conclusion

Bulk magnetometry experiments on MnSb(0001) epilayers confirms the manganese magnetic moment is comparable to previous published results. The thin films have uniaxial magnetisation with the c direction being the hard axis and the magnetic moments lying in the basal plane. This is consistent with previous experimental and theoretical investigations of the MnSb bulk magnetic properties. The Curie temperature for thicker MnSb films has been determined as 590 K, in agreement with previous studies. No magnetic ordering was found after cooling a thinner sample down from 700 K. It is believed that the sample has decomposed at these elevated temperatures, resulting in a loss of crystal structure and magnetic ordering.

A non-magnetic surface layer has been seen on MnSb thin films which have been air-exposed. The thickness of this film is estimated to be at least 5 nm. A simple HCl etch procedure has been demonstrated to effectively remove this oxide contamination layer and results in a magnetic surface. Moreover, antimony capping MnSb epilayers has been shown to prevent oxidation of the underlying MnSb, as evidenced by the magnetic signal seen in TEY FR results. Attempts at correlating these data with theoretical calculations have failed, largely due to the failure of the *ab inition* code to fully and accurately determine the magnetic behaviour of bulk-like MnSb.

Chapter 6

Surface structure determination of MnSb(0001)-(2×2)

A number of surface reconstructions have been seen on the free (0001) surfaces of a variety of BPs, such as MnAs, NiSb (reported in this thesis) and MnSb. The first reported surface reconstruction in this class of materials was the MnAs (2×2) in 2002 [119]. In the intervening decade, a very limited number of quantitative surface structure studies have been carried out on the MnAs(0001) (2×2) and td(1×4) surface reconstructions [85, 119, 120]. From these studies, the td(1×4) is believed to consist of long chains of arsenic atoms. However, analysis of the (2×2) data was more ambiguous, with three different structural models being proposed, namely an adatom, a missing atom model based on the GaAs(111)A-(2×2) [121] and a trimer model based on the GaAs(111)B-(2×2) [122]. To date, no reports exist in the literature relating to quantitative structure determination methods having been applied to any other BP, including MnSb.

One of the key difficulties with structure determination of the BPs is that there are no heuristics for solving their surface structures. For most III-V compounds, the well known electron counting rules can be applied to aid in the structure determination of the wide range of surface reconstructions observed on their free surfaces [30]. Elemental transition metals generally do not reconstruct as much as the III-V semiconductors largely due to the omnidirectional nature of metallic bonding. Of the free metal surfaces which do show reconstruction, e.g. Au(111), and of adsorbate-induced reconstruction, surface stresses are known to play a vital role [123, 124, 125, 126]. The BPs, being neither III-V semiconductors nor elemental metals, are not expected to be subject solely to either set of

rules. As such, solving the MnSb(0001)-(2×2) will be a crucial step in the development of a set of heuristics for solving the structures of BP surface reconstructions.

6.1 Proposed models

In this work, four main basic models have been considered: adatom, trimer, missing atom and mixed termination [82]. These models are shown schematically in Fig. 6.1(a), (b), (c) and (d). Models (a) and (c) are based on those proposed for the MnAs(0001)-(2×2) reconstruction by Ouerghi *et al.* [85, 120]. Model (b) is based on a structural model proposed by Kästner *et al.* [119], also for the MnAs-(2×2) surface reconstruction, whilst (d) was proposed by Hatfield and Bell [82]. In Fig. 6.1, the dashed red line denotes the (2×2) surface mesh, the open circles denote the final bulk-like atomic layer whilst green and blue circles denote "surface layer" atoms. Neither the blue nor green circles relate specifically to either manganese or antimony, but the surface layer consists of both antimony and manganese when both colours are present in a model. For each of the basic models, eight unique structures exist. This is in part due to the ABAC stacking order of MnSb shown in Fig. 6.1(h). For a manganese-terminated bulk with a final stacking order of ABAC, the surface layer atoms can sit in either B or C sites, henceforward denoted as hcp and fcc hollow sites respectively. Also, for an antimony terminated bulk with a stacking order of BACA, the surface layer atoms can sit in either A or C sites, again denoted as hcp or fcc hollow sites. No assumptions have been made *a priori* as to whether the bulk is manganese or antimony terminated. Moreover, no assumptions have been made of the chemical composition of the surface layer, e.g. the adatom in model (a) could be either manganese or antimony. Thus, for each model there are two possible bulk terminations, two surface layer compositions and two surface layer sites, resulting in eight unique structures per basic model.

Extensions to these basic models have been proposed and trialled in the LEED I-V study. Some of these extensions are depicted in Fig. 6.1(e), (f) and (g). In these extensions, some of the surface layer atoms are substituted for the other atomic species,
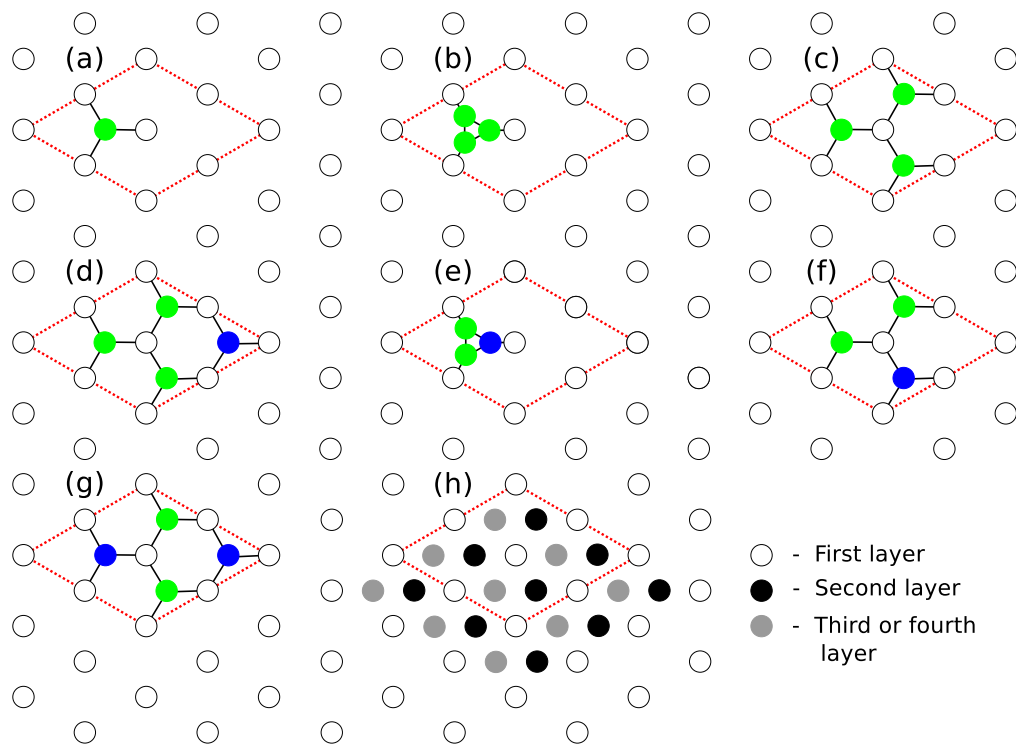
Figure 6.1: *Surface structure models for the MnSb(0001)-(2×2) surface reconstruc-
tion. The basic structural models are: (a) adatom, (b) trimer, (c) missing atom, (d)
mixed termination, (e) mixed trimer, (f) missing atom mixed termination and (g) stoi-
chiometric surface. In these models open circles denote the final bulk-like layer, whilst
the coloured circles denote different surface layer atomic species, but neither colour
specifically represents either manganese or antimony. (h) Generalised (0001) projection
of the MnSb bulk. The final layer stacking can be either ABAC or BACA depending on
whether the bulk is Mn- or Sb-terminated.*

giving a "heterotrimer", a missing-atom mixed-termination and a stoichiometric surface

layer composed 1:1 Mn:Sb. In addition, a vacancy-buckling (VB) model based on the

proposed structure for the GaAs and InSb (111)A-(2×2) reconstructions has also been

simulated during the LEED I-V study. This model is essentially the result of a large

inward relaxation of the surface layer atoms in Fig. 6.1(c) to form a 2D composite

layer with the final "bulk-like" layer. As with the other models, no assumptions have

been made *a priori*, meaning there are again eight unique structures for each of these

extensions.

One final basic model which had not been previously proposed, is based on a
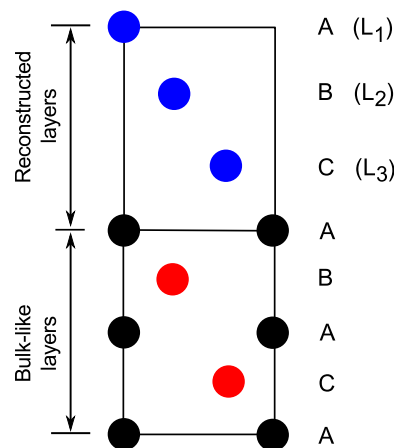
Figure 6.2: *An fcc-like surface structural model. Red and black circles represent respectively antimony and manganese atoms in their bulk-like positions. Blue circles represent "surface layer" atoms but does not relate specifically to either manganese or antimony.*

stacking rearrangement at the MnSb surface. In this model, shown in Fig. 6.2, the outermost MnSb layers re-order to give an fcc-like stacking arrangement in the final five atomic layers, i.e. ABCAB, with the separation between the final bulk-like manganese atom and L_1 set to be 5.789 Å. In the figure, black and red circles respectively denotes bulk-like manganese and antimony, whilst the blue circles represent surface layer atoms. For the purposes of this study, and for reasons which will become clearer in the following sections, this model was not made to be (2×2) in the simulations. Instead, L_1, L_2 and L_3 consisted of just one atomic species with all eight possible chemical permutations trialled in the CAICISS and LEED I-V simulations.

6.2 CAICISS results

CAICISS experiments were performed on an Sb-capped MnSb(0001) sample which was prepared according to the method detailed in Chap. 4. Fig. 6.3, taken after this preparation, shows the surface to be well ordered and (2×2) reconstructed.

Experimental data was acquired along the $<2\bar{1}\bar{1}0>$–$<\bar{2}110>$ ("0° azimuth") and $<1\bar{1}00>$–$<\bar{1}100>$ ("30° azimuth") high symmetry directions and is presented in
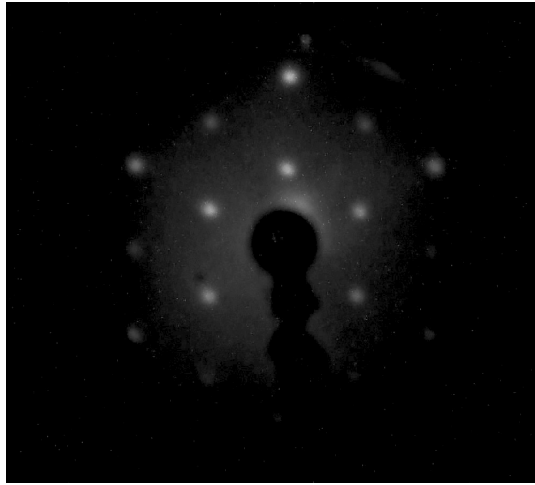
Figure 6.3: *LEED pattern of the Sb-capped MnSb(0001) sample after IBA. The pattern shows the surface to be (2×2) reconstructed and well ordered.*

Fig. 6.4. All of the collected data is presented in Apdx. B.

The first thing to note about these data is that it is approximately symmetric about $90°$, which is contrary to what is expected for a single domain MnSb(0001) surface. As discussed in Sec. 1.4, MnSb(0001) is strictly three-fold symmetric, so the $<2\bar{1}\bar{1}0>$ direction is inequivalent to the $<\bar{2}110>$. Thus, the data should not be symmetric about $90°$. However, terraces separated by $c/2$ steps are effectively rotated by $60°$ from one another. A surface covered with many such terraces would appear to have six-fold symmetry and is believed to be the case here. To account for this in the CAICISS simulations, simulated data is reflected about $\theta = 90°$ and averaged. Of much greater significance however, is the widths of the blocking dips in the manganese and antimony data about $90°$ are approximately equal. The width of the dip at $90°$ is related entirely to the spacing between two equivalent layers with larger separations giving narrower dips. In MnSb, this spacing is $c/2$ for manganese and c for antimony. Thus, the width of the $90°$ blocking feature in the manganese data is expected to be much wider than that in the antimony data, which is evidently not the case.
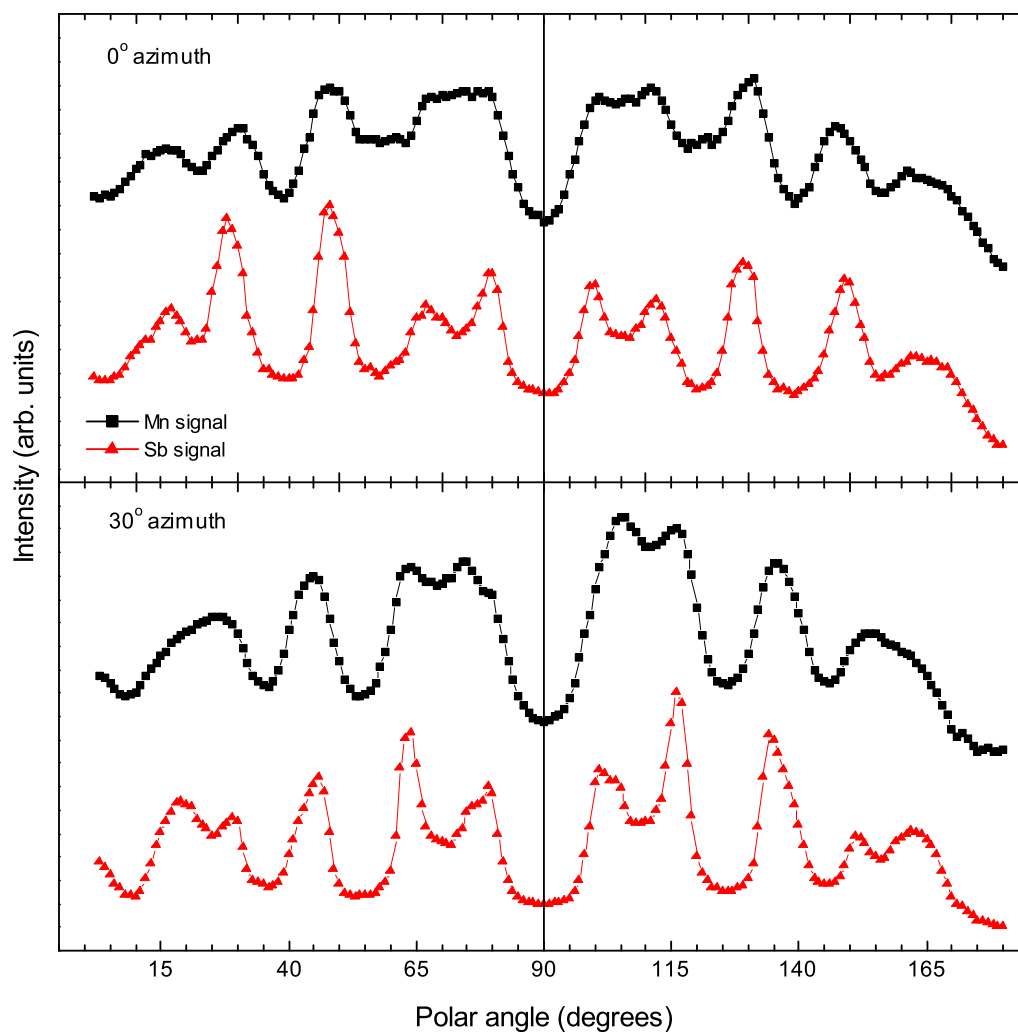
Figure 6.4: *Experimental CAICISS data along the two high symmetry azimuthal directions described in the test for the MnSb(0001)-(2×2). Black squares are manganese yields while red triangles are the antimony yields.*

Simulation results

Simulations were performed for the eight unique structures for each of the four basic models (a), (b), (c) and (d). The first thing to note is there are very few variations in the simulated data between the different models. Some obvious subtleties in some of the simulations are enough to instantly reject, for instance, the adatom and trimer models, but otherwise there are no major features which obviously distinguishes one model from

the next. The second thing to note is the $90°$ dip in the manganese yield in all of the simulations was considerably wider than in the antimony yield, which is expected for the niccolite bulk-stacking arrangement. Thirdly, the agreement between the simulated and experimental manganese signals is universally poor across all of the models, whilst the simulated antimony does fit the experimental data to a reasonable degree of accuracy for some of the models. On the basis of these observations, the models with the best CAICISS fits are as follows:

- Manganese terminated bulk

    - Mixed termination, 3:1 Sb:Mn, hcp site

    - Mixed termination, 1:3, Sb:Mn, hcp site

- Antimony terminated bulk

    - Missing manganese atom, fcc site

    - Mixed termination, 3:1 Sb:Mn, fcc site

    - Mixed termination, 1:3, Sb:Mn, fcc site

For these models, the simulated antimony data displays reasonable agreement with the experimental data in both of the experimental azimuths. For the other models, one or both of the antimony yields has a much poorer fit, either with extra or missing features. In the interests of brevity, only the simulated data from the above listed models is reproduced in Fig. 6.5. The complete set of data can be found in Appendix B.

As discussed earlier in this section, the separation between atoms in equivalent layers dictates the width of the blocking feature at $90°$. The width of this dip in both the manganese and antimony yields is approximately equal, suggesting the layer separation between equivalent manganese and antimony atoms is about the same. On this basis, the fcc-like structural model shown in Fig. 6.2 was proposed. In this structure, the separation between L_1 and the last bulk-like manganese layer is chosen to be c (5.789 Å), with the L_1–L_2 and L_2–L_3 separations being $c/3$. For the purposes of this
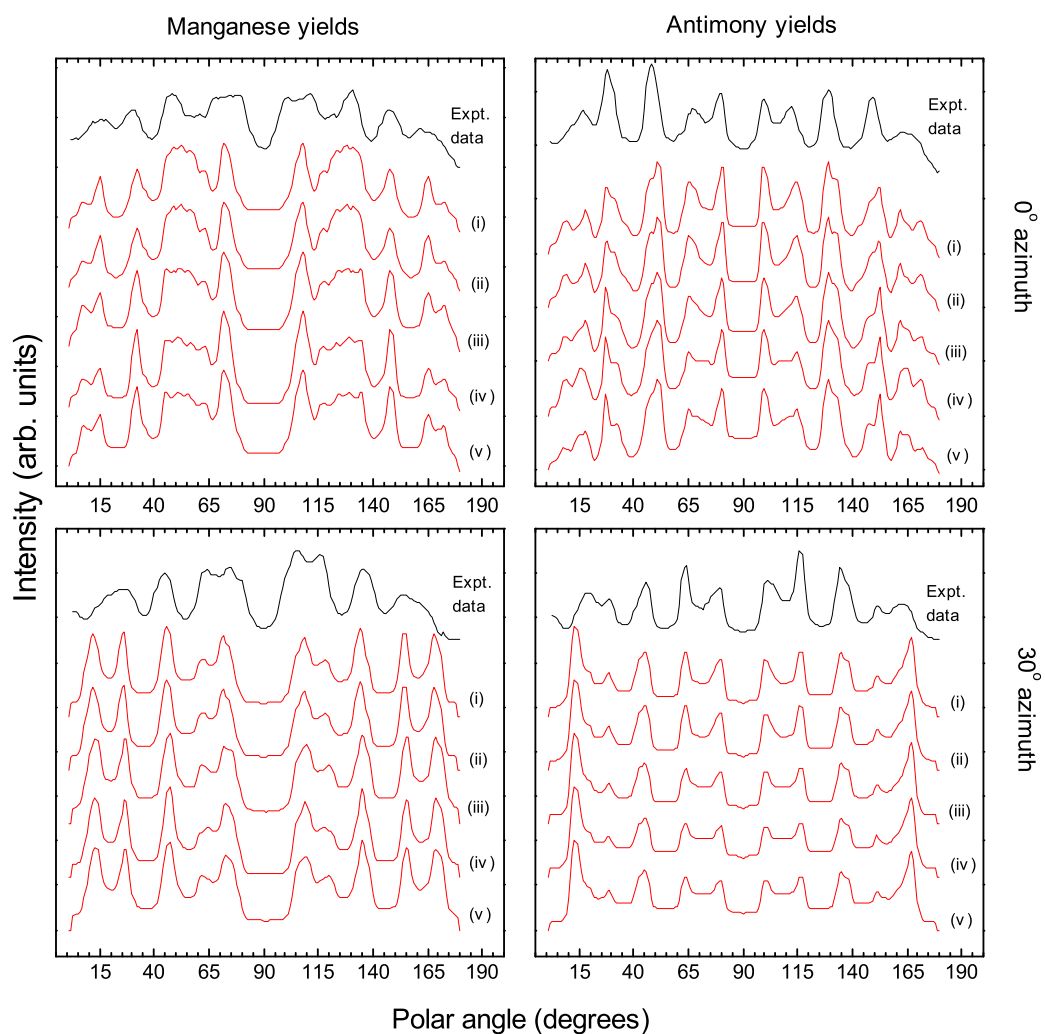
Figure 6.5: *Experimental manganese and antimony signals (black lines) along the two high symmetry azimuthal angles discussed in the text along with selected simulated data. (i) Missing Sb atom in hcp sites (ii) missing Sb atom in fcc sites. Both (i) and (ii) we bulk-terminated with manganese. (iii) Missing Mn atom in fcc sites (iv) 3:1 Sb:Mn mixed termination in fcc sites (v) 1:3 Sb:Mn mixed termination in fcc sites. These last three were bulk-terminated with antimony.*

work, only simulations of (1×1) surfaces along the $0°$ azimuth have been made. All possible atomic compositions of $L_1L_2L_3$ have been simulated, e.g. MnMnMn, MnMnSb, etc. The simulated data for these eight structures is given in Fig. 6.6. It is immediately apparent that the change in crystal structure has worsened the overall fit of the antimony data, as additional peaks appear at $\sim 40°$ and $\sim 140°$. Also, of particular interest, is
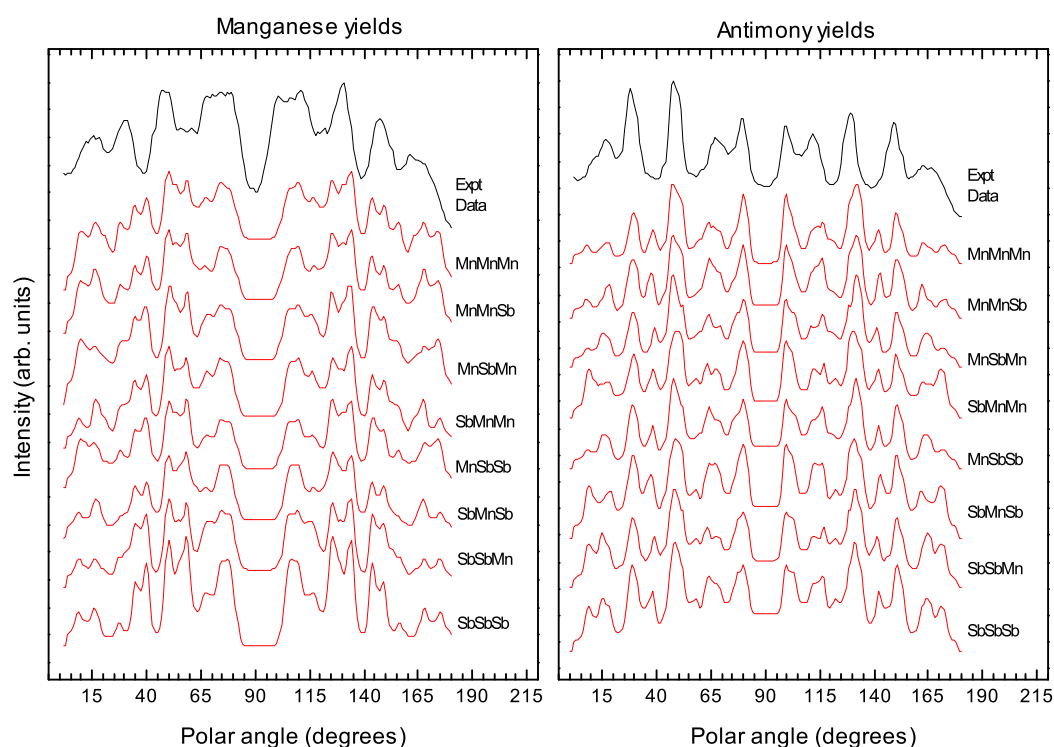
Figure 6.6: *Simulated data along the 0° azimuth for the eight possible chemical compositions of the fcc-like surface model. The chemical composition for $L_1 L_2 L_3$ is given by each dataset. The experimental data (black line) is for comparison.*

the manganese blocking dip at 90°, which is still wider than the corresponding antimony one, even with approximately equivalent layer separations.

6.3 LEED I-V results

Uncapped MnSb(0001) samples were transported in air without any special precaution and prepared using a combination of acid etching and *in situ* Ar^+ ion bombarding and gentle annealing, in accordance with the procedures discussed in Sec. 4.2. A typical (2×2) LEED image after surface preparation is given in Fig. 6.7. LEED I-V data was acquired using a computer operated control box and digital camera between 30 and 290 eV, with images taken in 1 eV increments. Extraction of the LEED I-V curves was done using the program multLEED [127]. Diffraction spots were highlighted manually and tracked by the software. Spot intensities were determined by integrating the intensity
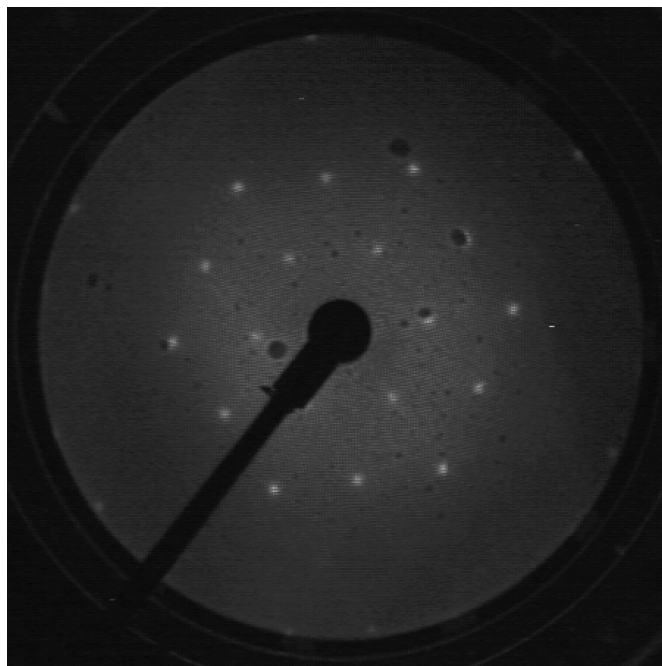
Figure 6.7: *LEED image at 60 eV of an antimony capped MnSb(0001) sample showing the (2×2) reconstruction after* in situ*preparation.*

of the diffraction spot within a square box and subtracting a background determined by a total of 36 pixels located at the corners of the boxes. Multiple LEED I-V curves corresponding to symmetrically equivalent diffraction spots were averaged to remove small fluctuations and to account for sensitivity inhomogeneities of the LEED screen.

Immediate inspection of the raw LEED images reveal a surface which is six-fold symmetric, which follows the behaviour seen in the CAICISS data. This six-fold symmetry is easily seen through the experimental LEED I-V curves shown in Fig. 6.8(a)–(e), where diffraction spots which should be inequivalent, e.g. (1, 0) and (0, 1) are identical. By symmetry, the diffraction spots shown in panels (c) and (e) should be equivalent. Fig. 6.8(f) shows the combined experimental spot averages, which were used in the CLEED r-factor calculations.

As before, the origin of this apparent six-fold symmetry is believed to be due to $c/2$ steps at the surface. Accounting for this is straightforward using the CLEED package. The diffraction pattern obtained from a surface with a local stacking order
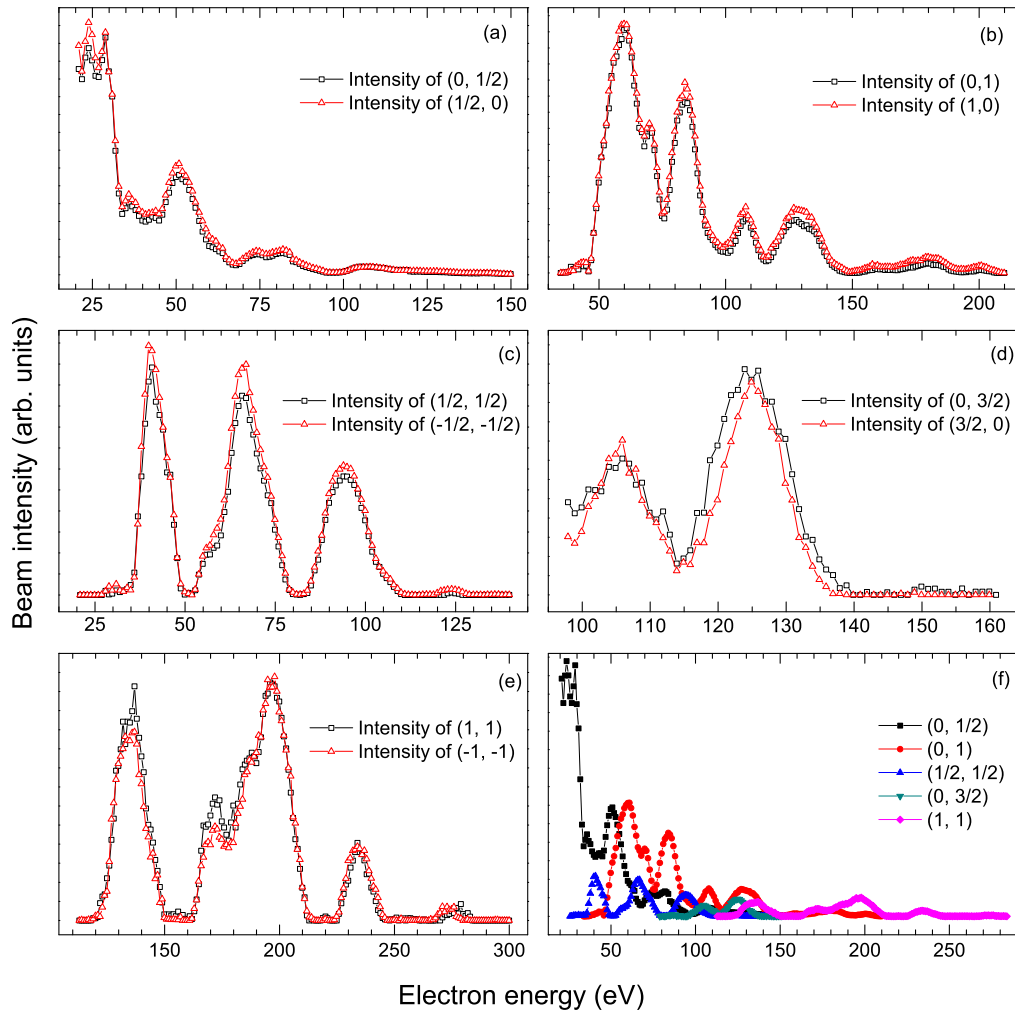
Figure 6.8: *Experimental LEED I-V curves for MnSb(0001)-(2×2). Due to the symmetry of the crystal, the diffraction spots shown in panels (a), (b) and (d) should be inequivalent. Similarly, the spots shown in (c) and (e) should be equivalent. The data in (f) are the combined diffraction spot averages used in the theoretical simulations.*

of ABAC is rotated by 60° relative to a surface terminated ACAB, meaning the (0,1) spot for ABAC is equivalent to the (1,0) spot of an ACAB surface. To check that this behaviour is seen in theoretical calculations, CLEED simulations were performed using a manganese adatom model, where the adatom was located in the fcc and hcp hollow sites on ABAC and ACAB terminated bulk crystals. The simulated LEED intensities, given in Fig. 6.9 show the expected equivalency between the (1,0) and (0,1) diffraction
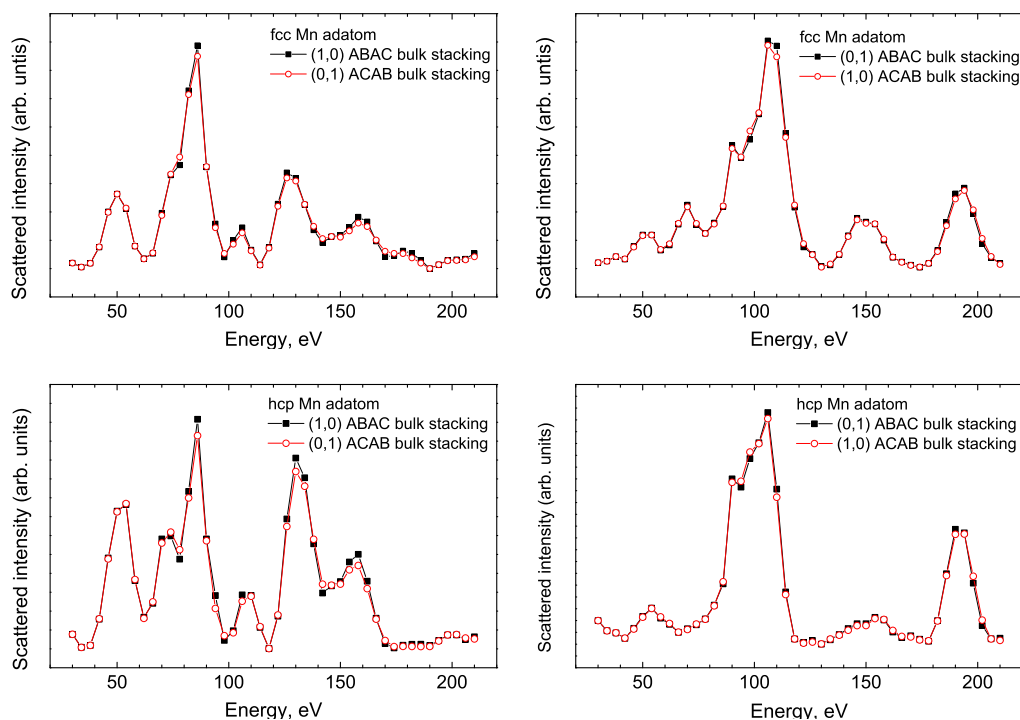
Figure 6.9: *Simulated LEED I-V curves for a manganese adatom in an fcc hollow site (top panels) and hcp hollow site (bottom panels) for two different surface stacking arrangements - ABAC and ACAB - of a manganese terminated bulk. As expected, the LEED I-V intensity of the (1,0) spot for one surface is equivalent to the (0,1) intensity for the other domain.*

spots for two surfaces effectively rotated by 60°. Thus, to account for the two-domain surface, the *crfac* code averages all beams of the same order, e.g. (0,1) and (1,0), before comparing to the corresponding experimental data.

Simulation results

All of the models discussed in Sec. 6.1 have been simulated using the *cleed* package. The "overlayer" file used for all of the trial models had at least four bulk-like layers in addition to the reconstructed surface layer. This allowed the CLEED package to move "bulk-like" layers as part of the parameter search and structural optimisation. Example input files used in these simulations can be found in Apdx. C.

As briefly discussed in Sec. 2.2.2, restrictions can be placed on the atomic displacements that the *csearch* program makes during structural optimisation. In this work, only a z-search was conducted, where entire layers of atoms are allowed to displace vertically with all in-plane displacements forbidden. The reason is based purely on speed, as 68 unique structures were trialled and computational time scales as the cube of the number of search parameters. Also, the calculations were performed with 4 eV steps. The reason for this is again one of speed, due to the large number of structures which were trialled. However, for this study, a 4 eV step size is sufficient. The peak widths in a LEED I-V curve will have a width approximately equal to the imaginary component of the inner potential, which is approximately 4 eV [57, 56], so no features will be missed by the simulation. Moreover, the parameter of interest in this LEED I-V study is the Pendry r-factor, R_P, which is calculated within the *crfac* program. As noted previously, R_P is predominantly sensitive to peak positions and not peak intensities, except when peaks overlap where relative intensities between the overlapping peaks are taken into consideration. An r-factor value of zero (one) denotes perfect (no) correlation between the experimental and simulated data.

All of the structural models considered in this work had an initial R_P of approximately 0.87, with the best being 0.8 for a manganese trimer in an fcc site on a Mn-terminated bulk, and the worst being 1.0 for the manganese VB model in an fcc site, also on a Mn-terminated bulk. After optimisation, every model had a Pendry r-factor equal to or greater than 0.57. This signifies there is very little agreement between any of the trial structures and experimental data. A full summary of all of the r-factors calculated for all of these structural models is given in Apdx. D and Tab. D.1.

All of these r-factors are clearly unsatisfactory, with no one structure presenting itself as being any more valid over the rest. However, the picture can be improved by considering the error on R_P, which is calculated by the *crfac* code following the method detailed by Pendry [62]. For all of the models considered in this work, the error is approximately 10%. As such, only models with an r-factor below 0.63 will be considered

here onwards. The models which satisfy this criterion are:

- Mn-terminated bulk

  - Mn trimer in hcp site ($R_P = 0.59$) (model (i))

- Sb-terminated bulk

  - Mixed missing atom, 1:2 Sb:Mn in hcp site ($R_P = 0.57$) (model (ii))

  - Mixed termination, 1:3 Sb:Mn in hcp site ($R_P = 0.58$) (model (iii))

  - Stoichiometric surface layer in hcp site ($R_P = 0.59$) (model (iv))

  - Mixed missing atom, 2:1 Sb:Mn in hcp site ($R_P = 0.59$) (model (v))

  - Mixed missing atom, 1:2 Sb:Mn in fcc site ($R_P = 0.62$) (model (vi))

  - Mixed missing atom, 2:1 Sb:Mn in fcc site ($R_P = 0.62$) (model (vii))

The experimental data for all six of these models is given in Fig. 6.10. Ignoring the values of R_P, there does appear to be a few trends of note. Firstly, the LEED simulations seem to favour a bulk crystal terminated with antimony. This is consistent with our RHEED observations, as the (2×2) is obtained by deposition of manganese onto a (1×1) surface, which is believed to be an antimony terminated bulk crystal. Secondly, the LEED I-V simulations appear to broadly favour the surface layer in a hcp site. Thirdly, the mixed missing atom model, corresponding to a mixed surface layer with one atomic vacancy per (2×2) unit mesh, all have R_P's within the limits considered, with the manganese rich surface in a hcp site having the smallest r-factor out of all the models considered. It is encouraging that one specific model gives universally low r-factors, with the most manganese rich surfaces being favoured over the antimony rich ones. Of course it must still be noted that the r-factors are poor and in light of the CAICISS data these models are unlikely to be correct. However, the chemical trends match what is expected and may provide further clues in conjunction with other techniques.
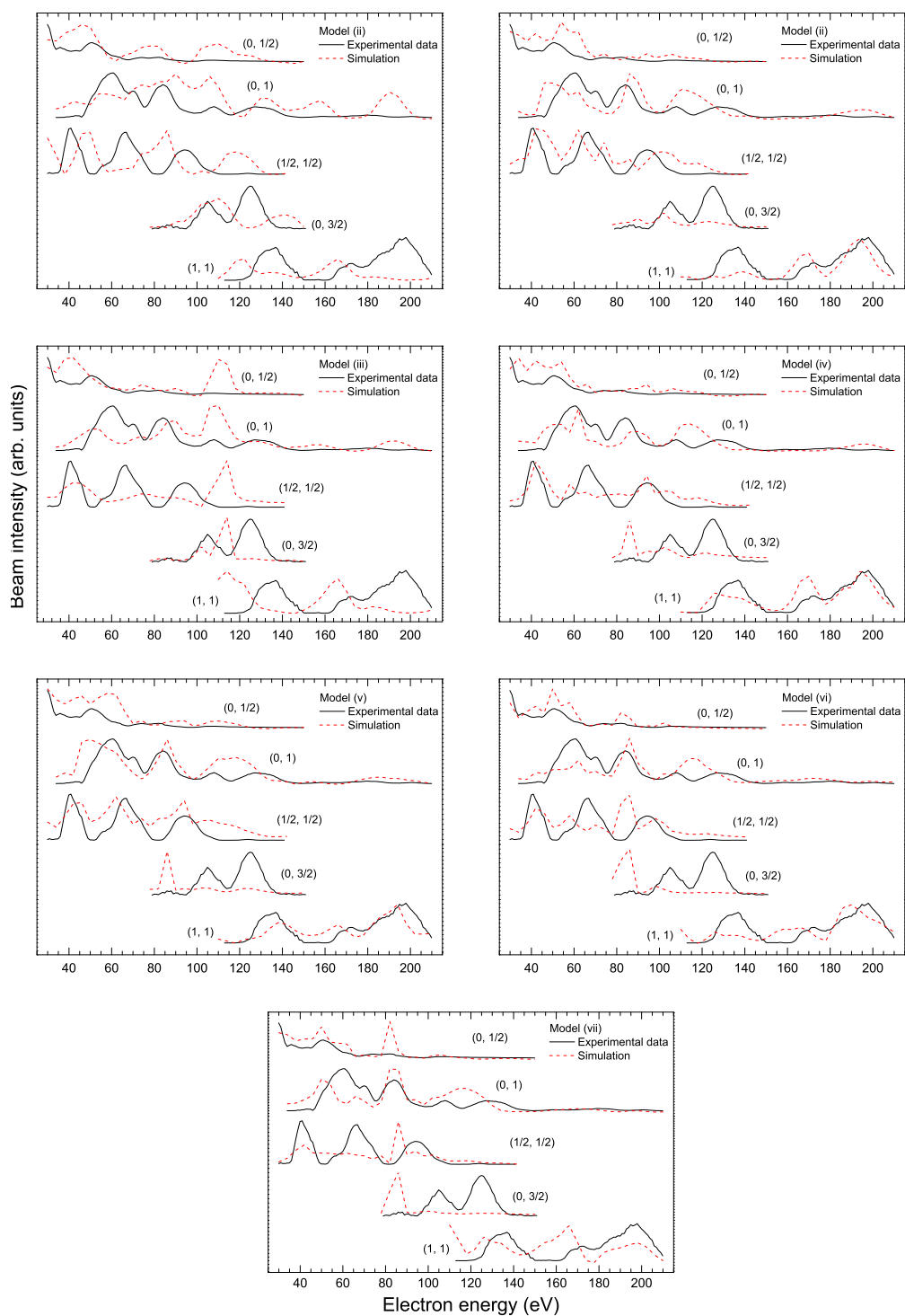
Figure 6.10: *Simulated LEED I-V curves for the seven best models described in the text.*

6.4 Summary

To summarise, quantitative structure determination has been done on the MnSb(0001)-(2×2) surface using a combination of low energy ion scattering and LEED I-V. In total, 68 different structural models have been trialled. Some of these models were based on III-V-like reconstructions proposed for the MnAs-(2×2), whilst others have been proposed during this work. None of these models adequately fit either or both of the techniques used with all of the models ruled out by either the CAICISS or LEED I-V simulations. However, some important observations have been made.

The LEED I-V data analysis suggests that the bulk is antimony terminated with a surface layer in a hcp site and composed mostly of manganese. This is entirely consistent with our RHEED observations, where manganese is deposited on the (1×1) to get the (2×2) reconstruction and antimony on a (2×2) surface to regain the (1×1). However, all LEED I-V r-factors for all models considered in this work are universally poor, whilst the best models are rejected by the CAICISS simulations.

From the CAICISS data analysis, no similar chemical trends are readily apparent, with the exception that a near complete surface layer is preferred over the incomplete surface layer and trimer models. No bulk-termination is especially preferable, but the hcp site would appear to be preferable over the fcc site on the manganese terminated bulk and the fcc sites more preferable on the antimony terminated bulk. This last point seems to contradict the LEED I-V results.

Despite these issues, two important points must be noted. Firstly, both the CAICISS and LEED I-V data suggests the surface is six-fold, symmetric. This is in direct contradiction to the bulk-stacking arrangement of the BPs which is strictly only three-fold symmetric. It was believed that this apparent six-fold symmetry was due to terraces separated by $c/2$ steps and rotated by 60° relative to each other, giving the apparent six-fold symmetry. However, the second important result to note is the blocking dip at 90° in the CAICISS data. Given the bulk-stacking arrangement, this blocking dip

should be much larger in the manganese yields than in the antimony yields, which is not seen in the experimental data, with the width of both dips being approximately equal. The width of this blocking feature is governed only by the interlayer separation of the same atomic species, which in MnSb is $c/2$ for manganese and c for antimony. Given this, a more significant structural change may take place in the near surface region, with the (2×2) surface being composed of several reconstructed layers and possibly have genuine six-fold symmetry. This would be unusual, but such a radical change in the crystal structure would have profound implications for the surface electronic and magnetic properties, which may differ substantially from the bulk, as well as for epitaxial growth of MnSb acting as the substrate. Moreover, such a dramatic change in structure may be a precursor to the formation of the cubic or wurtzite MnSb crystallites seen within these films.

Chapter 7

Conclusions and Further Work

7.1 Summary

To conclude, a multi-technique study of MnSb(0001) and NiSb(0001) thin films has been conducted to elucidate on their surface structures, bulk structures and magnetic properties. The first experimental chapter was concerned with the growth of NiSb(0001) on GaAs(111)B, and is the first study of its kind. A combination of RHEED and XRD has shown the thin films to be highly crystalline, although the origins of some additional, unindexed peaks remains an outstanding question. From the RHEED observations made during the growth, NiSb(0001) has been seen to reconstruct, with three different diffraction patterns being observed, although one of these, namely the (4×6), is only metastable. The td(1×3) is believed to be strongly related to similar reconstructions seen on MnSb and MnAs, i.e. chains of antimony on the surface. The second reconstruction has been initially labelled as a "(4×4)" and is potentially entirely new to the class of binary pnictides. That is, a (4×4) reconstruction has not been reported for MnAs or MnSb, but it is possible this NiSb structure is formed from two different (2×2) motifs arranged in a way to give the apparent (4×4) periodicity.

The MnSb(0001) growth procedure used in Hatfield's work has been modified and updated with a new antimony capping procedure being introduced. This antimony cap has been shown through the use of XMCD to prevent significant oxidation to the MnSb(0001) surfaces even after prolonged exposure to atmospheric conditions. Moreover, these XMCD results show a native Mn-oxide layer on uncapped MnSb(0001) films is non-magnetic and sufficiently thick to prevent a magnetic signal from the underlying

MnSb bulk to be observed using the TEY method.

A J dependent MnSb(0001) growth study shows a series of interesting results. Firstly, in the XRD data a number of additional reflections have been seen. Some of these reflections may be the result of multiple scattering but it is not possible from the results obtained if that is the case. Secondly, and of greater importance, is the observation of cubic MnSb(111) crystallites in at least two different strained states within some of these thin films. This is an intriguing result with no similar data in the published literature. However, it is not entirely clear from this study what prompts the growth of these crystallites, but from the work presented here, the beam flux ratio may be a contributory factor. This cannot, however, be confirmed unequivocally from the obtained data. For historical reasons, the manganese effusion cell is recessed in a feedthrough further away from the sample manipulator than the antimony cell, which essentially leads to a greater collimation of the molecular beam and a gradient in J across the sample of up to 10%. The evidence gathered to date and presented in this thesis would suggest the final film structure and morphology very sensitively depends upon J. In all likelihood, the x-ray beam for some XRD data was aligned parallel to the J gradient and others perpendicular to it which complicates the matter of extracting a trend.

Magnetic characterisation techniques have been applied to a variety of MnSb thin films. Bulk magnetometry shows the magnetisation is uniaxial, with the c direction being the hard axis. The magnetisation is found to lie entirely in-plane, with VSM giving a very low coercive field value of approximately 15 Oe. Magnetisation versus temperature results on thicker MnSb films show the Curie temperature of these films to be 590 K. In contrast, very thin films are seen to thermally decompose resulting in a loss of structural and magnetic ordering, when left at elevated temperatures for a prolonged period of time. Moreover, XMCD measurements on MnSb thin films show the surfaces of air-exposed samples to be non-magnetic. Magnetic ordering can be achieved on such samples through acid etching. Alternatively, antimony capping has been demonstrated

as being effective at preventing the formation of a thick non-magnetic Mn-oxide layer. Of potential significance is the reduction in coercive field of the bulk of the thin film after an uncapped sample is HCl etched. This has been attributed to the loss of antiferromagnetic Mn-oxides which pins locally the MnSb ferromagnetic moment.

Quantitative surface structure determination data acquired using LEED and CAICISS have proven to be extremely complex to interpret. Both techniques would appear to point towards a surface structure composed mostly of manganese on top of an antimony-terminated bulk but some doubt still remains. The r-factor determined in LEED for the very best model is 0.57 which signifies some considerable disagreement between the experimental data and simulation. Of the CAICISS data, the narrow blocking dip at 90° in the manganese yield appears to contradict the bulk stacking arrangement and all attempts at narrowing this dip in the simulations either destroys the correlation between the antimony simulated and experimental data or at best does little to improve the correlation between experiment and simulation for either the manganese or antimony signal. Two main possibilities exist for this disagreement. Firstly, polymorphs in the vicinity of the surface may contribute a signal to the experimental data but hasn't been taken care of in the models. Secondly it may be the models proposed are just wrong and that the real surface is a more complicated structure involving more atomic layers with larger lateral and vertical relaxations in combination with a total rearrangement of the stacking order. Such a structural change has profound implications for the surface electronic and magnetic properties. It is also possible that such a structural change encourages the formation of w-MnSb and c-MnSb.

7.2 Future work

There still exists a large number of unanswered questions surrounding the BPs and their potential spintronic applications. The initial growth study of NiSb undertaken during this work has proved to be highly promising, with high quality epitaxial thin films of MnSb being grown on GaAs(111)B substrates. However, the number of samples grown

to date is very limited. A much more detailed growth study and investigation is highly sought after. It is also necessary to determine whether the interface between the epitaxial thin film and the substrate is smooth and abrupt. For spintronics, such an interface is of vital importance. Moreover, it is necessary for NiSb to be compatible with a range of semiconductors and other BPs, e.g. CrSb and MnSb, if multilayers are to be grown with it. To date, no growth studies of either CrSb or NiSb multilayers is reported in the literature. As such, the growth and fine tuning of BP multilayer spintronic devices remains an open opportunity which should be explored.

It has been shown in this thesis that the growth of MnSb is highly sensitive on J. Indeed, the origins of both the cubic phase and the mesa morphology may result from small changes in the local J. To investigate this, a position-dependent XRD study should be conducted on samples which are both smooth and have mesas. It would also be worthwhile changing the working distance of the manganese cell, so that it matches the antimony. Doing this would reduce considerably the gradient in J across the substrate.

The surface structure determination work has proved to be extremely challenging. The results obtained indicate that the MnSb(0001)-(2×2)results from a significant change in the local structure, possibly resulting in a change from three-fold to six-fold symmetry. In order to confirm or deny this, it would be advantageous to use a number of other techniques. Firstly, high qualtiy, atomic resolution STM images across terrace steps would show conclusively whether there is a bond rotation of $60°$ or otherwise. Secondly, surface x-ray diffraction could prove to be an invaluable technique as: 1) different polymorphs will give rise to diffraction beams at different points in reciprocal space; and 2) more direct Fourier transform methods could be applied.

Appendix A

Predicted reflections for non-niccolite materials and phases

X-ray diffraction data from NiSb and MnSb thin films was presented in Chap. 3 and 4 respectively. In both of these studies several additional reflections which could not be indexed onto niccolite planes were evident. A number of possible materials and phases have been investigated as being the source of these reflections and are summarised here. Inexhaustive lists of predicted peak positions from these materials are given in Tables A.1 and A.2.

Firstly, Mn_2Sb, $MnSb_2$ and $NiSb_2$ were considered as possible candidates for some of the additional reflections. The latter two adopt the marcasite structure (space group Pnnm) [128, 129], with lattice parameters of $a = 6.017$ Å, $b = 6.881$ Å and $c = 3.32$ Å for $MnSb_2$ and $a = 5.19$ Å, $b = 6.33$ Å and $c = 3.84$ Å for $NiSb_2$. In contrast, Mn_2Sb adopts a tetragonal structure (space group P4/nmm) [130] with lattice parameters of $a = 4.078$ Å and $c = 6.557$ Å.

The lattice parameters of the zinc-blende (space group F$\bar{4}$3m) intermetallic (Ga,Mn)As and (Ga,Mn)Sb compounds can be estimated through Vegard's law using the lattice parameters of GaAs (5.6533 Å [92]), GaSb (6.0959 [131]), c-MnAs (5.7 Å [132, 133]) and c-MnSb (6.502 Å). On the basis of a manganese concentration of 5 at.% the lattice parameters of (Ga,Mn)As and (Ga,Mn)Sb are 5.656 Å and 6.11 Å respectively.

It is known that the surfaces of these thin films will oxidise, with experimental evidence suggesting a very thick Mn-oxide layer exists at the surfaces of MnSb. Both

NiO and MnO adopt the rocksalt structure (space group F$\bar{4}$3m) [134, 135] with room temperature lattice parameters of 4.177 Å and 4.448 Å respectively.

The cubic phase of NiSb (space group F$\bar{4}$3m) was investigated by David Pickup and Todd Humphries using the CASTEP DFT code to perform structure optimisation calculations on niccolite and cubic lattices [136]. Their calculations used ultrasoft pseudopotentials with an energy cutoff of 290 eV and were performed under the generalised gradient approximation, using the PBE exchange-correlation functional. All calculations were initiated with a non-zero spin-polarisation which was found to rapidly diminish to zero resulting in a paramagnetic groundstate for both structures. The final lattice parameters for n-NiSb were found to be a = 3.988 Å and c = 5.160 Å. The c-NiSb calculation ended with an equilibrium 0 K lattice constant of 5.74 Å.

In addition to the above mentioned compounds, elemental copper, aluminium, indium and antimony were considered as possible sources of the unknown reflections. The sample holders and attenuators used at X22C and in the Philips X'Pert diffractometers are composed of either copper or aluminium. Both elements crystallise in an fcc structure with lattice paramters of 3.6153 Å and 4.0496 Å for copper and aluminium respectively. Indium crystallises in a tetragonal lattice (space group I4/mmm) with lattice parameters a = 3.2523 Å and c = 4.9461 Å [137], whilst Sb crystallises in a trigonal lattice (space group R$\bar{3}$m) with lattice parameters a = 4.307 Å and c = 11.273 Å [137].

Table A.1: *Predicted Q_z peak positions in $Å^{-1}$ for Mn$_2$Sb, MnSb$_2$ and NiSb$_2$. Dashes indicate systematic extinctions. The list is not exhaustive.*

Lattice plane	Mn$_2$Sb	MnSb$_2$	NiSb$_2$
001	0.958	–	–
002	1.916	3.780	2.421
003	2.875	–	–
004	3.834	7.561	4.843
005	4.791	–	–
006	5.749	11.341	7.264
020		1.826	1.985
040		3.652	3.970
060		5.478	5.956
200		2.089	3.273
400		4.177	6.545
600		6.266	9.817
110	2.179	1.387	1.566
220	4.358	2.774	3.131
330	6.537	4.162	4.697
101	1.814	2.159	2.035
202	2.363	4.319	4.071
303	3.544	6.478	6.106
011		2.099	1.914
022		4.198	3.826
033		6.298	5.741
111	2.380	2.345	2.265
222	4.760	4.689	4.529
333	7.141	7.034	6.794

Table A.2: *Predicted Q_z peak positions in Å^{-1} for the range of materials described in the text. Dashes indicate systematic extinctions. The list is not exhaustive.*

Lattice plane	MnO	(Ga,Mn)As	(Ga,Mn)Sb	c-MnSb	w-MnSb	NiO	c-NiSb	Cu	Al	In	Sb
002	2.825	2.222	2.057	1.933		3.008	2.189	3.476	3.103	2.541	
004	5.650	4.444	4.113	3.865		6.017	4.379	6.952	6.206	5.081	
006	8.476	6.665	6.170	5.798		9.025	6.568	10.428	9.309	7.622	
110	–	–	–	–		–	–	–	–	2.732	2.918
220	3.995	3.142	2.909	2.733		4.255	3.096	4.916	4.388	5.464	5.835
330	–	–	–	–		–	–	–	–	8.196	8.753
440	7.991	6.284	5.817	5.466		8.509	6.192	9.831	8.777	10.928	11.671
101										2.312	1.774
202										4.624	3.549
303										6.936	5.323
111	2.447	1.924	1.781	1.674		2.606	1.896	3.010	2.687	–	
222	4.893	3.848	3.562	3.348		5.211	3.792	6.020	5.375	6.026	
333	7.340	5.777	5.343	5.021		7.817	5.688	9.031	8.062	–	
0002					1.794						
0004					3.588						
0006					5.383						
1100					1.691						
2̄200					3.382						
3̄300					5.073						
1̄101					1.914						
2̄202					3.828						
3̄303					5.742						

Appendix B

CAICISS simulation data

All of the CAICISS simulation results are collated here. In the following graphs, the first (black) line corresponds to the experimental data whilst the other labelled (red) lines correspond to:

(i) antimony adatom in fcc site

(ii) antimony adatom in hcp site

(iii) manganese adatom in fcc site

(iv) manganese adatom in hcp site

(v) antimony trimer in fcc site

(vi) antimony trimer in hcp site

(vii) manganese trimer in fcc site

(viii) manganese trimer in hcp site

(ix) missing antimony in fcc site

(x) missing antimony in hcp site

(xi) missing manganese in fcc site

(xii) missing manganese in hcp site

(xiii) mixed termination, 3:1 Sb:Mn in fcc site

(xiv) mixed termination, 3:1 Sb:Mn in hcp site

(xv) mixed termination, 1:3 Sb:Mn in fcc site

(xvi) mixed termination, 1:3 Sb:Mn in hcp site.

As in Section 6.2, the $0°$ azimuth corresponds to an incident geometry along $<2\bar{1}\bar{1}0>-<\bar{2}110>$ directions, while the $30°$ azimuth corresponds to $<1\bar{1}00>-<\bar{1}100>$.

Figure B.1: *Simulated manganese data along the $0°$ azimuth for a manganese termi-
nated bulk. Data is offset vertically for clarity.*

Figure B.2: *Simulated antimony data along the $0°$ azimuth for a manganese terminated bulk. Data is offset vertically for clarity.*
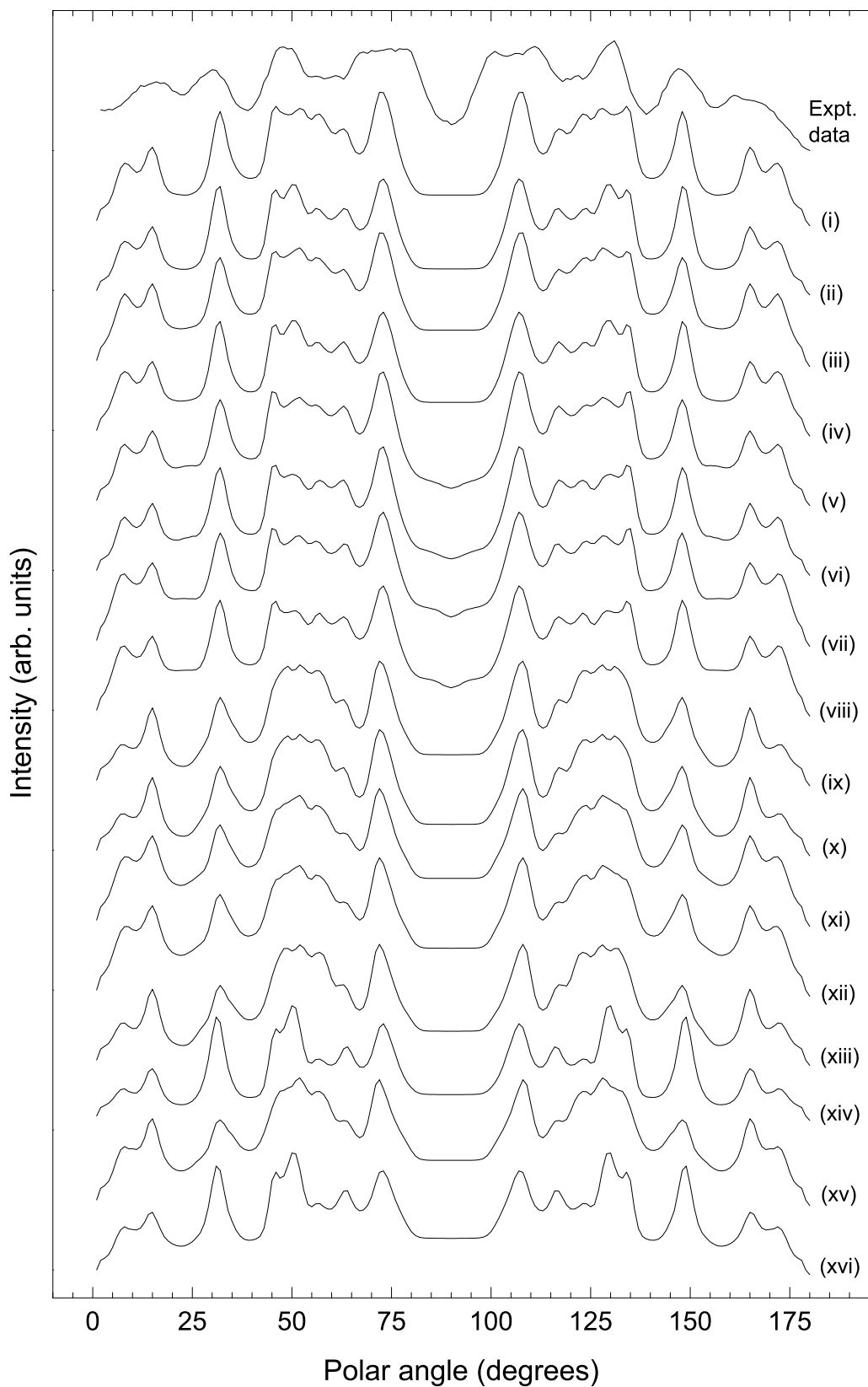
Figure B.3: *Simulated manganese data along the $30°$ yields for a manganese terminated bulk. Data is offset vertically for clarity.*

Figure B.4: *Simulated antimony data along the $30°$ azimuth for a manganese terminated bulk. Data is offset vertically for clarity.*

Figure B.5: *Simulated manganese data along the* $0°$ *yields for an antimony terminated bulk. Data is offset vertically for clarity.*
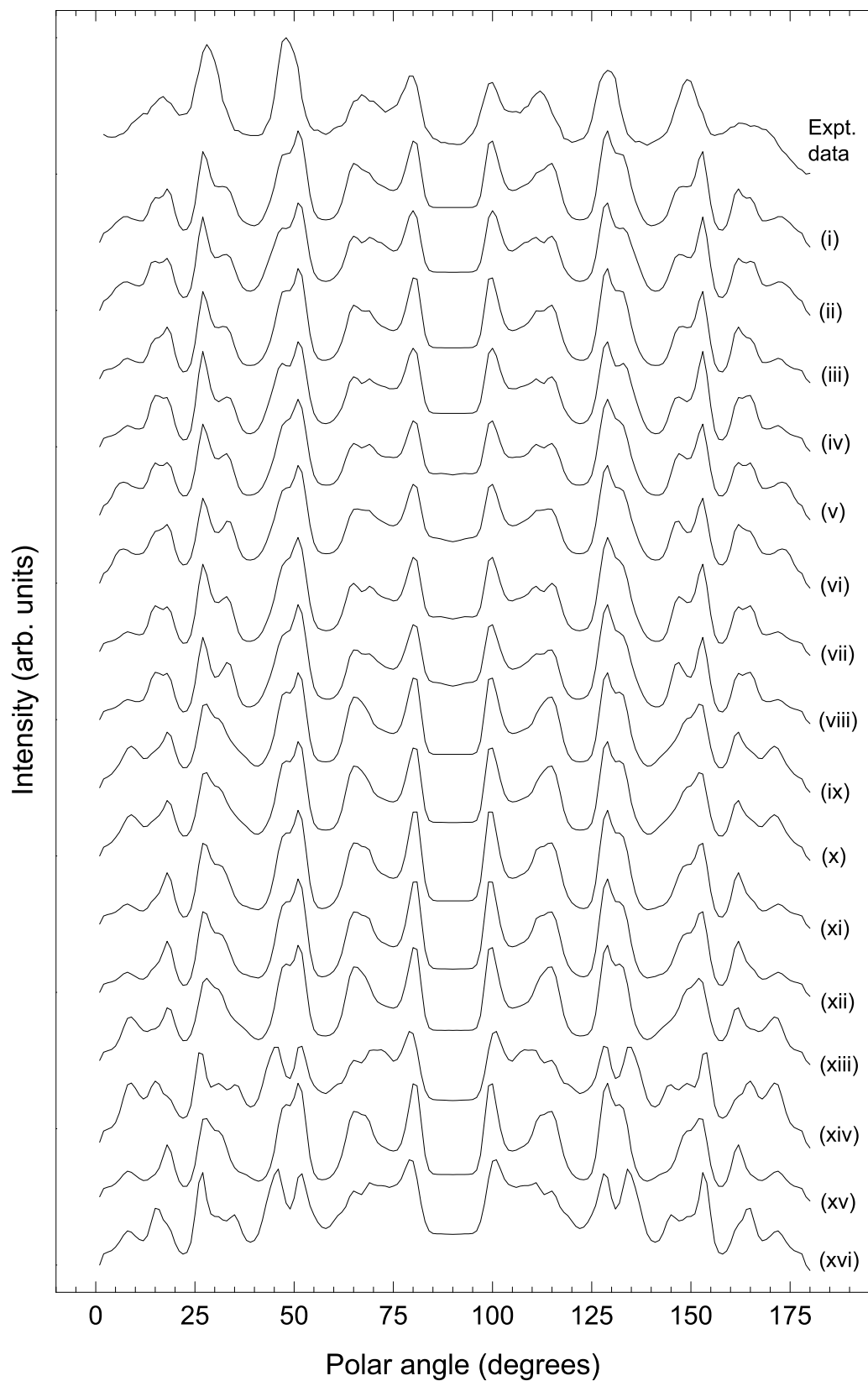
Figure B.6: *Simulated antimony data along the $0°$ azimuth for an antimony terminated bulk. Data is offset vertically for clarity.*
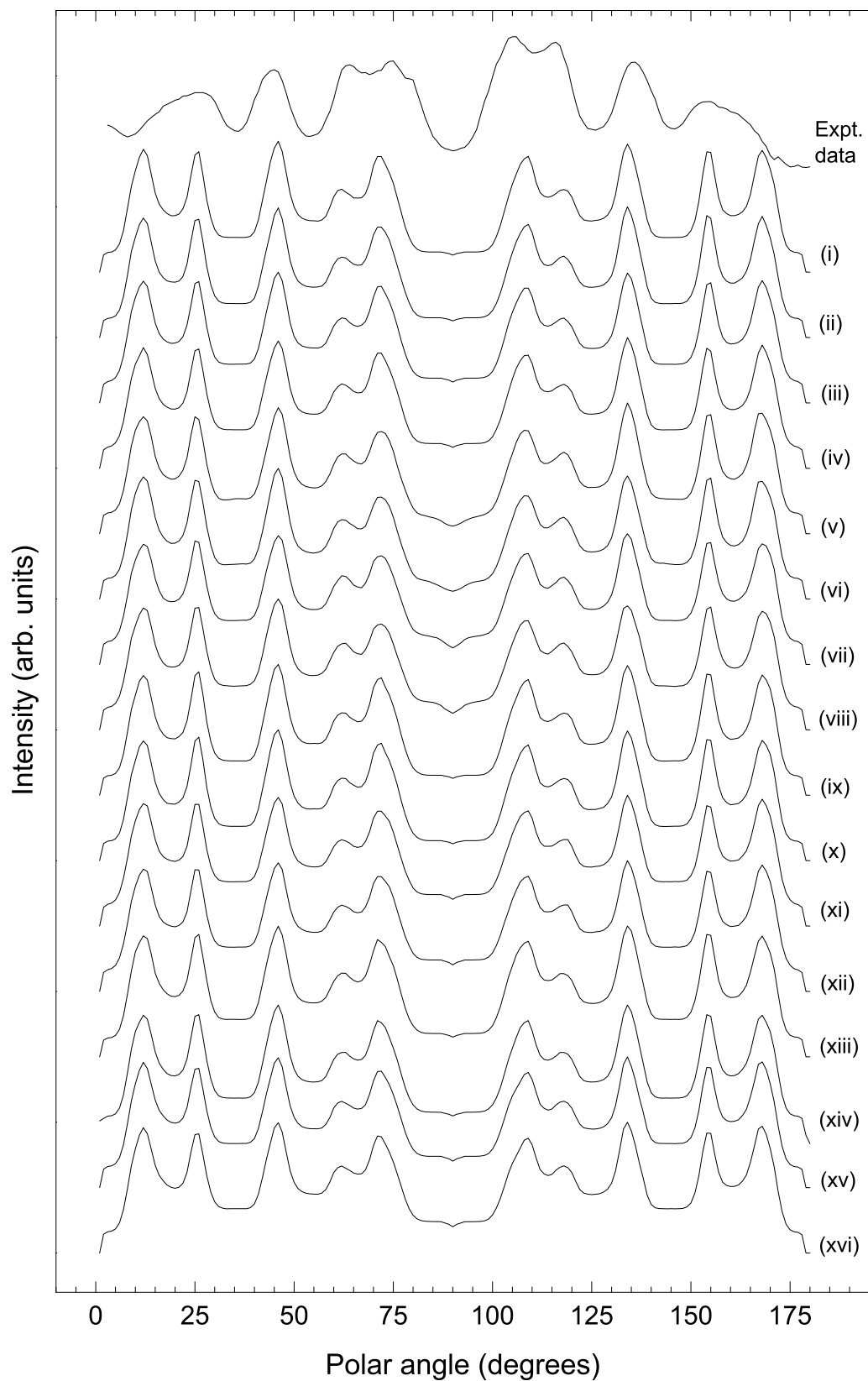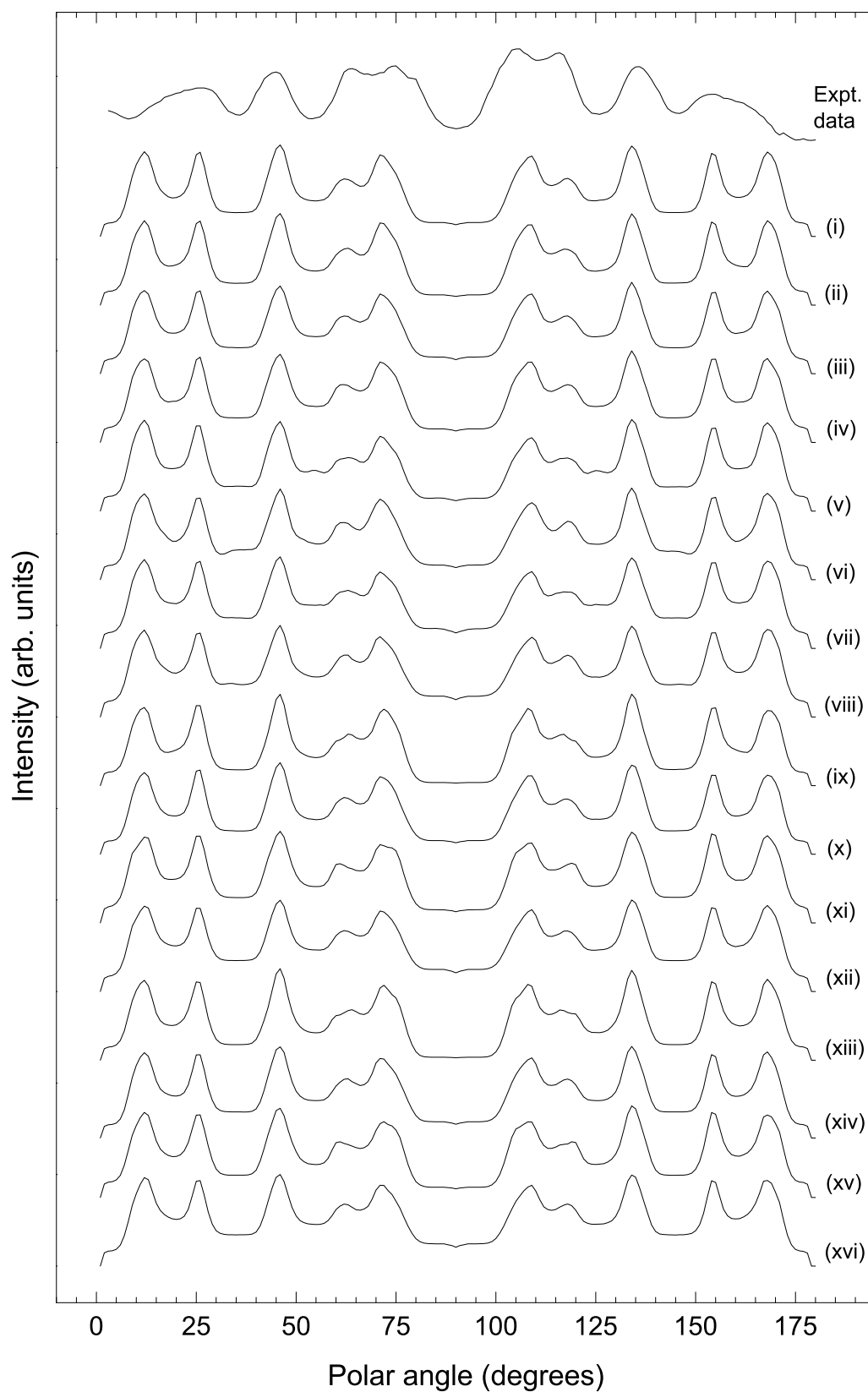
Figure B.7: *Simulated manganese data along the* $30°$ *yields for an antimony terminated bulk. Data is offset vertically for clarity.*
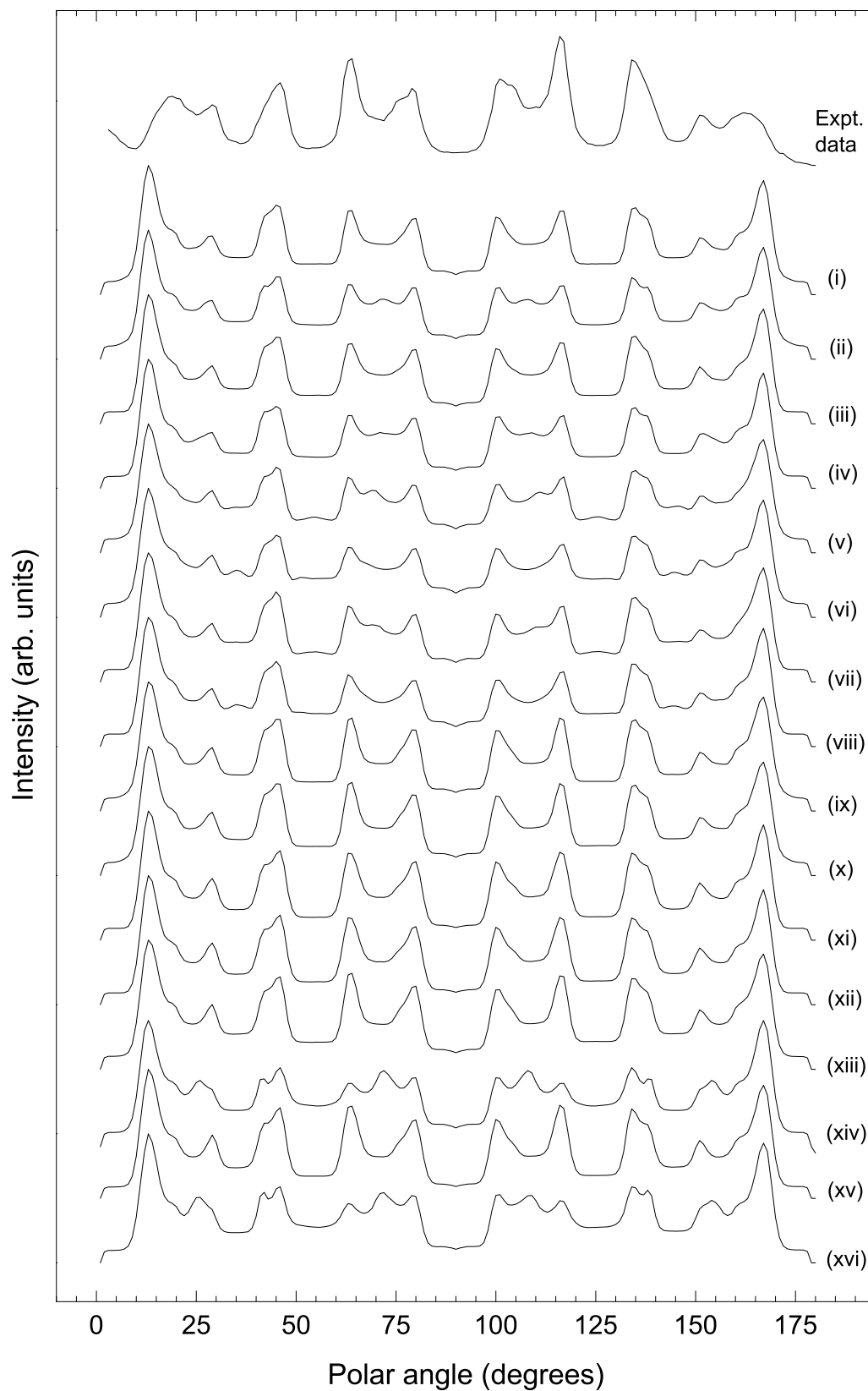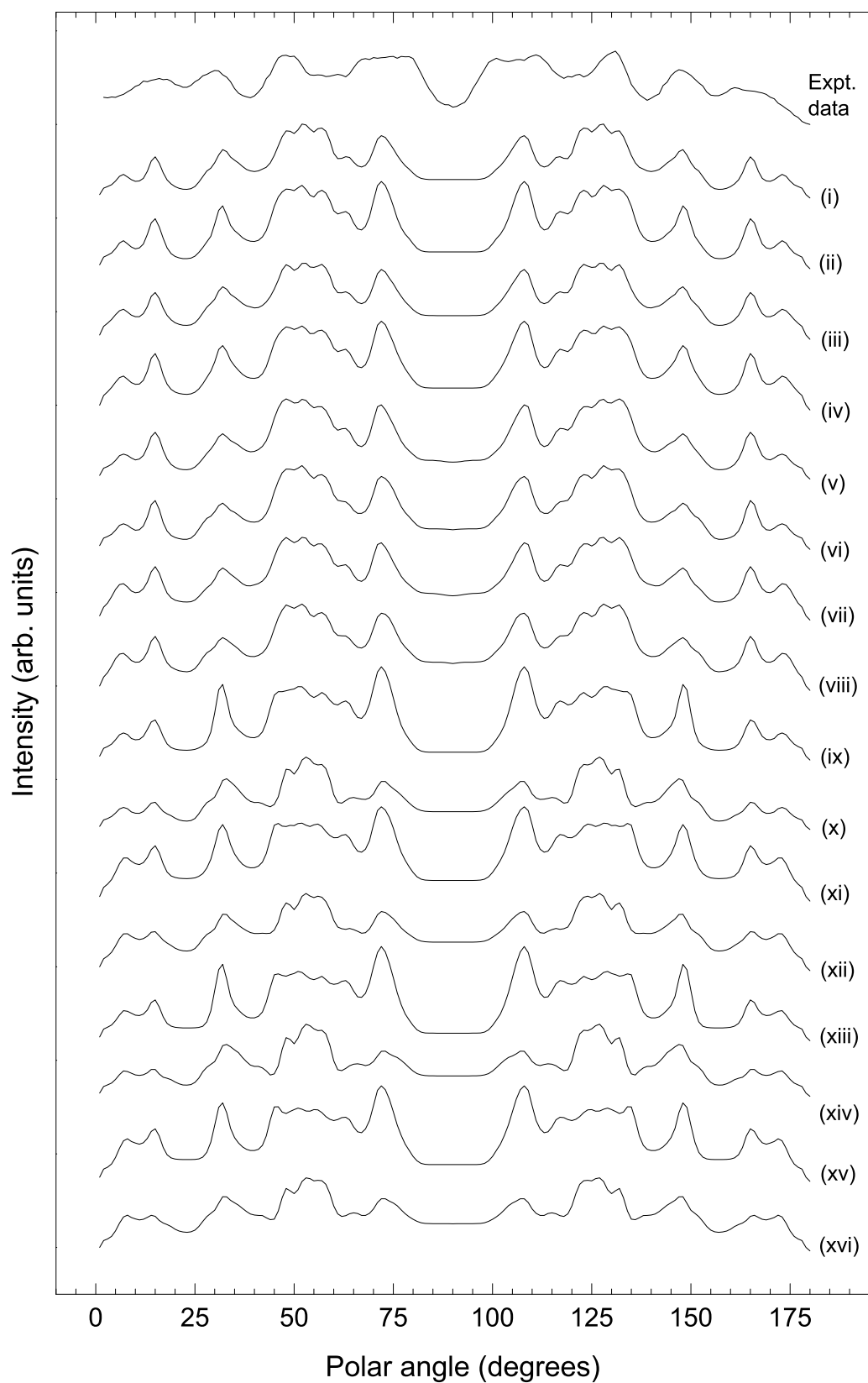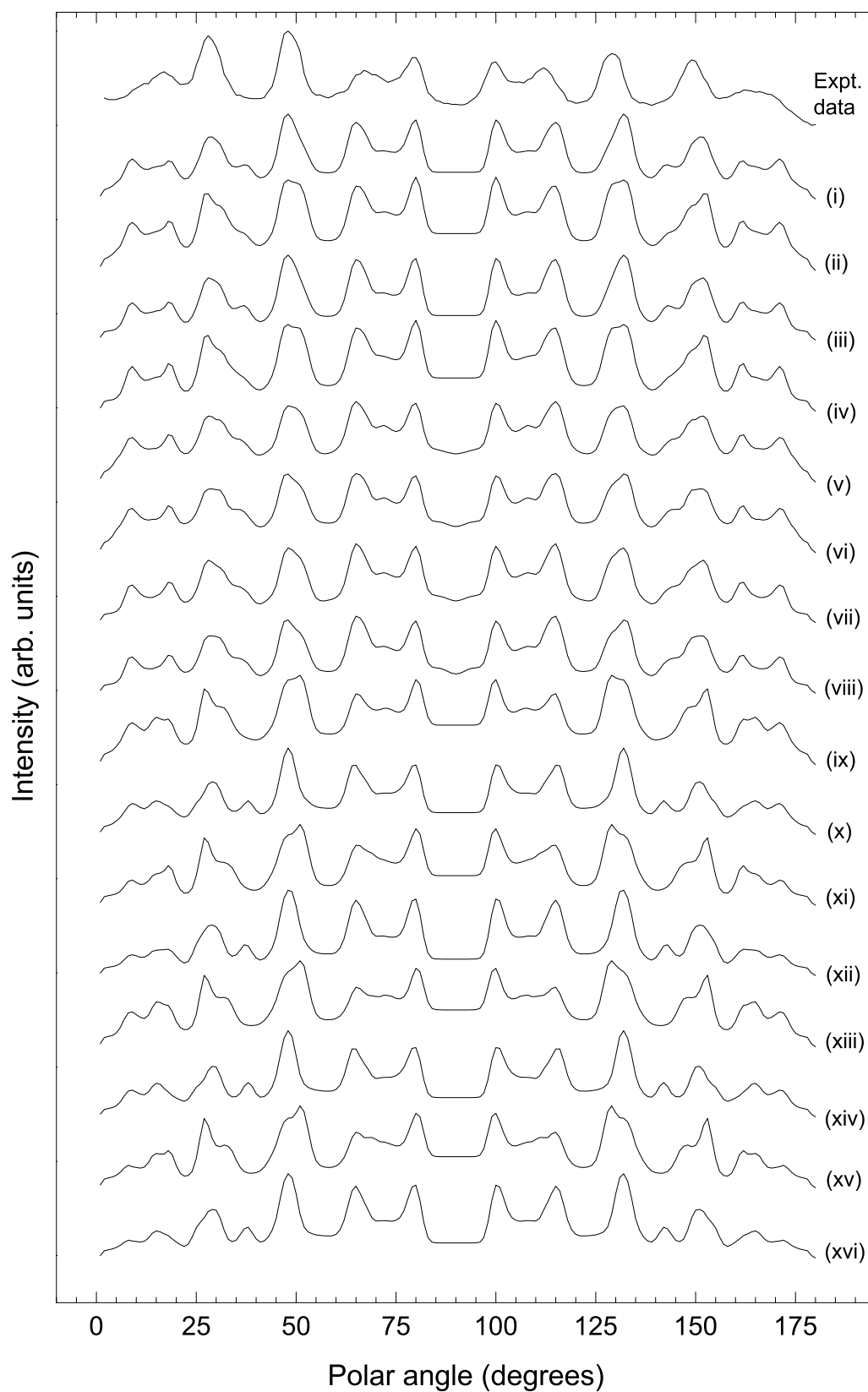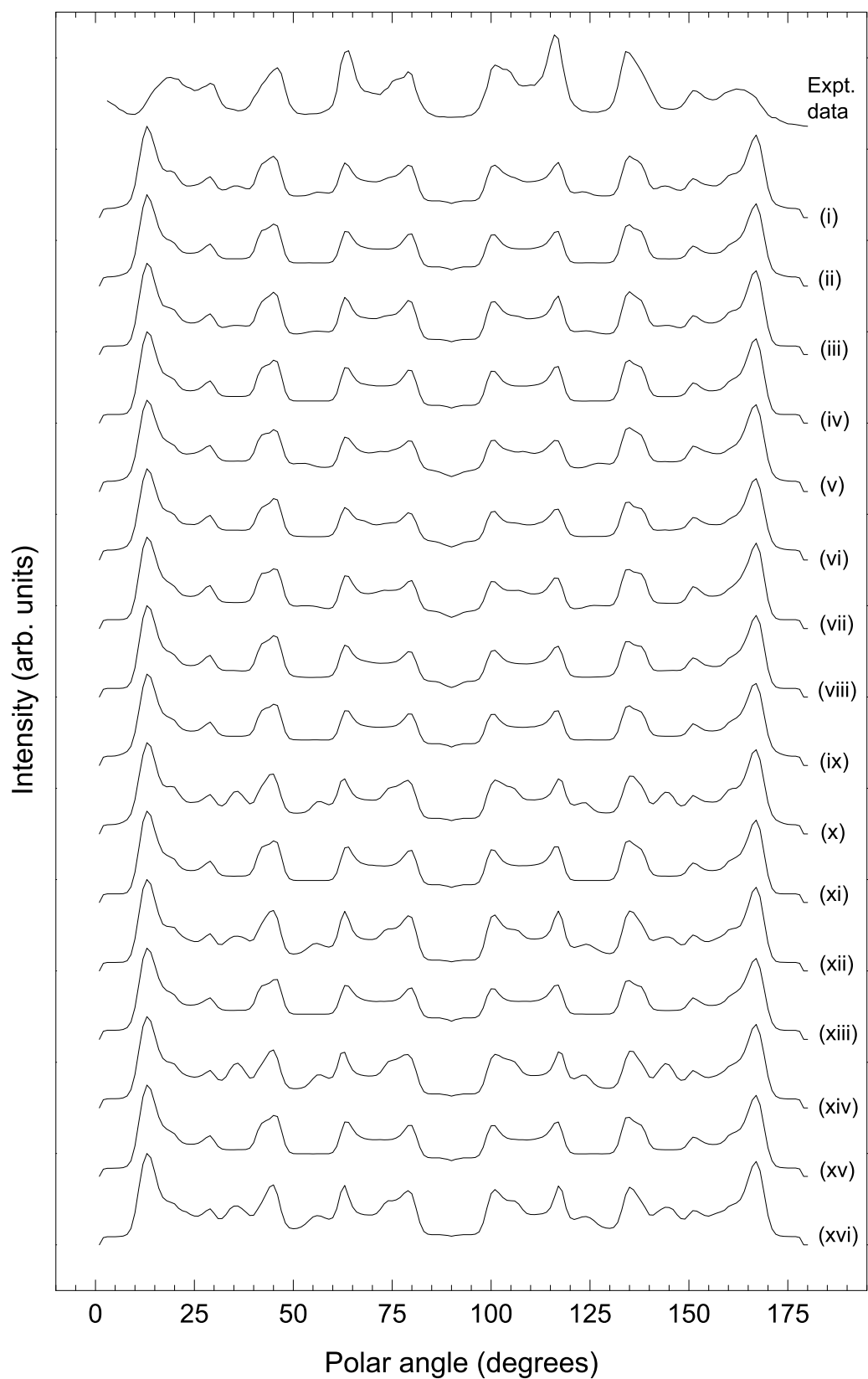
Figure B.8: *Simulated antimony data along the* $30°$ *azimuth for an antimony termi-nated bulk. Data is offset vertically for clarity.*

Appendix C

CLEED input files

For completeness, example CLEED input files used in the calculations are given here. The *.bul* and *.ctr* files are common to all of the calculations. The *.inp* file contains all of the model-specific atomic positions. For the sake of brevity, only one *.inp* file is reproduced here, that being the Mn-adatom in a hcp-site on a Mn-terminated bulk.

C.1 MnSb2x2.bul

```
c: MnSb(0001) bulk -- Mn terminated
#
a1:       3.57495  2.0640    0.0000
a2:      -3.57495  2.0640    0.0000
a3:       0.00000  0.0000   -5.7890
#
m1:  2.  0.
m2:  0.  2.
#
vr:    -7.00
vi:     4.00
#
# bulk:
pb: Mn_MnSb   0.0000     0.0000     0.00000   dr1 0.09397
pb: Sb_MnSb  -1.1917     2.0640    -1.44725   dr1 0.06312
pb: Mn_MnSb   0.0000     0.0000    -2.89450   dr1 0.09397
pb: Sb_MnSb   1.1917     2.0640    -4.34175   dr1 0.06312
#
ei: 30.0
ef: 210.1
es: 4.
it: 0.0
ip: 0.0
ep: 1.e-2
```

```
lm: 7
```

C.2 MnSb2x2.ctr

```
#  MnSb 2x2
#  (control file for R factor program CRFAC)
#  ef=<experimental input file>
#  ti=<corresponding indices in theoretical input file>
#  id=<group ID>
#  : = separator
ef=Spot_2.dat:ti=(0.00,1.00)+(-1.00,0.00)+(1.00,-1.00)+(0.00,-1.00)
+(1.00,0.00)+(-1.00,1.00):id=01:wt=1.
ef=Spot_5.dat:ti=(1.00,1.00)+(2.00,-1.00)+(1.00,-2.00)+(-1.00,-1.00)
+(-2.00,1.00)+(-1.00,2.00):id=02:wt=1.
#
ef=Spot_1.dat:ti=(0.00,0.50)+(-0.50,0.00)+(0.50,-0.50)+(0.00,-0.50)
+(0.50,0.00)+(-0.50,0.50):id=03:wt=1.
ef=Spot_3.dat:ti=(0.50,0.50)+(-0.50,-0.50)+(1.00,-0.50)+(-1.00,0.50)
+(-0.50,1.00)+(0.50,-1.00):id=04:wt=1.
ef=Spot_4.dat:ti=(0.00,1.50)+(-1.50,0.00)+(1.50,-1.50)+(0.00,-1.50)
+(1.50,0.00)+(-1.50,1.50):id=05:wt=1.
.
```

C.3 MnSb2x2.inp

```
c: MnSb(0001) bulk -- Mn-BAB
#
#
a1:      3.57495  2.0640   0.0000
a2:     -3.57495  2.0640   0.0000
a3:      0.00000  0.0000  -5.7890
#
m1: 2.  0.
m2: 0.  2.
#
vr:    -7.00
vi:     4.00
#
# Overlayer
```

```
#
spn: 5
#
# LAYER B
po: Mn_MnSb -1.19165    2.064   7.23623  dr1 0.14095
spp: - x  0.000  0.000  0.000  0.000  0.000
spp: - y  0.000  0.000  0.000  0.000  0.000
spp: - z  1.000  0.000  0.000  0.000  0.000
# LAYER A
po: Mn_MnSb  0.00000    0.0000  5.7890   dr1 0.14095
spp: - x  0.000  0.000  0.000  0.000  0.000
spp: - y  0.000  0.000  0.000  0.000  0.000
spp: - z  0.000  1.000  0.000  0.000  0.000
po: Mn_MnSb  3.57495    2.0640  5.7890   dr1 0.14095
spp: - x  0.000  0.000  0.000  0.000  0.000
spp: - y  0.000  0.000  0.000  0.000  0.000
spp: - z  0.000  1.000  0.000  0.000  0.000
po: Mn_MnSb -3.57495    2.0640  5.7890   dr1 0.14095
spp: - x  0.000  0.000  0.000  0.000  0.000
spp: - y  0.000  0.000  0.000  0.000  0.000
spp: - z  0.000  1.000  0.000  0.000  0.000
po: Mn_MnSb  0.00000    4.1280  5.7890   dr1 0.14095
spp: - x  0.000  0.000  0.000  0.000  0.000
spp: - y  0.000  0.000  0.000  0.000  0.000
spp: - z  0.000  1.000  0.000  0.000  0.000
# LAYER B
po: Sb_MnSb -1.19165    2.064   4.34175  dr1 0.0947
spp: - x  0.000  0.000  0.000  0.000  0.000
spp: - y  0.000  0.000  0.000  0.000  0.000
spp: - z  0.000  0.000  1.000  0.000  0.000
po: Sb_MnSb -4.76665    4.128   4.34175  dr1 0.0947
spp: - x  0.000  0.000  0.000  0.000  0.000
spp: - y  0.000  0.000  0.000  0.000  0.000
spp: - z  0.000  0.000  1.000  0.000  0.000
po: Sb_MnSb  2.38325    4.128   4.34175  dr1 0.0947
spp: - x  0.000  0.000  0.000  0.000  0.000
spp: - y  0.000  0.000  0.000  0.000  0.000
spp: - z  0.000  0.000  1.000  0.000  0.000
po: Sb_MnSb -1.19165    6.192   4.34175  dr1 0.0947
spp: - x  0.000  0.000  0.000  0.000  0.000
spp: - y  0.000  0.000  0.000  0.000  0.000
spp: - z  0.000  0.000  1.000  0.000  0.000
# LAYER A
po: Mn_MnSb  0.00000    0.0000  2.8945   dr1 0.14095
spp: - x  0.000  0.000  0.000  0.000  0.000
spp: - y  0.000  0.000  0.000  0.000  0.000
```

```
spp: - z  0.000  0.000  0.000  1.000  0.000
po: Mn_MnSb  3.57495    2.0640  2.8945    dr1 0.14095
spp: - x  0.000  0.000  0.000  0.000  0.000
spp: - y  0.000  0.000  0.000  0.000  0.000
spp: - z  0.000  0.000  0.000  1.000  0.000
po: Mn_MnSb -3.57495    2.0640  2.8945    dr1 0.14095
spp: - x  0.000  0.000  0.000  0.000  0.000
spp: - y  0.000  0.000  0.000  0.000  0.000
spp: - z  0.000  0.000  0.000  1.000  0.000
po: Mn_MnSb  0.00000    4.1280  2.8945    dr1 0.14095
spp: - x  0.000  0.000  0.000  0.000  0.000
spp: - y  0.000  0.000  0.000  0.000  0.000
spp: - z  0.000  0.000  0.000  1.000  0.000
# LAYER C
po: Sb_MnSb  1.19165    2.064   1.44725   dr1 0.0947
spp: - x  0.000  0.000  0.000  0.000  0.000
spp: - y  0.000  0.000  0.000  0.000  0.000
spp: - z  0.000  0.000  0.000  0.000  1.000
po: Sb_MnSb  4.76665    4.128   1.44725   dr1 0.0947
spp: - x  0.000  0.000  0.000  0.000  0.000
spp: - y  0.000  0.000  0.000  0.000  0.000
spp: - z  0.000  0.000  0.000  0.000  1.000
po: Sb_MnSb -2.38325    4.128   1.44725   dr1 0.0947
spp: - x  0.000  0.000  0.000  0.000  0.000
spp: - y  0.000  0.000  0.000  0.000  0.000
spp: - z  0.000  0.000  0.000  0.000  1.000
po: Sb_MnSb  1.19165    6.192   1.44725   dr1 0.0947
spp: - x  0.000  0.000  0.000  0.000  0.000
spp: - y  0.000  0.000  0.000  0.000  0.000
spp: - z  0.000  0.000  0.000  0.000  1.000
#
rm: Sb_MnSb  1.00
rm: Mn_MnSb  1.00
#
#
zr: 1.3  12.0
```

Appendix D

LEED I-V simulation data

All of the structural models which were discussed in Chap. 6 have been simulated using the CLEED package. In the interests of brevity, the Pendry r-factors (R_P) for all of these structural models are given here, in Tab. D.1 for the structure models shown in Fig. 6.1 and the VB model. The error on these values, as calculated by the *crfac* program is approximately 10%.

Table D.1: *The Pendry r-factors for the models shown in Fig. 6.1 and the vacancy-buckling (VB) model described in Section 6.1.*

	Structure model	Bulk termination	
		Mn	Sb
(a)	Mn, fcc	0.65	0.67
	Mn, hcp	0.69	0.70
	Sb, fcc	0.73	0.66
	Sb, hcp	0.60	0.66
(b)	Mn, fcc	0.59	0.67
	Mn, hcp	0.67	0.66
	Sb, fcc	0.66	0.76
	Sb, hcp	0.70	0.75
(c)	Mn, fcc	0.73	0.67
	Mn, hcp	0.76	0.67
	Sb, fcc	0.80	0.73
	Sb, hcp	0.71	0.72
(d)	3:1 Mn:Sb, fcc	0.81	0.58
	3:1 Mn:Sb, hcp	0.77	0.72
	1:3 Mn:Sb, fcc	0.71	0.63
	1:3 Mn:Sb, hcp	0.70	0.72
(e)	2:1 Mn:Sb, fcc	0.66	0.71
	2:1 Mn:Sb, hcp	0.64	0.65
	1:2 Mn:Sb, fcc	0.67	0.76
	1:2 Mn:Sb, hcp	0.63	0.76
(f)	2:1 Mn:Sb, fcc	0.81	0.59
	2:1 Mn:Sb, hcp	0.65	0.62
	1:2 Mn:Sb, fcc	0.78	0.62
	1:2 Mn:Sb, hcp	0.63	0.57
(g)	fcc	0.72	0.59
	hcp	0.78	0.70
VB	Mn, fcc	0.73	0.65
	Mn, hcp	0.78	0.72
	Sb, fcc	0.77	0.65
	Sb, hcp	0.74	0.69

Bibliography

[1] M. N. Baibich, J. M. Broto, A. Fert, F. N. V. Dau, and F. Petroff, Phys. Rev. Lett. **61**, 2472 (1988).

[2] J. Barnaś, A. Fuss, R. E. Camley, P. Grünberg, and W. Zinn, Phys. Rev. B **42**, 8810 (1990).

[3] S. Datta and B. Das, Appl. Phys. Lett. **56**, 665 (1990).

[4] I. Tudosa, J. A. Katine, S. Mangin, and E. E. Fullerton, Appl. Phys. Lett. **96**, 212504 (2010).

[5] J.-U. Bae, T.-Y. Lin, Y. Yoon, S. J. Kim, A. Imre, W. Porod, J. L. Reno, and J. P. Bird, Appl. Phys. Lett. **92**, 253101 (2008).

[6] P. N. Hai, S. Ohya, M. Tanaka, S. E. Barnes, and S. Maekawa, Nature Lett. **458**, 489 (2009).

[7] B. N. Engel et al., IEEE Trans. Mag. **41**, 132 (2005).

[8] D. Hägele, M. Oestreich, W. W. Rühle, N. Nestle, and K. Eberl, Appl. Phys. Lett. **73**, 1580 (1998).

[9] S. A. Wolf, D. D. Awschalom, R. A. Buhrman, J. M. Daughton, S. von Molnár, M. L. Roukes, A. Y. Chtchelkanova, and D. M. Treger, Science **294**, 1488 (2001).

[10] W. van Roy, O. van Dorpe, V. Motsnyi, Z. Liu, G. Borghas, and J. de Boeck, Phys. Stat. Sol. B **241**, 1470 (2004).

[11] B. D. Schultz, N. Marom, D. Naveh, X. Lou, C. Adelmann, J. Strand, P. A. Crowell, L. Kronik, and C. J. Palmstrøm, Phys. Rev. B **80**, 201309 (2009).

[12] M. Nogami, M. Sekinobu, and H. Doi, J. Japn. Appl. Phys. **3**, 572 (1964).

[13] R. Coehoorn, C. Haas, and R. A. de Groot, Phys. Rev. B **31**, 1980 (1985).

[14] G. C. Han, C. K. Ong, and T. Y. F. Liew, J. Mag. Mag. Mat. **19**, 233 (1999).

[15] H. Akinaga, S. Miyanishi, and Y. Suzuki, Jpn. J. Appl. Phys. **35**, L897 (1996).

[16] T. Amemiya, Y. Ogawa, H. Shimizu, H. Munekata, and Y. Nakanoy, Appl. Phys. Express **1**, 022002 (2008).

[17] H. Kobayashi, M. Kageshima, N. Kimura, H. Aoki, M. Oohigashi, K. Motizuki, and T. Kamimura, J. Mag. Mag. Mat **272-276**, e247 (2004).

[18] W. J. Takei, D. E. Cox, and G. Shirane, Phys. Rev. **129**, 2008 (1963).

[19] J. E. Pask, L. H. Yang, C. Y. Fong, W. E. Pickett, and S. Dag, Phys. Rev. B **67**, 224420 (2003).

[20] W.-H. Xie, B.-G. Liu, and D. G. Pettifor, Phys. Rev. B **68**, 134407 (2003).

[21] L. Kahal, A. Zaoui, and M. Ferhat, J. Appl. Phys. **101**, 093912 (2007).

[22] R. A. de Groot, F. M. Mueller, P. G. van Engen, and K. H. J. Bushcow, Phys. Rev. Lett. **50**, 2024 (1983).

[23] A. M. Sánchez, R. Beanland, J. D. Aldous, C. W. Burrows, I. Maskery, M. Dias, J. Staunton, T. Hase, M. Brewer, and G. R. Bell, Polymorphism in MnSb epitaxial films, (to be submitted to Phys. Rev. B).

[24] S. Li, J.-G. Duh, F. Bao, K.-X. Liu, C.-L. Kuo, X. Wu, L. Lü, Z. Huang, and Y. Du, J. Phys. D: Appl. Phys. **41**, 175004 (2008).

[25] S. Li, Z. Tian, J. Fang, J.-G. D. K.-X. Liu, Z. Huang, Y. Huang, and Y. Du, Sol. State Comm. **149**, 196 (2009).

[26] K. Momma and F. Izumi, J. of Appl. Crystallography **41**, 653 (2008).

[27] W. A. Harrison, J. Vac. Sci. Technol. **16**, 1492 (1969).

[28] D. J. Chadi, J. Vac. Sci. Technol. A **5**, 834 (1987).

[29] M. D. Pashley, Phys. Rev. B **40**, 10481 (1989).

[30] G. P. Srivastava, Rep. Prog. Phys. **60**, 561 (1997).

[31] W. D. Mieher and W. Ho, Surface Science **322**, 151 (1995).

[32] C. R. Parkinson, M. Walker, and C. F. McConville, Surface Science **545**, 19 (2003).

[33] M. L. Anderson, M. S. Ford, P. J. Derrick, T. Drewello, D. P. Woodruff, and S. R. Mackenzie, The Journal of Physical Chemistry A **110**, 10992 (2006).

[34] M. K. Bradley, D. Duncan, J. Robinson, and D. P. Woodruff, Phys. Chem. Chem. Phys. **13**, 7975 (2011).

[35] R. L. Park and H. H. Madden, Surf. Sci. **11**, 188 (1968).

[36] E. A. Wood, J. Appl. Phys. **35**, 1306 (1964).

[37] J. Arthur, J. Appl. Phys. **39**, 4032 (1968).

[38] A. Y. Cho, J. Appl. Phys. **41**, 2780 (1970).

[39] M. A. Herman and H. Sitter, *Molecular Beam Epitaxy - Fundamentals and Current Status*, Springer-Verlag, Berlin, Heidelberg, Germany, 1989.

[40] D. R. Lide, editor, *The Handbook of Chemistry and Physics*, CRC Press, London, 84th edition, 2003-2004.

[41] B. Elman, E. S. Koteles, P. Melman, C. Jagannath, J. Lee, and D. Dugger, Appl. Phys. Lett. **55**, 1659 (1989).

[42] B. Eaglesham and M. Cerullo, Phys. Rev. Lett. **64**, 1943 (1990).

[43] R. S. Wagner and W. C. Ellis, Appl. Phys. Lett. **4**, 89 (1964).

[44] T. I. Kamins, R. S. Williams, D. P. Basile, T. Hesjedal, and J. S. Harris, J. Appl. Phys. **89**, 1008 (2001).

[45] B. Mandl, J. Stangl, T. Martensson, A. Mikkelsen, J. Eriksson, L. S. Karlsson, G. Bauer, L. Samuelson, and W. Seifert, Nano Lett. **6**, 1817 (2006).

[46] S. A. Hatfield and G. R. Bell, J. Cryst. Growth **296**, 165 (2006).

[47] W. Braun, A. Trampert, V. M. Kaganer, B. Jenichen, D. K. Satapathy, and K. H. Ploog, J. Cryst. Growth **301**, 50 (2007).

[48] N. W. Ashcroft and N. D. Mermin, *Solid State Physics*, Brooks/Cole, Belmont, CA USA, 1976.

[49] C. Davisson and L. H. Germer, Phys. Rev. **30**, 705 (1927).

[50] C. Duke and C.W. Tucker Jr., Surf. Sci. **19**, 231 (1969).

[51] C. Duke, J. Anderson, and C.W. Tucker Jr., Surf. Sci. **19**, 117 (1970).

[52] J. B. Pendry, J. Phys. C: Solid St. Phys. **4**, 2501 (1971).

[53] J. B. Pendry, J. Phys. C: Solid St. Phys. **4**, 2514 (1971).

[54] J. C. Slater, Phys. Rev. **51**, 846 (1937).

[55] D. P. Woodruff and T. A. Delchar, *Modern Techniques of Surface Science*, Cambridge University Press, Cambridge UK, second edition, 1994.

[56] M. A. van Hove, W. H. Weinberg, and C.-M. Chan, *Low Energy Electron Diffraction: Experiment, Theory and Surface Structure Determination*, Springer-Verlag, Berlin, 1986.

[57] M. A. van Hove and S. Y. Tong, *Surface Crystallography by LEED*, Springer-Verlag, Berlin, 1979.

[58] M. A. van Hove and A. Barbieri, *Barbieri/van Hove phase shift package*, private communication.

[59] L. F. Mattheiss, Phys. Rev. **133**, A1399 (1964).

[60] http://www.ap.cityu.edu.hk/personal-website/Van-Hove_files/leed/leedpack.html, Personal website of M. A. van Hove: accessed May 2009.

[61] G. Held and W. Braun, *Cambridge LEED Package*, private communication.

[62] J. B. Pendry, J. Phys. C: Solid St. Phys. **13**, 1937 (1980).

[63] D. A. Shirely, Phys. Rev. B **5**, 4709 (1972).

[64] B. D. Cullity and S. R. Stock, *Elements of X-ray Diffraction*, Prentice-Hall, New Jersey, third edition, 2001.

[65] B. E. Warren, *X-ray Diffraction*, Dover Publications, New York, 1990.

[66] D. K. Bowen and B. K. Tanner, *X-ray Metrology in Semiconductor Manufacturing*, CRC Press, Boca Raton, London, New York, 2006.

[67] G. Schütz, W. Wagner, W. Wilhelm, P. Kienle, R. Zeller, R. Frahm, and G. Materlik, Phys. Rev. Lett. **58**, 737 (1987).

[68] S. W. Lovesey and S. P. Collins, *X-ray Scattering and Absorption by Magnetic Materials*, Oxford Series on Synchrotron Radiation, Oxford University Press, Oxford, 1996.

[69] J. Stöhr and H. C. Siegmann, *Magnetism: From Fundamentals to Nanoscale Dynamics*, Springer series in Solid-State Sciences, Springer-Verlag, Berlin, Heidelberg, New York, 2006.

[70] G. van der Laan and B. T. Thole, Phys. Rev. B **43**, 13401 (1991).

[71] C. T. Chen, Y. U. Idzerda, H.-J. Lin, N. V. Smith, G. Meigs, E. Chaban, G. H. Ho, E. Pellegrin, and F. Sette, Phys. Rev. Lett. **75**, 152 (1995).

[72] C. Kapusta, P. Fischer, and G. Schutz, J. of Alloys Compd. **286**, 37 (1999).

[73] B. T. Thole, P. Carra, F. Sette, and G. van der Laan, Phys. Rev. Lett. **68**, 1943 (1992).

[74] P. Carra, B. T. Thole, M. Altarelli, and X. Wang, Phys. Rev. Lett. **70**, 694 (1993).

[75] C. Piamonteze, P. Miedema, and F. M. F. de Groot, Phys. Rev. B **80**, 184410 (2009).

[76] W. L. OBrien, B. P. Tonner, G. R. Harp, and S. S. P. Parkin, J. Appl. Phys **76**, 6462 (1994).

[77] B. L. Henke, E. M. Gullikson, and J. C. Davis, At. Data Nucl. Data Tab. **54**, 191 (1993).

[78] M. Abes et al., Phys. Rev. B **82**, 184412 (2010).

[79] D. A. Ogarev, S. A. Aitkhozhin, Y. S. Temirov, K. K. Palkina, K. A. Shchamkhalov, and S. F. Marenkin, Inorganic Mat. **41**, 1162 (2005).

[80] K. Motizukic, T. Kawakami, M. Oohigashi, H. Harima, T. Mozue, H. Kobayashi, and T. Kamimura, Physica. B **284-288**, 1345 (2000).

[81] S. Li, J.-G. Duh, F. Bao, K.-X. Liu, C.-L. Kuo, X. Wu, L. Lü, Z. Huang, and Y. Du, J. Phys. D **41**, 175004 (2008).

[82] S. A. Hatfield and G. R. Bell, Surf. Sci. **61**, 5368 (2007).

[83] R. Nakane, J. Kondo, M. W. Yuan, S. Sugahara, and M. Tanaka, J. Cryst. Growth **278**, 649 (2005).

[84] V. Garcia, M. Bibes, B. Vodungbo, M. Eddrief, D. Demaille, and M. Marangolo, Appl. Phys. Lett **92**, 011905 (2008).

[85] A. Ouerghi et al., Phys. Rev. B **74**, 155412 (2006).

[86] *http://www.fhi-berlin.mpg.de/KHsoftware/LEEDpat/index.html*, accessed January 2011.

[87] Q.-K. Xue, Q. Z. Xue, R. Z. Bakhtizin, Y. Hasegawa, I. S. T. Tsong, T. Sakurai, and T. Ohno, Phys. Rev. Lett. **82**, 3074 (1999).

[88] K. Aït-Mansour, L. Kubler, M. Diani, D. Dentel, J.-L. Bischoff, L. Simon, J. Peruchetti, and A. Galliano, Phys. Rev. B **67**, 195407 (2003).

[89] J. Yuhara, M. Schmid, and P. Varga, Phys. Rev. B **67**, 195407 (2003).

[90] S. Hatfield, J. Aldous, and G. Bell, Appl. Surf. Sci. **255**, 3567 (2009).

[91] K. Ono, M. Shuzo, M. Oshima, and H. Akinaga, Phys. Rev. B **64**, 085328 (2001).

[92] J. S. Blakemore, J. Appl. Phys. **53**, R123 (1982).

[93] T. Chen, J. C. Mikkelsen, and G. B. Charlan, J. Cryst. Growth **43**, 5 (1978).

[94] S. A. Hatfield, *Heteroepitaxial growth of MnSb on III-V semiconductor substrates*, PhD thesis, University of Warwick, 2007.

[95] H. Ido, T. Kaneko, and K. Kamigaki, J. Phys. Soc. Jpn. **22**, 1418 (1967).

[96] S. Liu, S. Bedair, and N. El-Masry, Matt. Lett. **42**, 121 (2000).

[97] J.-C. Zheng and J. W. Davenport, Phys. Rev. B **69**, 144415 (2004).

[98] H. Ohno, Science **281**, 951 (1998).

[99] G. Yang, F. Zhu, and S. Dong, J. Cryst. Growth **316**, 145 (2011).

[100] K. Ganesan and H. L. Bhat, J. Supercond. Nov. Magn. **201**, 391 (2008).

[101] T. Okita and Y. Makino, J. Phys. Soc. Jpn. **25**, 120 (1968).

[102] R. Podloucky, Sol. State. Comm. **50**, 763 (1984).

[103] N. Vast, B. Siberchicot, and P. G. Zerah, J. Phys.: Condens. Matter **4**, 10469 (1992).

[104] H. Tatsuoka, K. Isaji, H. Kuwabara, Y. Nakanishi, T. Nakamura, and H. Fujiyasu, Appl. Surf. Sci. **113**, 48 (1997).

[105] H. Zhang, S. S. Kushvaha, A. T. S. Wee, and X.-S. Wang, J. Appl. Phys. **102**, 023906 (2007).

[106] B. L. Low, C. K. Ong, G. C. Han, H. Gong, T. Y. F. Liew, H. Tatsuoka, H. Kuwabara, and Z. Yang, J. Appl. Phys. **84**, 973.

[107] C. Sánchez-Hanke, C.-C. Kao, and S. Hulbert, Nucl. Instr. and Meth. Phys. Res. Sect. A **608**, 351 (2009).

[108] P. Turban, S. Andrieu, E. Snoeck, B. Kierren, and C. Teodorescu, J. Mag. Mag. Mat. **240**, 427 (2002).

[109] W. L. O'Brien and B. P. Tonner, Phys. Rev. B **51**, 617 (1995).

[110] A. Kimura, T. Kanbe, T. Xie, S. Qiao, M. Taniguchi, T. Muro, S. Imada, and S. Suga, Jpn. J. Appl. Phys. **42**, 4692 (2003).

[111] *http://www.nist.gov/srd/nist71.htm*, Accessed September 2010 (released 2000).

[112] K. W. Edmonds, N. R. S. Farley, T. K. Johal, G. van der Laan, R. P. Campion, B. L. Gallagher, and C. T. Foxon, Phys. Rev. B **71**, 064418 (2005).

[113] G. R. Harp, S. S. P. Parkin, W. L. O'Brien, and B. P. Tonner, Phys. Rev. B **51**, 3293 (1995).

[114] H. Ebert, Fully relativistic band structure calculations for magnetic solids - formalism and application, in *Electronic Structure and Physical Properies of Solids*, edited by H. Dreyss, volume 535 of *Lecture Notes in Physics*, pages 191–246, Springer Berlin / Heidelberg, 2000.

[115] W. L. O'Brien and B. P. Tonner, Phys. Rev. B **50**, 12672 (1994).

[116] N. V. Smith, C. T. Chen, F. Sette, and L. F. Mattheiss, Phys. Rev. B **46**, 1023 (1992).

[117] M. Fraune, U. Rüdiger, , G. Güntherodt, S. Cardoso, and P. Freitas, Appl. Phys. Lett. **77**, 3815 (2000).

[118] J. D. Aldous, C. W. Burrows, T. P. A. Hase, J. A. Duffy, C. Sánchez-Hanke, T. Decoster, W. Theis, A. Quesada, A. K. Schmid, and G. R. Bell., to be submitted to Phys. Rev. B .

[119] M. Kästner, L. Däweritz, and K. Ploog, Surf. Sci. **511**, 323 (2002).

[120] A. Ouerghi, M. Marangolo, M. Eddrief, S. Guyard, V. H. Etgens, and Y. Garrea, Phys. Rev. B **68**, 115309 (2003).

[121] S. Y. Tong, G. Xu, and W. N. Mei, Phys. Rev. Lett. **52**, 1693 (1984).

[122] D. K. Biegelsen, R. D. Bringans, J. E. Northrup, and L.-E. Swartz, Phys. Rev. Lett. **65**, 452 (1990).

[123] P. J. Feibelman, Phys. Rev. B **56**, 2175 (1997).

[124] H. Ibach, Surface Science Reports **29**, 195 (1997).

[125] R. Terborg et al., Surface Science **446**, 301 (2000).

[126] M. J. Harrison, D. P. Woodruff, J. Robinson, D. Sander, W. Pan, and J. Kirschner, Phys. Rev. B **74**, 165402 (2006).

[127] *multLEED version 5.50 (2008)*, http://www.ocivm.com.

[128] A. Kjekshus, T. Rakke, and A. F. Andresen, Acta Chem. Scand. A **28**, 996 (1974).

[129] H. Takizawa, M. Shimada, Y. Sato, and T. Endo, Mater.. Lett. **18**, 11 (1993).

[130] L. Heaton and N. S. Gingrich, Acta Crystalallog. **8**, 207 (1955).

[131] M. E. Straumanis and C. D. Kim, J. Appl. Phys. **36**, 3822 (1965).

[132] M. C. Qian, C. Y. Fong, W. E. Pickett, and H.-Y. Wang, J. APpl. Phys. **95**, 7459 (2004).

[133] T. W. Kim, H. C. J., T. W. Kang, H. S. Lee, J. Y. Lee, and S. Ji, Appl. Phys. Lett. **88**, 021915 (2006).

[134] I. Hotovy, J. Huran, and L. Spiess, J. of Matt.. Sci. **39**, 2609 (2004).

[135] A. Kantor, L. Dubrovinsky, N. Dubrovinskaia, I. Kantor, and I. Goncharenko, J. of Alloys Compd. **402**, 42 (2005).

[136] T. Humphries and D. Pickup, Internal final year undergraduate project reports, 2011.

[137] P. Ehrhart, editor, *Landolt-Börnstein - Group III Condensed Matter*, volume 25: Atomic Defects in Metals, Springer Materials.